

Dynamic slope stability and geomorphological site effects : Numerical simulations and back analysis

Zezhong Zhang

▶ **To cite this version:**

Zezhong Zhang. Dynamic slope stability and geomorphological site effects : Numerical simulations and back analysis. Earth Sciences. Université Paris sciences et lettres, 2018. English. NNT : 2018PSLEM074 . tel-02196802

HAL Id: tel-02196802

https://pastel.hal.science/tel-02196802

Submitted on 29 Jul 2019

HAL is a multi-disciplinary open access archive for the deposit and dissemination of scientific research documents, whether they are published or not. The documents may come from teaching and research institutions in France or abroad, or from public or private research centers.

L'archive ouverte pluridisciplinaire **HAL**, est destinée au dépôt et à la diffusion de documents scientifiques de niveau recherche, publiés ou non, émanant des établissements d'enseignement et de recherche français ou étrangers, des laboratoires publics ou privés.

PSL
UNIVERSITÉ PARIS

THÈSE DE DOCTORAT
DE L'UNIVERSITÉ PSL

Préparée à MINES ParisTech

DYNAMIC SLOPE STABILITY AND GEOMORPHOLOGICAL SITE EFFECTS: NUMERICAL SIMULATIONS AND BACK ANALYSIS

Soutenue par

Zezhong ZHANG

Le 19 Décembre 2018

Ecole doctorale n° 398

Géosciences, Ressources Naturelles et Environnement (GRNE)

Spécialité

Géosciences et géo-ingénierie

Composition du jury :

Jean-François SEMBLAT ENSTA	*Président*
Véronique MERRIEN Conservatoire National des Arts et Métiers	*Rapporteur*
Luca LENTI IFSTTAR	*Rapporteur*
Fréderic L. PELLET MINES ParisTech	*Examinateur*
Jean-Alain FLEURISSON MINES ParisTech	*Directeur de thèse*

MINES ParisTech | PSL

Résumé

Stabilité dynamique des versants et effets de site d'origine géomorphologique : simulations numériques et rétro-analyses

Lors de séismes, les effets de site peuvent augmenter ou parfois diminuer l'intensité du mouvement du sol car la présence d'un relief ou de dépôts superficiels peut modifier localement le champ d'ondes. Il a également été montré que la réponse du mouvement du sol en un site spécifique affecte fortement la fréquence et la durée du mouvement sismique. De nombreuses études ont montré l'influence de la topographie sur l'amplification de l'accélération en utilisant des méthodes numériques incorporant un modèle de pente, mais la plupart des recherches ne se sont concentrées que sur un ou plusieurs facteurs indépendants qui affectent le mouvement du sol. Bien que des études sur l'interaction entre la fréquence des ondes sismiques et les caractéristiques topographiques (ou géologique de subsurface) aient été récemment menées, la connaissance de cet effet de couplage lié à la topographie de la pente fait encore défaut. Par conséquent, une investigation plus approfondie de l'amplification due à la topographie des pentes est toujours nécessaire.

Dans cette thèse, des simulations numériques ont d'abord été effectuées avec le logiciel en différences finies FLAC (Itasca) sur un modèle de pente élastique linéaire homogène pour caractériser l'amplification de l'accélération le long de la surface située le long et à l'arrière de la crête d'une pente, et évaluer ainsi l'effet de la topographie sur l'amplification de l'accélération. L'interaction entre la fréquence du signal sismique appliqué à la base du modèle et l'angle et la hauteur de la pente a été particulièrement étudiée. Il a été constaté que le facteur d'amplification de l'accélération varie de manière significative avec l'angle de et la hauteur de la pente, la fréquence et la durée (nombre de cycle) du signal. De plus, l'amplification du mouvement du sol due à la topographie de la pente est influencée de manière significative par l'effet de couplage complexe entre les ondes incidentes et les ondes réfléchies sur la topographie, et qu'elle est fortement contrôlée par le rapport entre la longueur d'onde du signal incident et la hauteur de la pente.

Les simulations numériques sont basées sur une étude géotechnique et une modélisation géomécanique nécessitant de valider les résultats par des comparaisons entre les résultats de modélisations et les données provenant des observations sur le terrain. L'analyse des domaines de fréquence, telle que la densité spectrale et la réponse en fréquence, est un moyen performant pour comprendre les caractéristiques des processus et les divers phénomènes qui ne peuvent pas être expliqués dans le domaine temporel. À cette fin, une étude de la crête du parc Xishan à Zigong au Sichuan en Chine a été réalisée. Les amplifications du site associées au mouvement du sol produit par le séisme de Wenchuan en 2008 ont été évaluées à l'aide de la technique du rapport spectral standard (SSR) et de la méthode d'accélération quadratique moyenne (arms) dans le domaine temporel. Une analyse numérique à 2D au moyen du logiciel FLAC (Itasca) a été ensuite mise en œuvre et les résultats ont été comparés aux mesures de terrain. Les pics "simulés" des amplifications spectrales sont toujours inférieurs à ceux dérivés des enregistrements de terrain. L'effet d'atténuation important

sur le mouvement d'entrée pour les hautes fréquences met en évidence le fait qu'un rapport d'amortissement du signal ne représente pas correctement la dissipation d'énergie dans les simulations numériques. Des amplifications significatives se sont produites à des fréquences élevées (> 10 Hz) et sont considérées comme résultant de conditions locales spécifiques telles que la fracturation des roches et les irrégularités géométriques locales. Ces amplifications ne sont pas nécessairement localisées au sommet de la colline.

Enfin, des études paramétriques ont été réalisées avec des modèles élastiques en termes de diverses géométries de pente 2D et de couches géologiques de subsurface pour caractériser les amplifications du mouvement du sol. L'analyse paramétrique a pour but de comprendre le rôle joué par ces couches de surface, l'angle de la pente et la hauteur de la pente sur l'amplification du mouvement du sol, et donc d'évaluer si l'amplification du site peut être responsable du déclenchement du glissement de terrain. Ensuite, l'analyse dynamique sur des modèles de pente pour différentes magnitudes a été effectuée et la stabilité de la pente du site de Las Colinas au Salvador a été évaluée sur la base du déplacement induit. Les résultats numériques ont clairement montré que les effets de site peuvent avoir induit d'importantes amplifications du mouvement du sol qui ont contribué à déclencher des glissements de terrain.

Mots clés : Effets de site topographiques, Simulations numériques, Stabilité des pentes, Tremblements de terre, Glissements de terrain

Abstract

Site effects may increase or sometimes decrease ground motion intensity as the local wave field can be modified due to the presence of topographic features or superficial weak materials. Ground motion records at the specific site also showed that the frequency and duration of seismic motion could also be strongly affected. Numerous studies investigated the influence of topography on acceleration amplification using numerical methods incorporating a slope model, but most researches only focused on one or several independent factors that may affect ground motion. Although studies on the interaction between seismic wave frequency and topographic feature (or surface geology) have been recently reported, knowledge of such coupling effects related to slope topography is still lacking. Therefore, a more thorough investigation of amplifications due to slope topography is still needed.

In this research work, numerical simulations using the FLAC software (Itasca)were first conducted with a homogeneous linear elastic slope model in order to characterize the acceleration amplification along the slope surface and behind the slope crest, and then to evaluate the topographic effect on the acceleration amplification. The interaction between the frequency of the seismic input motion applied at the base of the model with the slope angle and height has been deeply investigated. It was found that significant changes in the acceleration amplification factor result from variations in the slope angle and height as well as the signal frequency and duration. In addition, it has been shown that the ground motion amplification due to slope topography result from complex coupling effects between the input waves and the reflected waves on the topographic features and is highly controlled by the ratio between the wavelength of the input signal and the slope height.

Numerical simulations are based on geotechnical investigations and geotechnical modeling, and it is necessary to validate the results through comparisons between modeling results and field observations. Frequency domain analysis such as spectral density and frequency response are an effective way to understand process characteristics and the various phenomena that cannot be explained in the time domain. For this purpose, a case study at Xishan Park ridge in Zigong in China has been studied. Site amplifications associated with the ground motion produced by the 2008 Wenchuan earthquake have been evaluated using the Standard Spectral Ratio (SSR) technique and root-mean-square acceleration (arms) method in time domain. 2D numerical analysis using the finite difference method using the FLAC software (Itasca) has been then performed and results have been compared with monitoring data. The “simulated” peaks of the spectral amplifications are always lower than those derived from the field records. The strong attenuation of input motion at high frequencies highlights the shortcoming that a signal damping ratio does not adequately represent the energy dissipation in numerical simulations. Significant amplifications occurred at high frequencies (>10 Hz) are considered to result from local specific conditions such as rock fracturing and ridge steps; thus they do not necessarily occur at the top of the hill.

Finally, parametric studies were performed with elastic models in terms of various 2D slope geometries and geological layers to characterize the ground motion amplifications. The purpose of the parametric analysis is to understand the role of the geological layer, slope angle and slope height on the ground motion amplification, and thus to estimate if site amplifications could be responsible for the triggering of the landslide. Then, the dynamic analysis on the slope model for different seismic magnitudes was performed and the evaluation of the Las Colinas slope stability in Salvador was evaluated through the analysis of the induced displacement. The numerical results clearly showed that site effects can have induced significant ground motion amplifications that contributed to triggering landslides.

Keywords: Site effects, Numerical simulations, Slope stability, Earthquake, Landslides

Acknowledgements

First of all, I would like to express sincere gratitude to my supervisor, Professor Jean-Alain Fleurisson for providing the opportunity to work with him in MINES ParisTech. I am really grateful to him for his guidance and patient support during the completion of the research works. Without his kind help, I would never be able to complete this study. I also want to thank Professor Frédéric Pellet for his great support in the paper publishing and kind encouragements all these years. My experience working with them was incredibly rewarding and full of a lot of fun.

I gratefully acknowledge the China Scholar Council which provided a Ph.D. scholarship and gave me therefore the chance to study abroad in the Geosciences and Geoengineering Research Department of MINES ParisTech.

I would like to extend my thanks to Dominique Vassiliadis and Véronique Lachasse for their kind assistance and help provided throughout my stay at Fontainebleau. They really helped me a lot in facilitating the administrative procedures of registration and application to the resident card.

My sincere thanks for many reasons also go to my friends and colleagues (Mohamed, Xiangdong, Paule, Thuong, Sara, Hafsa, Aurelien, Hao, Shuaitao and Yubing). We ever did studying, meeting, eating together with a lot of fun. I will surely remember the very nice time spent together with them.

Last, I would like to express my appreciation to my family and Haijing for their unconditional love and continuous support.

Table of contents

Table of contents

Chapter 1 Introduction 1
1.1 Motivation 1
1.2 Literature review 4
1.2.1 Topographic amplification 5
1.2.2 Influence of the subsurface geology 23
1.2.3 Summary 24
1.3 Objectives 24
1.4 Thesis document structure 25
Chapter 2 Effects of slope topography on acceleration amplification and interaction between slope topography and seismic input motion 27
2.1 Introduction 27
2.2 Numerical models 29
2.3 Topographic effects on acceleration 31
2.3.1 Analysis of typical results 31
2.3.2 Effects of the slope angle 35
2.3.3 Effects of the slope height 37
2.3.4 Effects of curvature of the slope edge 39
2.4 Influence of seismic input motion 42
2.4.1 Effects of signal frequency 42
2.4.2 Effects of the number of cycles of seismic input motion 44
2.5 Conclusions 45
Chapter 3: Site effects on seismic ground motions at Xishan Park ridge in Zigong, Sichuan, China 47
3.1 Introduction 47
3.2 Study area 49
3.3 Methodology and Data 50
3.4 Site effects on ground motion 53
3.4.1 Effects of topography 53
3.4.2 Effects of surficial soft deposit 55
3.5 Numerical analysis 57

3.5.1 Results of the analysis in the frequency domain 59
3.5.2 Results of the analysis in the time domain 64
3.6 Conclusions 66
Chapter 4: Site effects contributing to triggering the Las Colinas landslide during the 2001 M_w=7.7 El Salvador earthquake 67
4.1 Introduction 67
4.2 Characterization of the Las Colinas landslide in El Salvador 70
4.3 Methodology 70
4.4 Analysis of the results 74
4.4.1 Effects of slope angle 74
4.4.2 Effects of slope height 76
4.4.3 Effects of surface geology 77
4.4.4 Effects of input motion frequency 78
4.4.5 Effects of the number of cycles of the input motion 79
4.4.6 Effects of ground motion magnitude on slope stability 80
4.5 Conclusions 82
Chapter 5: Conclusions and Recommendations 83
5.1 Conclusions 83
5.2 Recommendations for further research 84
References 87
Publications of the author 95

List of Figures

Figure 1.1: Collapsed buildings during the 2008 Wenchuan earthquake (http://agnesngoy.blogspot.fr) 1

Figure 1.2: Fatality causes for all deadly earthquakes between September 1968 and June 2008. (a) With deaths from the 2004 Sumatra event; (b) without deaths from the 2004 Sumatra event. (Marano et al., 2010) 2

Figure 1.3: Non-shaking fatalities for all deadly earthquakes between September 1968 and June 2008. (a) With dead people from the 2004 Sumatra event; (b) without dead people from the 2004 Sumatra event. (Marano et al., 2010) 3

Figure 1.4: The location of seismological stations near Sourpi and example of observed ground motions. (a) Section of the ridge, showing the distribution of seismological stations; (b) recorded ground motions (scale of signal amplitude is the same for all the recording) (Pedersen et al., 1994). 6

Figure 1.5: The location of seismological stations near Mt. St. Eynard and recorded ground motions. (a) Section of the ridge, showing the distribution of seismological stations; (b) observed ground motions (Pedersen et al., 1994). 7

Figure 1.6: Local topographic map near the Robinwood ridge and example of spectral ratio analysis. (a) Local topographic map and the distribution of seismological stations on the ridge; (b) spectral ratios derived from an earthquake event A (*M* 2.3) at a distance of 14.1 km (Hartzell et al., 1994). 8

Figure 1.7: Geophones installed on at the Cedar Hill Nursery and raw recorded accelerations. (a) Local topographic map, showing the location of the Geophones installed across the ridge; (b) observed accelerations (Spudich et al., 1996). 9

Figure 1.8: Topographic map of the study area (a) and observed ground motions for three components (b). The interval between neighboring curves is 100 m and the maximum altitude is 1300 m (LeBrun et al., 1999). 10

Figure 1.9: The portable stations installed along the ridge and the spectral ratios derived for several sites. The results show that high ground motion amplification is likely to be attributed to the near-surface geology. Legend defines: a) Recent alluvium; b)'Marnoso-Arenacea' formation; c) 'Scaglia' formation; d) faults; e) seismic stations. (Caserta et al., 2000). 11

Figure 1.10: Arrangement of the array in the study area. (a) Location of the epicenter; (b) topographic map; (c) the profile showing the distribution of the seismometers (Buech et al., 2010). 12

Figure 1.11: The spectral amplitude of the observed ground motions for two horizontal components. The results identify the high topographic amplification, which is obtained at a frequency of 5 Hz (Buech et al., 2010). 12

Figure 1.12: The location of seismic stations used during Phase I of recording (N-S and E-W cross-sectional profiles of the feature shown for profiles A-A' and B-B' , respectively) (Wood, 2013). 13

Figure 1.13: Examples of results from Event 17801 Phase I, Stations 1–10, E-W component: (a) E-W topographic cross section, (b) time records, (c) Fourier amplitude spectra, and (d) standard spectral ratio (Station 1 used as the reference station). Expected topographic frequencies based on simple analytical formulas range from 0.79–2.39 Hz, as indicated by the inset box in (d) (Wood, 2013). 14

Figure 1.14: Topographic map of the instrumented ridge, showing the location of seismic stations 1–10. Cross section A–A′ showing the location of seismic stations placed along a line parallel to the direction of elongation of the ridge. Cross section B–B′ showing the location of seismic stations placed along a line perpendicular to the direction of elongation of the ridge (Stolte et al., 2017). 15

Figure 1.15: A comparison of the spectral ratio in the horizontal direction perpendicular to the axis of elongation of the ridge (Stolte et al., 2017). 15

Figure 1.16: Seismic response of the hill model subjected SV waves at different frequencies range. The topographic contour of 5-foot intervals lines are labeled in white (Bouchon and Barker, 1996). 19

Figure 2.1: Geometry of the numerical model for L_1=200 m and L_2=500 m, D-H=150m. 29

Figure 2.2: Acceleration time history for the Gabor wavelet for the central frequency f=6 Hz. 30

Figure 2.3: Acceleration amplification factor along the surface, for slope angle α=20 ° and slope height h=50 m subjected to a seismic wave with central frequency f=6 Hz. Three lines with different color represent amplification factors of slopes with sharp corners and round corners. 31

Figure 2.4: Acceleration amplification factor along the surface, for slope angle α=45 ° and slope height h=50 m subjected to a seismic wave with central frequency f=6 Hz. Three lines with different color represent amplification factors of slopes with sharp corners and round corners. The green frame encloses the secondary peak. 32

Figure 2.5: Propagation of incident SV waves, reflected SV waves and P waves and diffracted Rayleigh waves in the slope model. 34

Figure 2.6: Amplitude ratio of a reflected P wave as a function of the incident angle. The red arrow points to the critical angle 32.3 °. 34

Figure 2.7: The maximum amplification factor as a function of distance from the crest. (a)-(h) Results from numerical analyses of the slope model with varying slope angles ranging from 10 ° to 45 ° in case of slope height h=50 m. The blue arrows point to the maximum acceleration amplification and the red frame encloses the secondary peak. 36

Figure 2.8: Location of the maximum amplification as a function of the slope angle. For slope angle α>22.2 °, the maximum amplification is observed at a short distance behind the crest. 37

Figure 2.9: Acceleration amplification factor as a function of distance from the crest in case of slope angle α=45 °. (a)-(h) Results from numerical analyses of the slope model with varying slope height ranging from 20 to 90 m. The blue arrows point to the maximum acceleration amplification. 38

Figure 2.10: Acceleration amplification factor as a function of distance from the crest in case of slope angle α=25 °. (a)-(h) Results from numerical analyses of the slope model with varying slope height ranging from 20 to 90 m. The blue arrows point to the maximum acceleration amplification. 39

Figure 2.11: Amplification factor as a function of slope angle. Squares represent results of a slope with the sharp corner; cycles represent results of a slope with corners of small curvature; triangles represent results of slopes with corners of large curvature. 40

Figure 2.12: Amplification factor on the ground surface for slope with sharper corners and slope with round corners (a), the upper round corner and the lower sharp corner (b) and the upper shape corner and the lower round corner (c), for slope angle α=20 ° and slope height h=50 m, subjected to a seismic wave with central frequency f=6 Hz. 41

Figure 2.13: Acceleration amplification factor as a function of slope angle of configurations subjected to a Gabor wavelet with different frequencies for slope height h=50 m. 43

Figure 2.14: Acceleration amplification factor as a function of slope height of configurations subjected to a Gabor wavelet with different frequencies for slope angle α=45 °. 44

Figure 2.15: Acceleration amplification factor as a function of distance from the crest of a slope subjected to a Gabor wavelet with different significant cycles and a Ricker wavelet for a slope angle α=45 ° and slope height h=50 m. 45

Figure 3.1: Schematic map showing the location of the monitoring stations and local topography. (a) Bird's eye view map, indicating the location of the Zigong study area, which is about 246 km away from the epicenter of the 2008, M_w 7.9 earthquake. Several other active faults that frequently trigger seismic activity are also indicated on the map (Xu et al., 2005; Yang, 2008). (b) Local topographic map, showing the location of the

accelerographs installed along a profile across the ridge. (c) Section of the ridge, showing the distribution of the accelerographs along the ridge slope. 50

Figure 3.2: Acceleration histories recorded by the accelerograph array on the Xishan Park ridge during the Wenchuan earthquake. The time history recorded at the #2 station is shorter, but this does not affect the results as time histories windowed from 40 s to 80 s were chosen for analysis. 52

Figure 3.3: Stages of data processing at the #2 (reference) and #7 stations. (a) Windowed accelerations, including the maximum peaks of the SV waves; (b) FFT amplitudes of the windowed accelerations; (c) FFT amplitudes smoothed using a digital FFT filter; (d) spectral amplification ratios at #7 in three directions, respectively. 53

Figure 3.4: FFT amplitude spectra observed at sites #2-8 and spectral ratios relative to station #2 for components East (a, d), North (b, e) and vertical (c, f). 54

Figure 3.5: FFT amplitude spectra (a, b, c) for sites #1 and #2 in three directions and spectral ratios between them (d). The results show that there is significant amplification between 7 and 8 Hz, which is correlated to the soil layer resonance frequency. 56

Figure 3.6: Propagation of incident SV waves, reflected P waves and SV waves and diffracted Rayleigh waves near the slope. 57

Figure 3.7: Statistical shear wave velocity of the bedrock in the study region. 58

Figure 3.8: The FFT amplitude spectra of ground motion obtained from 1D numerical simulations. 58

Figure 3.9: FFT amplitudes of recorded and computed ground motion for each observation station. Similar trends are observed between the field observations and the numerical results. 60

Figure 3.10: Spectral ratios of observed and computed ground motions for each observation station. 61

Figure 3.11: Comparison of spectral amplification ratios for the ridge model subjected to different input motions. 63

Figure 3.12: Amplification of ground motion in terms of a_{rms} ratios at the 8 observation stations with respect to the reference station (#2) for the NS and EW components of the recorded ground motion and the horizontal ones predicted by the ridge model. 65

Figure 4.1: (a) Map showing the location of the Las Colinas landslide and epicentre of the 2001 earthquakes on January 13 and February 13 in El Salvador; (b) a photograph by the United States Geological Survey (USGS) showing the Las Colinas landslide (triggered by the January 13, 2001, M_w=7.7 El Salvador earthquake) that induced long-range movement. 69

Figure 4.2: Observed accelerations (a) at Santa Tecla Station, and the corresponding FFT spectra (b). 69

Figure 4.3: The 3 groups of slope models that were numerically simulated. (a) Actual slope model; (b) model with varying slope angle; and (c) model with varying slope height. 72

Figure 4.4: The spectra of the horizontal accelerations obtained from the numerical analyses of the homogenous and layered models subjected to windowed seismic waves. 73

Figure 4.5: Horizontal peak ground motion maximum amplification as a function of distance from the crest (x=0 corresponds the crest). (a)-(h) Results from numerical analyses for the slope model with varying slope angles from 25 ° to 60 °. 75

Figure 4.6: Illustration of wave propagation, reflection, diffraction and superposition. 76

Figure 4.7: Peak ground motion amplification as a function of the distance from the crest. (a)-(f) Results from numerical analyses of the slope model with varying slope heights ranging from 40 m to 150 m. The red frame encloses the secondary peak. 77

Figure 4.8: Amplification factor as a function of the distance from the crest of four slope models with different geological compositions. (a) Homogenous model; (b) the model in Figure 4.3(a) with brown cinders in place of palaeosol and pyroclastic fall deposits; (c) the model in Figure 4.3(a) with brown cinders in place of palaeosol; and (d) the model in Figure 4.3(a). 78

Figure 4.9: Distribution of peak ground motion amplification along the ground surface behind the crest of the model in Figure 4.3(a), subjected to a Gabor wavelet with a varying central frequency from 1 Hz to 10 Hz. 79

Figure 4.10: Distribution of peak ground motion amplification along the ground surface behind the crest in the model of Figure 4.3(a), subjected to a Gabor wavelet with varying cycles of 1, 2, 4, 6 and 12. 80

Figure 4.11: Horizontal displacement distribution in the real slope model subjected input motion with different peak ground accelerations. (a) PGA=0.1 g; (b) PGA=0.2 g; (c) PGA=0.3 g; (d) PGA equals to the original amplitude. 81

List of Tables

Table 2.1: Parameters controlling the shape of acceleration history 29

Table 2.2: Curvature radii for the models 32

Table 3.1: Material parameters used in the numerical simulations. 59

Table 3.2: Seismic recordings used in the numerical simulation.....62

Table 4.1: Material properties used in the numerical simulations (Bourdeau, 2005) 71

Table 4.2: Parameters for controlling the number of cycles 73

Chapter 1 Introduction

1.1 Motivation

Each year in the world, natural disasters such as earthquakes, landslides, debris flow, tsunamis, and hurricanes cause severe losses of life and property damages, as well as consequential losses from disruption of commerce and destruction of infrastructures slowing the aid to the affected population. According to the statistical investigations on disasters between 1947 to 1980 (Abbott, 2008), 450,048 people lost their lives from earthquakes, 4,519 from the tsunami, and 10,841 from landslides: an average of 14,103 fatalities per year from those events.

Earthquake is one of the most destructive natural events that cause huge losses in a short period of time (Figure 1.1). It is estimated that a minimum of 11 million fatalities were due to earthquakes in the past 4000 years (Korup and Clague, 2009). In the past decades, several catastrophic earthquakes around the world, including the 2006 M_w=6.3 Java (Indonesia) earthquake (Matsuoka and Yamazaki, 2006), the 2007 M_w=8 Peru earthquake (Hébert et al., 2009), the 2008 M_w=7.9 Wenchuan (China) earthquake (Yin et al., 2009), the 2010 M_w=7.0 Haiti earthquake (Hough et al., 2010a), the 2011 M_w=9.0 Tohoku earthquake (Hayes, 2011) and the 2011 M_w=6.3 Christchurch earthquake (Reyners, 2011), have been reported to have induced massive destructions.



Figure 1.1: Collapsed buildings during the 2008 Wenchuan earthquake (http://agnesngoy.blogspot.fr)

Marano et al. (2010) carried out a quantitative analysis of global earthquake casualties using the primary source of detailed fatality information from US Geological Survey's (USGS) Preliminary Determination of Epicenters (PDE). 1,442,342 documented fatalities for all deadly events including shakings, landslides, tsunamis, missing and other reasons between September 1968 and June 2008, were compiled (Marano et al., 2010). As can be seen from Figure 1.2, 1,133,878 (77.66%) were due to shaking-related causes, 70,525 (4.83%) were due to landslides, 238,385 (16.33%) were due to tsunami,

430 (0.03%) were due to other causes, 16,423 (1.12%) were listed missing and assumed dead, and 365 (0.02%) were due to undifferentiated causes. However, the 2004 Great Sumatra–Andaman Islands earthquake and tsunami contributed to the majority of tsunami fatalities with more than 227,000 dead people (Telford and Cosgrave, 2006). In order to eliminate the effect of this single event, the statistical analysis without the Sumatra–Andaman Islands event is presented in Figure 1.2b. This allows a better description of the non-shaking fatal injuries distribution for the covered period of time.

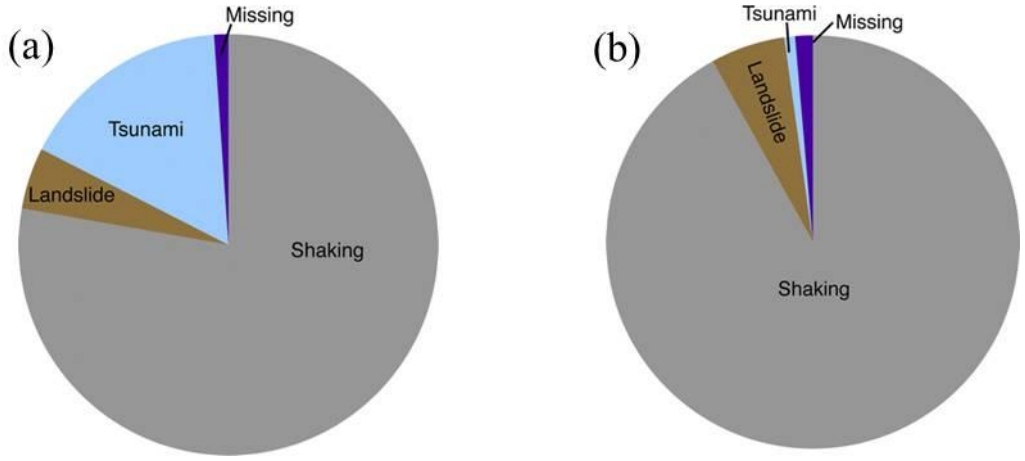


Figure 1.2: Fatality causes for all deadly earthquakes between September 1968 and June 2008. (a) With deaths from the 2004 Sumatra event; (b) without deaths from the 2004 Sumatra event. (Marano et al., 2010)

Figure 1.3 illustrates the part of the fatalities for all deadly earthquakes between September 1968 and June 2008 who are not directly resulting from earthquake shaking. Landslides, which are responsible for 71.1% of the non-shaking deaths, are observed to be the main cause of non-shaking dead people in earthquakes with a removal of the 2004 Sumatra event. In addition, for many specific earthquake events, it is reported that landslides often contribute to more devastation and fatal injuries than direct earthquake effects. For instance, in the 1964 Alaska earthquake, more than 50% of the total cost of damage was caused due to landslides (Wilson and Keefer, 1985). Kobayashi (1981) pointed out that more than half of the fatalities due to earthquakes in Japan between 1964 and 1980 were caused by landslides.

As another example, over 69,000 people lost their lives in the 2008 M_w=7.9 Wenchuan earthquake and more than 370,000 were reported injured, with over 18,000 listed as missing as of July 2008 (Dai et al., 2011). Hundreds of thousands of landslides were triggered over a broad area during this earthquake. Some of them buried villages or even cities, blocked the roads and dammed the rivers. It was estimated that about 20,000 amongst the 69,000 fatalities are caused due to landslides during the Wenchuan earthquake (Yin, 2008).

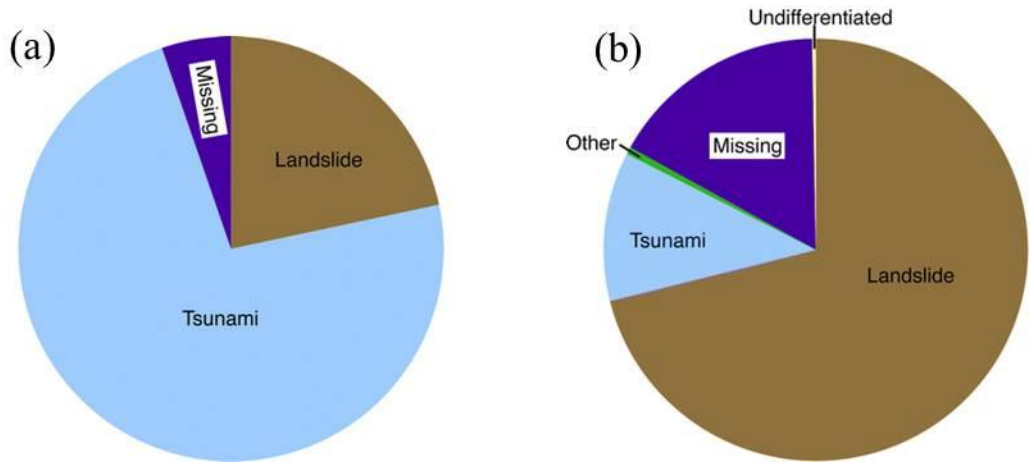


Figure 1.3: Non-shaking fatalities for all deadly earthquakes between September 1968 and June 2008. (a) With dead people from the 2004 Sumatra event; (b) without dead people from the 2004 Sumatra event. (Marano et al., 2010)

Topographic effects, e.g. the amplification, de-amplification, or frequency modification of ground motion in the vicinity of topographic features, have drawn widespread attention in the scientific community. Certain topographic irregularities scatter, diffract or focus incident seismic waves, resulting in large amplifications or reductions of ground motions. In particular, severe damages at the top of hills or slopes during earthquakes have been noticed to be induced by site effects. Extremely high movement intensities are often observed near topographic irregularities and may be responsible for landslides triggering. A typical example of the observed "topographic effects" is the extraordinary damage patterns on topographic ridges during the 2010 M_w 7.0 Haiti earthquake, where destructions were concentrated on ridges or other topographic features (Hough et al., 2010a).

Historically, site effects have been observed in a lot of earthquake events, such as the 1989 Loma Prieta earthquake (Wald et al., 1991), and the 2010 Haiti earthquake (Assimaki and Jeong, 2013; Hough et al., 2010a). In these events, typical ground motion modifications (most of them are amplifications) are observed near topographic irregularities. This suggests that relief morphology, such as hills, slope and ridges, plays a significant role in modifying seismic waves field near the topographic features. The amplification of ground motion due to topography may be also increased by the resonance of seismic wave-field inside the layer depending on soil layer thickness (comparable with the seismic wavelength). Sometimes, the instructive interference occurs due to resonance when seismic waves propagate into the soil layer at a specific frequency (resonance frequency). Furthermore, ground motion amplification may happen related to special reliefs, where different physical phenomena such as wave reflection, infraction or diffraction can occur and could aggravate destruction. It has been reported for a long time by researchers (Bonamassa and Vidale, 1991; Caserta et al., 2000; Çelebi, 1987; Donati et al., 2001; Griffiths and Bollinger, 1979; Hartzell et al., 1994; Pedersen et al., 1994), that widespread localized damage often occurs at special sites where always consists of topographic irregularities. Both field observations (Caserta et al., 2000; Spudich et al., 1996; Stolte et al., 2017; Tsai and Huang, 2000; Wood, 2013) and numerical studies (Assimaki et al., 2005; Bouchon, 1973; Lenti and Martino, 2012; Sánchez-Sesma et al., 1982; Wong and Jennings, 1975; Zahradník and Urban, 1984) suggest that topographic effects are very important for the seismic hazard evaluation at the top of ridge or very steep hillsides. Earthquake ground shaking, involving effects of local site conditions, could cause huge destructions. Such local conditions must be taken into account when engineers design criteria of any infrastructure project in seismic areas. Especially at special sites such

as mountainous areas, topographic effects often interact with soil amplification and thus may aggravate the earthquake-induced disaster.

In order to evaluate ground motion amplifications, ground motion amplification factors or spectral amplification factors derived from surface acceleration-time series, are often provided based on the dynamic response of the local site conditions. Researchers have focused on studying the effects of topography on ground shakings by using numerical and analytical methods. These research results give very valuable insights into the understanding of ground motion amplification. It was also shown that many factors, such as topographic geometry, the presence of the soil layer at the slope surface, three-dimensional (3D) topography geometry, wave-field incident angle and orientation, influence the magnitude of ground motion amplifications and even the frequencies at which these effects are observed. These effects are usually evaluated by site response analysis, which refers to the seismic wave propagation from the bedrock to the ground surface. In most cases, one-dimensional (1D) site response analysis is widely used to evaluate the effect of soil conditions on ground motion. It is of practical interest because vertically propagating shear waves (SV) dominate the seismic wave-field. However, in order to assess the topographic effect, two-dimensional (2D) and even 3D numerical analysis must be conducted based on model profile subjected to seismic signal input motion.

Most of the numerical studies are performed using simplified models such as a homogeneous model with idealized 2D geometry or simple 2D model with soil layering. As a consequence, numerical modeling usually gives lower amplifications than those observed in instrumented field studies. There are many reasons, such as the presence of a loose soil layer at the surface, wave-field incident angle and orientation, wave type, and three-dimensional (3D) topography geometry (Geli et al., 1988; Paolucci, 2002; Semblat et al., 2002), for the discrepancies between observed results and numerical results, but the most important of them are uncertainties in the subsurface properties used in numerical simulations and the lack of adequate knowledge of topographic features. In this respect, a few studies have used 3D models with more realistic geological and geomorphological site conditions to compute ground motion amplifications due to surface topography (Chaljub et al., 2010; Lee et al., 2009; Maufroy et al., 2012). Such 3D numerical modeling is supposed to predict ground motion amplifications in a more accurate and realistic way and get results closer to what could be observed in the field, but they are more complex and more time and money consuming than the 2D studies.

Although research works have been done on topographic irregularity, a study on the phenomenon related to small-scale factors, 3D effects, and high-frequency seismic waves, is still needed. In this document, we address the issue of ground motion amplifications due to site effect using numerical models in terms of variation of the geometry and subsurface geology. The effects of topography, geology and input motions are assessed by quantifying ground motion amplification along slope ground surface, and interactions between topographic amplification and surficial soil amplification are also discussed. Numerical simulations have also been performed on two case studies where field measurements were available in order to compare the results of numerical modeling with field data and to study the reason why differences may occur.

1.2 Literature review

Seismic waves have been observed being modified by local geological and topographic conditions for a long time. The phenomena of ground motion modifications are widely known due to site effects and they can result in significant differences in the characteristics of shaking at a given site.

Site effects mainly include four factors. (1) The stiffness of the soil or rock at the local site (Atkinson and Cassidy, 2000; Bouckovalas and Kouretzis, 2001): Seismic waves travel faster through stiff sediments than through softer ones; when waves spread from deep (often harder) to shallow (softer) rocks, the seismic waves slow down and the amplitude of seismic waves increases as the energy is accumulated. The higher the contrast on stiffness, the larger the seismic amplifications. (2) The presence of a weak soil layer (Assimaki et al., 2005; Bauer et al., 2001): as a consequence of the contrast in the impedance, seismic waves are trapped in soil layers so that it produces higher amplitudes and longer durations. The effect is strongly dependent on the relationship between the wave frequency (wavelength) and the thickness of the soil layer. (3) Topographic conditions (Fukushima et al., 2000; Geli et al., 1988; Meunier et al., 2008; Paolucci, 2002; Spudich et al., 1996): topographic geometries including slopes, ridges, and canyons have a significant influence on the ground motion characteristics and seismic intensity; a higher peak horizontal acceleration is often recorded by accelerometer installed at the top of a ridge or hill than those recorded by nearby accelerographs at surrounding areas. (4) Geological structures (Bertrand et al., 2011; Cormier and Spudich, 1984): sedimentary basins and dipping layers are expected to focus or defocus seismic waves and therefore to have a significant effect on ground motion modifications. Seismic waves travelling through faults or sedimentary basins from bedrock with high shear velocity will slow down and get larger amplitude of the earthquake waves. The high density contrast between the sedimentary material in the basin and the surrounding materials induces wave trapping into the basin which will combine and result in stronger and longer ground motion.

1.2.1 Topographic amplification

1.2.1.1 Instrumental observations

Charles Darwin was one of the first to explain the phenomena of fractured and displaced soil on narrow ridges using topographic effects (Barlow, 1933), during the 1835, February 20, Chilean earthquake. Afterward, the observation of churned ground, ground fissures, and overturned boulders near the topographic features subjected to strong ground shaking were attributed to topographic effects (Boore, 1972; Plafker et al., 1971; Ponti and Wells, 1991). Field observations on topographic amplifications have been improved for fundamental data acquisition and have been carried out in many case studies (Hartzell et al., 1994; Pedersen et al., 1994; Spudich et al., 1996). Nowadays the array of velocimeter or strong motion networks can be used to record a given seismic event at different sites and allow to easily compare the ground motion from the same seismic event and thus to evaluate topographic effects.

Topographic amplification can be computed in the time domain based on ratio between the peak ground motion recorded at a given site and those recorded at a reference site, or in the frequency domain by comparing the frequency spectra. However, sometimes physical phenomena related to seismic wave propagation are hard to be explained in the time domain since they are strongly frequency-dependent. Frequency domain analysis such as spectral density and frequency response is an effective way to understand process characteristics and the various phenomena that cannot be explained in the time domain. The Standard Spectral Ratio (SSR) (Borcherdt, 1970) applied on earthquake data are the most frequently used spectral analysis methods. SSR is defined as the spectral ratio of the specific site with respect to a reference site on bedrock. The key step is to choose the available reference site, which cannot be affected by any topographic effects. Based on this idea, topographical

and geological amplifications that occurred during past earthquakes are investigated by instrumental studies and several cases are presented hereafter.

Pedersen et al. (1994) carried out two field experiments to evaluate local amplification and wave diffraction on a ridge (Figure 1.4). They obtained seismic records of local and regional earthquakes. The recorded ground motions were processed both in the frequency domain and in the time domain. Numerical analyses were also performed with two-dimensional models by the indirect boundary element method for comparison. In the first experiment, amplification ratios of 1.5 to 3 at the ridge top with respect to the base of the ridge were observed by Fast Fourier Transform analysis. It was also observed that amplifications of horizontal components are slightly higher than amplifications in the vertical direction. For different earthquakes, the spectral ratios seem stable. The theoretical spectral ratios from numerical analyses were found in good agreement with observed spectral amplifications.

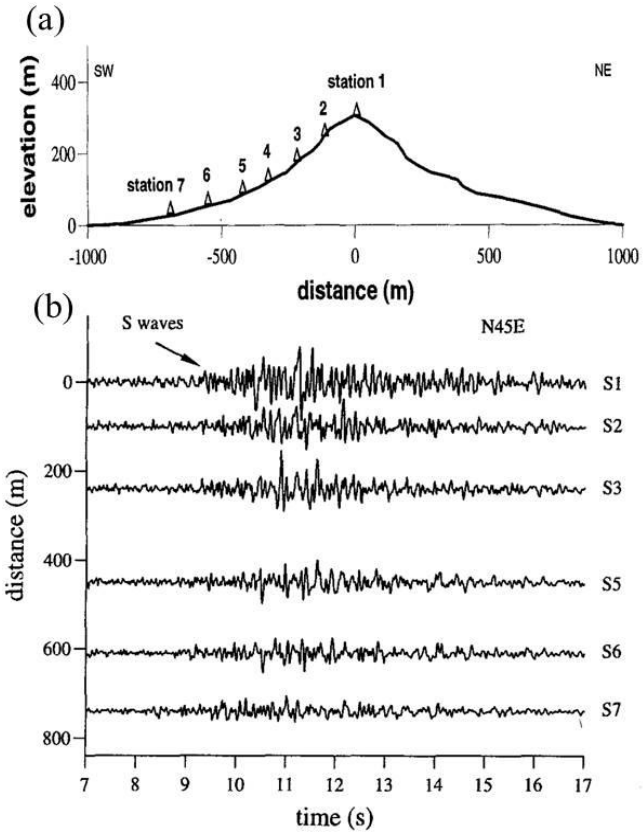


Figure 1.4: The location of seismological stations near Sourpi and example of observed ground motions. (a) Section of the ridge, showing the distribution of seismological stations; (b) recorded ground motions (scale of signal amplitude is the same for all the recording) (Pedersen et al., 1994).

In the second experiment, Pedersen et al. (1994) arranged 5 seismological stations along a ridge, which presents a very steep cliff at its top and is filled with soft deposit at the ridge bottom. Recording stations were installed along the slope and numbered 1 to 7 from the top to the bottom. Strong soil amplifications were observed at stations 1, 4, and 5 (Figure 1.5), as the amplitudes of ground motion recorded at stations 1, 4, and 5 were much larger than those recorded on rock sites (stations 2 and 3). To study the pure topography-induced effects, stations 2 and 3 were selected for spectral ratio analysis. The spectral amplitude ratio at station 3 with respect to station 2 was calculated with a widowed

ground motion of frequency range larger than 2 Hz. A broadband relative amplification between 2 and 4 Hz was observed for the vertical component.

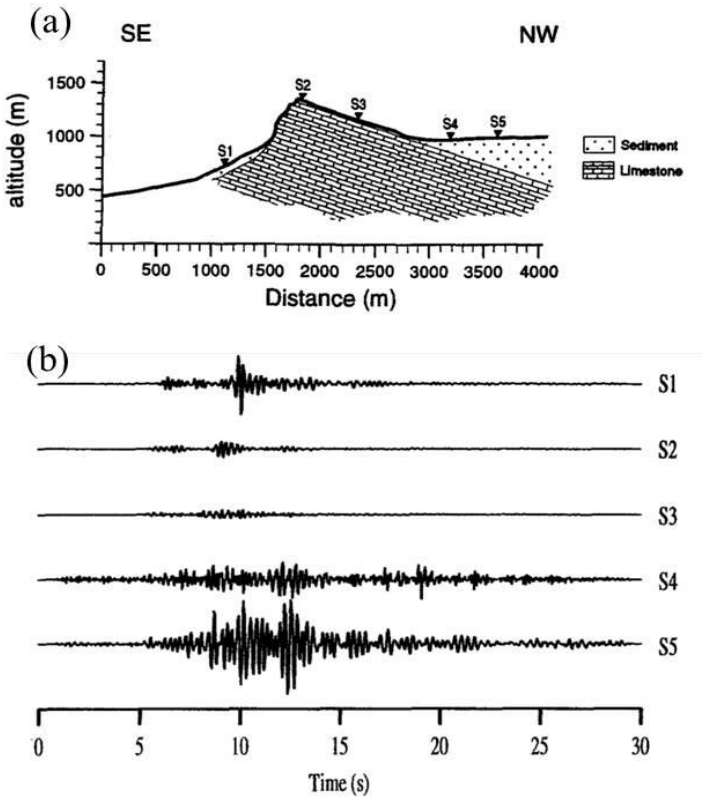


Figure 1.5: The location of seismological stations near Mt. St. Eynard and recorded ground motions. (a) Section of the ridge, showing the distribution of seismological stations; (b) observed ground motions (Pedersen et al., 1994).

Severe structural damage and ground cracking on a ridge during the 1989 Loma Prieta earthquake lead to carry out research works focused on site effect evaluation in this region. Hartzell et al. (1994) deployed a dense array of three-component accelerographs on Robinwood ridge 7.3 km northwest of the epicenter for investigating the cause of severe earthquake damage observed on the ridge crest. Ground motions recorded by the array allowed spectral analyses considering the base as a reference site (Figure1.6). Amplification with spectral ratios from 1.5 to 4.5 was observed in frequencies ranging from 1.0 to 3.0 Hz. The reason can be attributed to a combination of local geological effects and topographic amplification. In the higher frequency range, high amplification can be detected up to 5.

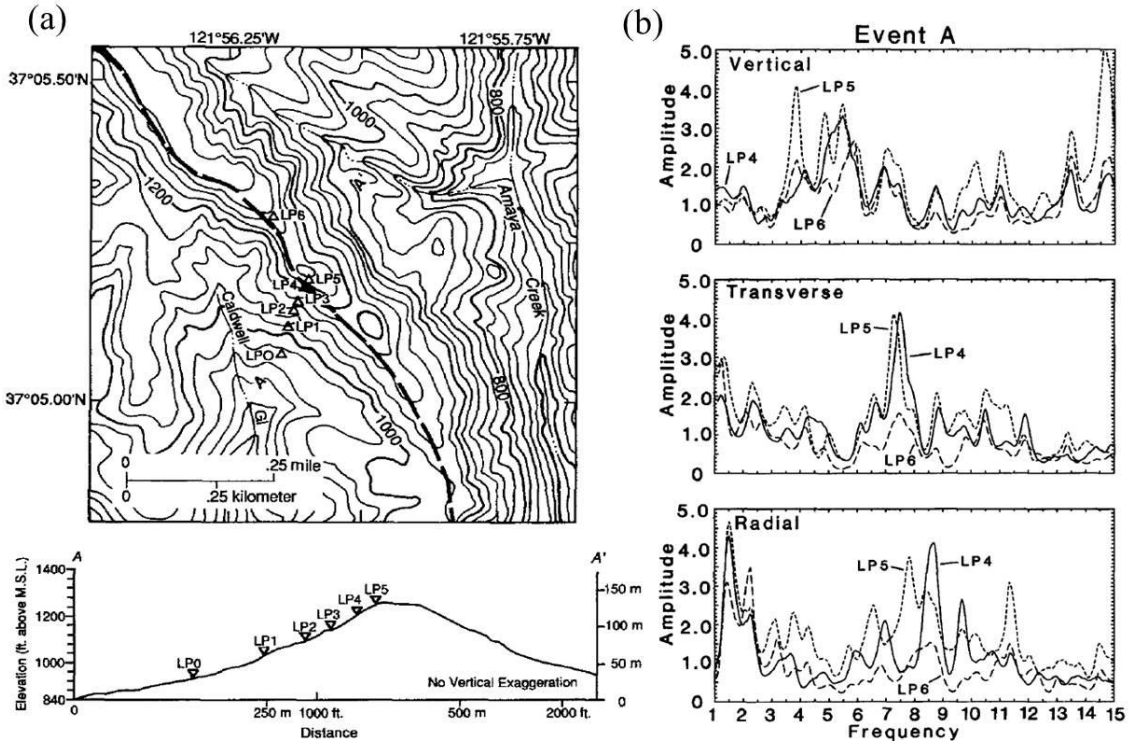


Figure 1.6: Local topographic map near the Robinwood ridge and example of spectral ratio analysis. (a) Local topographic map and the distribution of seismological stations on the ridge; (b) spectral ratios derived from an earthquake event A (*M* 2.3) at a distance of 14.1 km (Hartzell et al., 1994).

In order to investigate the cause of a high observed acceleration of 1.78 g at the Cedar Hill Nursery (Figure 1.7), Spudich et al. (1996) installed 21 three-component geophones in six radial lines with an average distance between the sensors of 35 m on the hill. The radial lines are oriented in six directions, which are the north (N), south (S), east (E), west (W), northeast (NE), and southeast (SE). The raw recorded ground motion can also be seen in Figure 1.7. The results identify the directional topographic effect and the resonance frequency at a transverse direction is 4.5 Hz. The amplification ratio of 4.5 at the hilltop is obtained in the horizontal direction. Comparisons of field observations with theoretical results indicate that the 3D shape of the hill and its internal structure are important factors affecting its response.

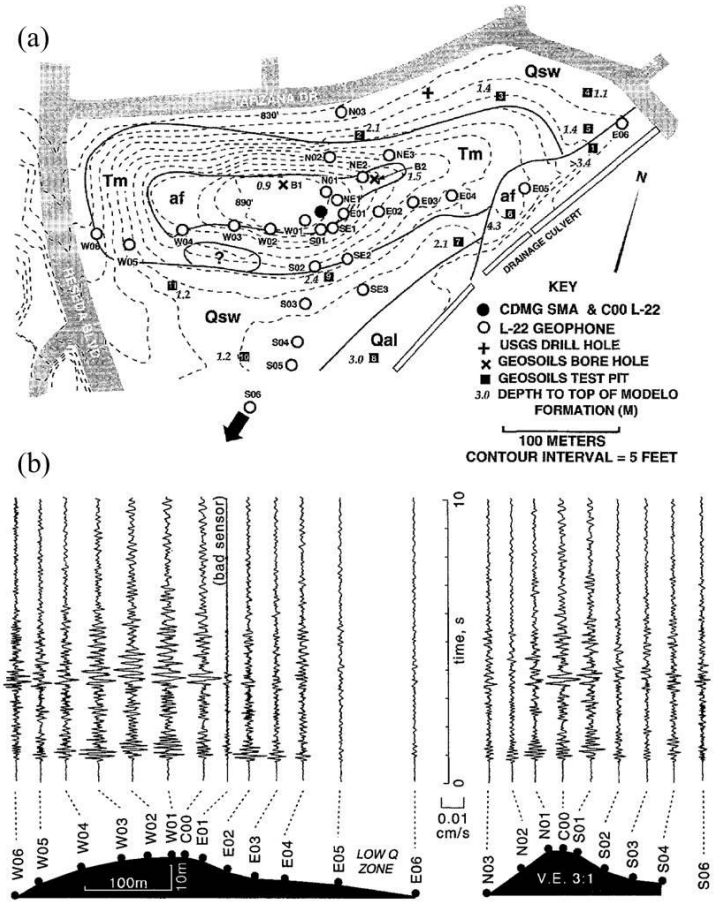


Figure 1.7: Geophones installed on at the Cedar Hill Nursery and raw recorded accelerations. (a) Local topographic map, showing the location of the Geophones installed across the ridge; (b) observed accelerations (Spudich et al., 1996).

An experiment for investigating the effects on the seismic ground motion on a hill near Corinth (Greece), with large dimensions of 6 km long, 3 km wide and 700 m high, was performed by LeBrun et al. (1999). In this experiment, 7 accelerometers were installed along the hill, and the recorded ground motions were analyzed with different methods: the standard spectral ratios (SSR) and the horizontal to vertical spectral ratios both calculated on ambient noise (HVNR) and earthquake data (RF). HVNR is based on the spectral ratio between the horizontal and vertical components of a ground motion recorded at the same station. This method is mainly applied to microtremors or, sometimes, to strong motions (Wen et al., 2014) and allows the estimation of the predominant resonance frequency at the local site under consideration. Two assumptions are established for using the HVNR method. The first one is that the vertical component of the tremor is mostly composed of Rayleigh waves. The second one is that the ratio between horizontal and vertical spectra of surface tremor is supposed to be as an approximate transfer function. The experiment results show that the amplification at the resonant frequency (around 0.7 Hz, which is given by $f = 0.4 * \beta / l$, with β being the S wave velocity and l being the half-width of the topography (Geli et al., 1988)) is relatively low; however, it is found that a large amplification (up to a factor of 10) at 3Hz is obtained at one of the two stations installed at the top of the hill. The H/V spectra clearly suggested the fundamental frequencies of a hill but it does not accurately predict the amplification in a wide range of frequency.

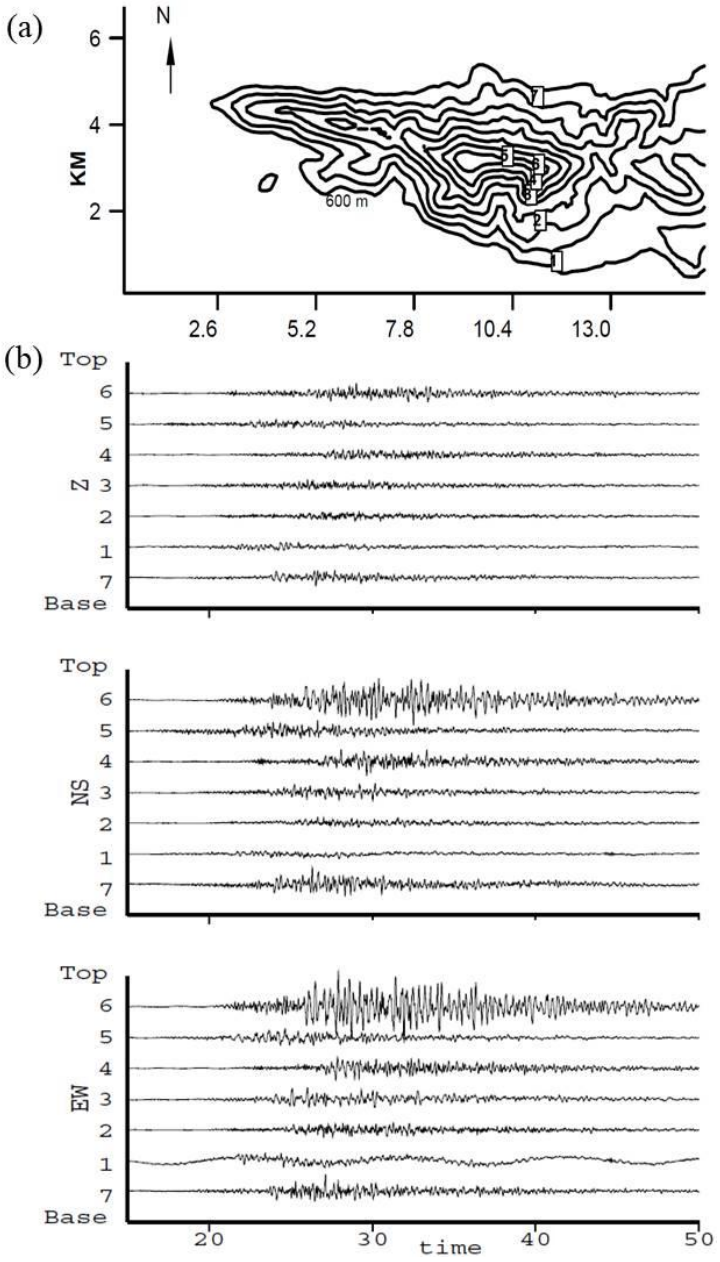


Figure 1.8: Topographic map of the study area (a) and observed ground motions for three components (b). The interval between neighboring curves is 100 m and the maximum altitude is 1300 m (LeBrun et al., 1999).

After the earthquake occurred on 26 September 1997 in central Italy, the historic center of Nocera Umbra, lying on top of a 120 m high hill, was found diffusely damaged. Some recently built houses even suffered a higher level of damage on the top of the hill, where the marly limestone of the 'Scaglia' formation crops out. Caserta et al., (2000) investigated the possible correlation between ground motion amplifications and the observed seismic damages. Five portable stations were deployed in eight sites along a 2.5 km profile to record the aftershocks (Figure 1.9). They analyzed the ground motion with different methods: the classical spectral ratios and the horizontal to vertical spectral ratios calculated both on noise and earthquake data. Amplifications of 2 to 3 at a frequency range of 2.5-5 Hz were obtained at the top of the hill. In the frequency band around 20 Hz, an extremely high value of amplification of 20 for the standard spectral ratio was observed at station 5 at the middle of the ridge. However, at frequencies lower than 10 Hz, the high amplification was obtained at stations 1 and 2

located on a flat site. This suggests that the near-surface geological layers are probably responsible for the observed amplifications.

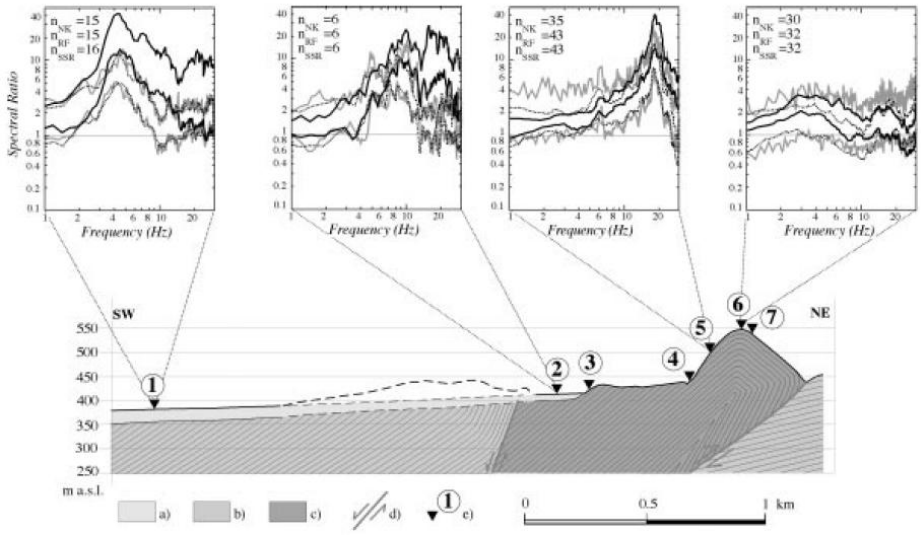


Figure 1.9: The portable stations installed along the ridge and the spectral ratios derived for several sites. The results show that high ground motion amplification is likely to be attributed to the near-surface geology. Legend defines: a) Recent alluvium; b)'Marnoso-Arenacea' formation; c) 'Scaglia' formation; d) faults; e) seismic stations. (Caserta et al., 2000).

Buech et al. (2010) deployed seven seismometers along a ridge, which is a 210 m high, 500 m wide, and 800 m long hill (Figure 1.10). Seismic records of local and regional earthquakes were recorded and analyzed using three methods: comparisons of the recorded peak ground accelerations, power spectral density analysis, and standard spectral ratio analysis. Both time and frequency domain analyses show that high topographic amplifications occurred along the ridge with respect to the reference motion recorded at the station rh0 located on the flat base and the maximum amplification ratio in the frequency domain at station rh6 can reach 11. The spectral ratios show that a maximum response occurred for frequencies of about 5 Hz (Figure 1.11).

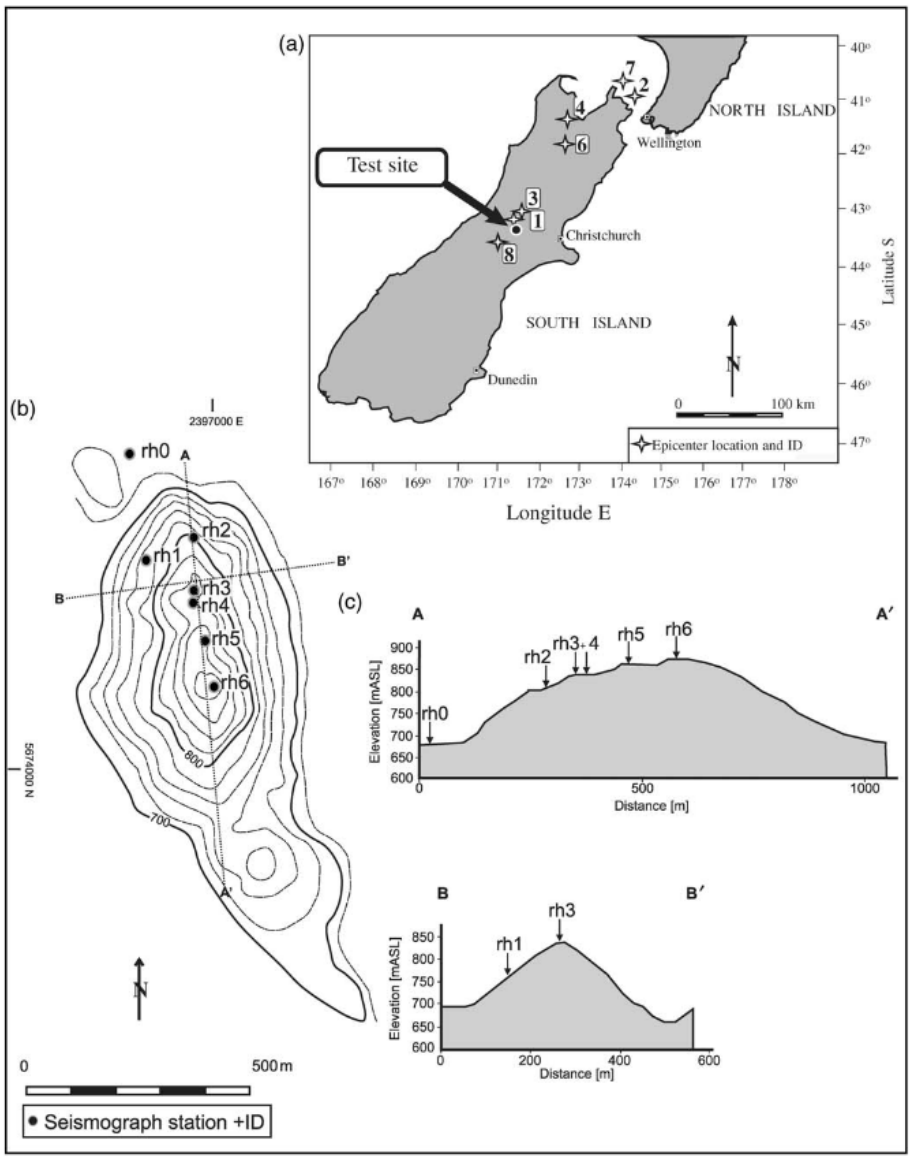


Figure 1.10: Arrangement of the array in the study area. (a) Location of the epicenter; (b) topographic map; (c) the profile showing the distribution of the seismometers (Buech et al., 2010).

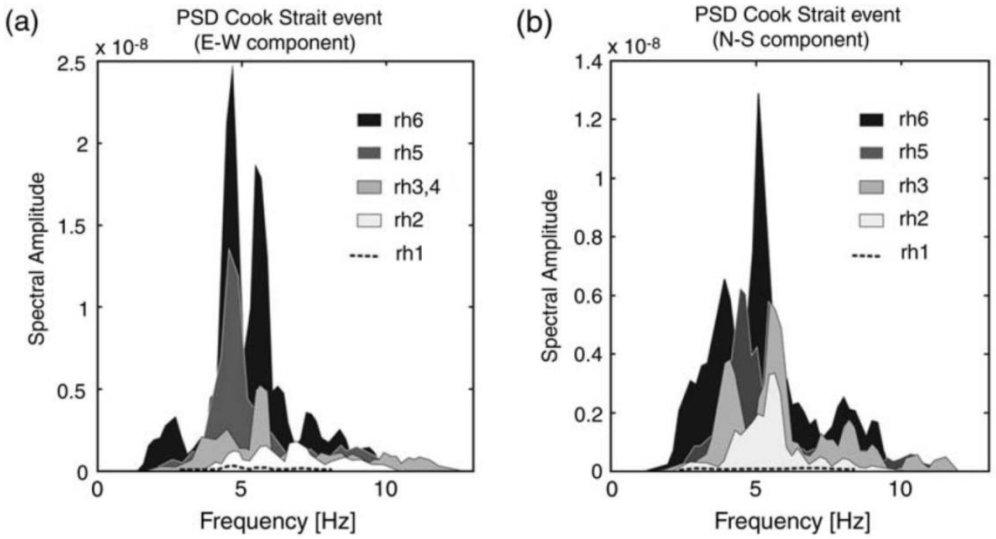


Figure 1.11: The spectral amplitude of the observed ground motions for two horizontal components. The results identify the high topographic amplification, which is obtained at a frequency of 5 Hz (Buech et al., 2010).

Severe building destructions during the 2011 February M_w 6.2 and the June M_w 6.0 Canterbury earthquake (New Zealand) were considered to be caused by topographic effects, because damage patterns suggested that ground motion amplifications due to localized features have likely been responsible for the most severe effects (Kaiser et al., 2013). To evaluate the site effects on ground motion amplifications, temporary arrays were deployed at four sites. The ground motions were collected from aftershocks in order to characterize the seismic site response and to assess amplification from lithological and topographic factors. The initial analyses from records at two of the sites suggested significant complexity in ground motion amplification and revealed polarization over small distances within the arrays for any given event.

In 2003, dense arrays of seismometers were deployed at a steep mountainous terrain in Central-Eastern Utah (USA) in two directions with varying slope angles and topographic features (Figure 1.12) to record ground motions and thus to assess site effect on ground motion amplification (Wood, 2013). The researcher analyzed the ground motions recorded at the mountainous site and assessed changes of the frequency content and amplitude of available ground motions affected by topographic features. The results show that the instrumented peak ground motions were affected in a narrow frequency range by the effects of topography (Figure 1.13). It is also clear that the physical phenomenon of topographic effects was not only observed at the crest of the slope, but also along the slope and at the base of the slope. The highest amplification factors were produced at the crest of the slope while amplifications decreased downwards along the slope. At the toe of the slope, deamplification occurred.

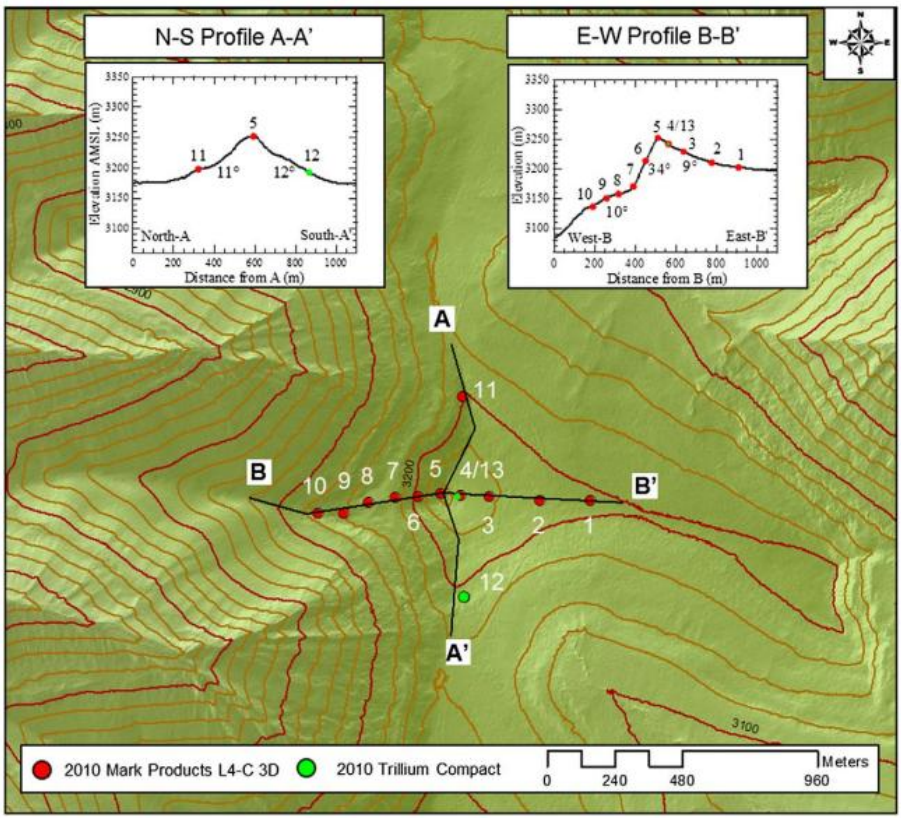


Figure 1.12: The location of seismic stations used during Phase I of recording (N-S and E-W cross-sectional profiles of the feature shown for profiles A-A' and B-B' , respectively) (Wood, 2013).

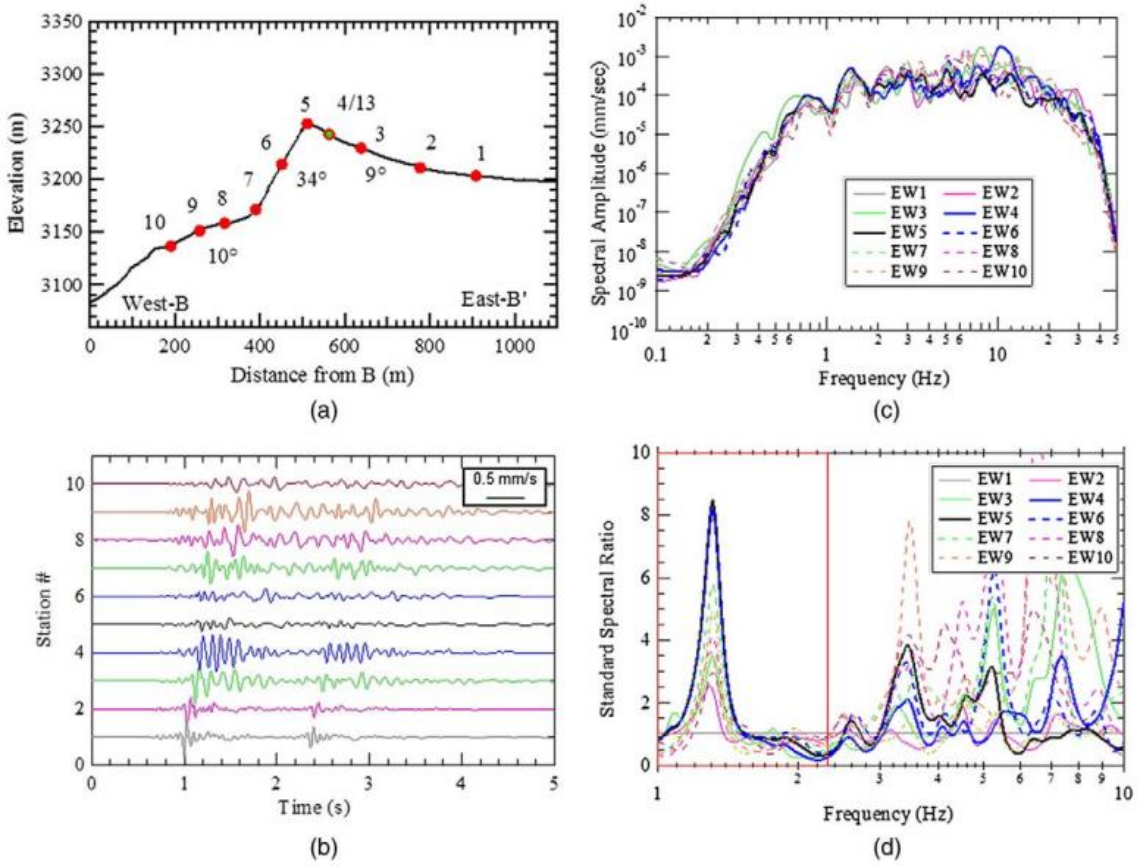


Figure 1.13: Examples of results from Event 17801 Phase I, Stations 1–10, E-W component: (a) E-W topographic cross section, (b) time records, (c) Fourier amplitude spectra, and (d) standard spectral ratio (Station 1 used as the reference station). Expected topographic frequencies based on simple analytical formulas range from 0.79–2.39 Hz, as indicated by the inset box in (d) (Wood, 2013).

Recently, an experimental study, investigating potential topographic amplifications of ground motion, was carried out on a soft rock ridge of a height of 50 m, which is located at Los Alamos National Laboratory, New Mexico (Stolte et al., 2017). Seismic arrays of ten portable broadband seismograph stations were deployed across the ridge for monitoring ambient vibration data during 9 hours. By comparing spectral ratios of ambient noise recordings, clear evidence of topographic amplification was obtained at the slope crest of the instrumented ridge. The predominant frequency of the ridge observed from the spectra of experimental recordings is in agreement with the theoretical estimation based on its geological and geometrical features. The results suggest that ambient vibrations monitoring is a feasible way to quantify the frequency range of topographic amplifications. Spectral analyses by using standard spectral ratio, median reference method, and horizontal to vertical spectral ratio, were performed to quantify topographic effects, as well as to make comparisons. A topographic map can be seen in Figure 1.14 and a comparison of spectral ratios is illustrated in Figure1.15.

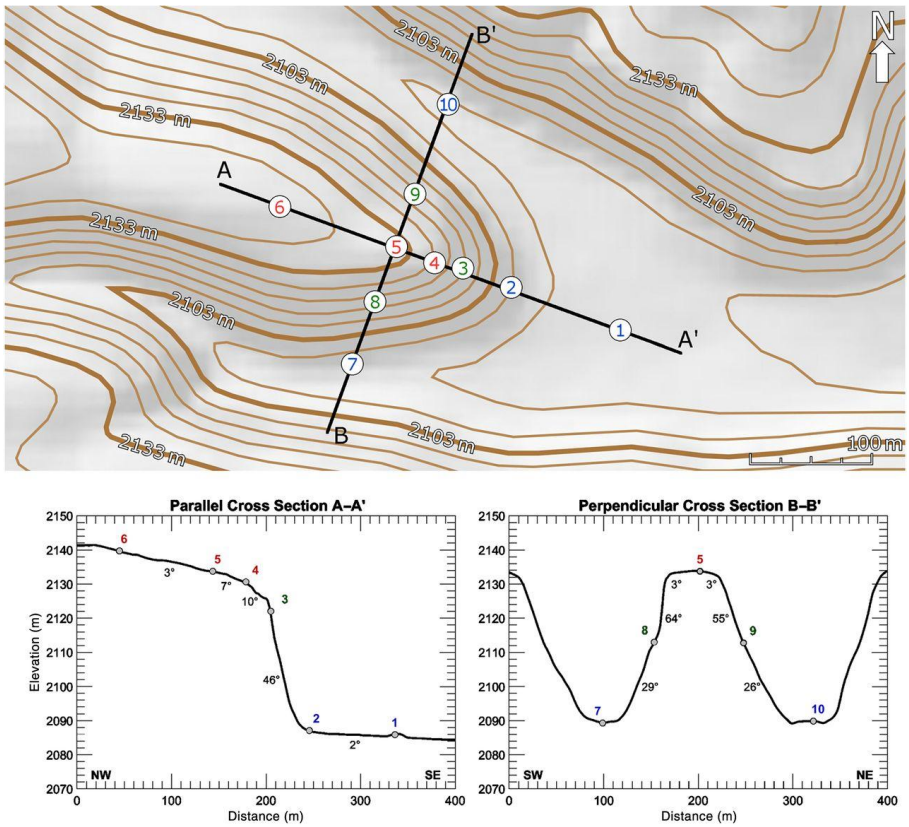


Figure 1.14: Topographic map of the instrumented ridge, showing the location of seismic stations 1–10. Cross section A–A′ showing the location of seismic stations placed along a line parallel to the direction of elongation of the ridge. Cross section B–B′ showing the location of seismic stations placed along a line perpendicular to the direction of elongation of the ridge (Stolte et al., 2017).

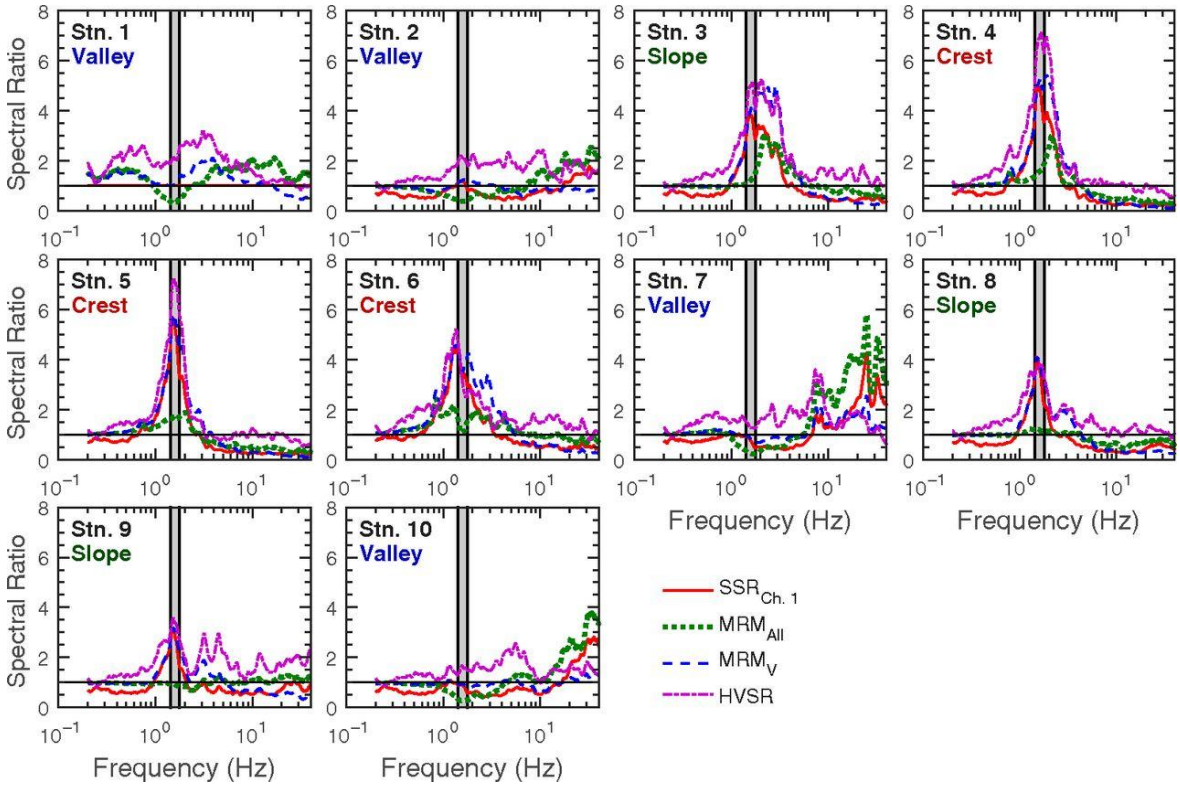


Figure 1.15: A comparison of the spectral ratio in the horizontal direction perpendicular to the axis of elongation of the ridge (Stolte et al., 2017).

1.2.1.2 Theoretical analyses

Volume waves (P, S) and surface waves (Rayleigh, Love) involved in a seismic event can be generated or transformed when earthquake waves travel through a medium with geological irregularity or at the surface of the earth due to wave interferences, reflections and diffractions. Simplified theoretical equations are often used to evaluate topographic effects on wave transmission near the ground surface at a given site. Using these simplified methods, simple homogeneous 1D or 2D problems are often studied when subjected to vertically propagated SV waves or sometimes SH waves. However, under certain circumstances, these analyses can quickly provide a good approximation that can be applied to deal with real engineering situations and thus are welcome to solve engineering problems. A review of the most widely used theoretical methods to evaluate ground motion amplification due to topographic features is presented hereafter.

In 1960, Ambraseys presented a theoretical study for analyzing the shear response of a truncated 2D elastic wedge subjected to an arbitrary disturbance (Ambraseys, 1960). Elastic and constant rigidity of the wedge is assumed, and only shear movement along the wedge faces was considered for the equation derivation. He derived equations to estimate the response in shear of the wedge-shaped elastic solid, which is verified to be suitable to earthquake engineering problems, in particular to those dealing with the seismic stability of earth dams and embankments.

Shortly afterwards, Gilbert and Knopoff developed a perturbation solution for 2D elastic geometry, in particular for the case of irregularities with gentle curvature (Gilbert and Knopoff, 1960). The approximation is based on the assumptions of small magnitude and slope of the irregularity. The irregularity is replaced by an equivalent stress distribution. This method was used by Hudson for a case study of a small slope. By analyses using this approach, results with respect to Rayleigh waves are found to be in good agreement with observations, even for topographic irregularities characterized by slope angles greater than 25 °or 30 ° (Hudson and Boore, 1980).

Because the conversion mode of SH waves is simpler than the generation of P, SV or Rayleigh waves, researchers have mainly studied the wave propagations due to topographic effect using incident SH waves. Trifunac (1971) investigated a semi-cylindrical alluvial valley for characterizing surface motion in case of incident plane SH waves. He showed that the complex phenomena of wave-interferences are characterized by wave patterns and rapid changes in the ground-motion amplification are observed along the free surfaces. These phenomena depend on the incidence angle of SH waves. Then, Wong and Trifunac (1974) performed another analysis on a semi-elliptical canyon to examine the dependency of ground motion amplifications on the surface and near the canyon. The results suggest that the amplification ratios depend on the incident angle of the input motion and on the ratio between the width of the canyon and the wavelength of SH waves.

At the meantime, Aki-Larner method (Aki and Larner, 1970) was developed and applied to a study of the seismic response of sediment-filled valleys subjected to SH waves (Bard and Bouchon, 1980). The results confirmed that the Aki-Larner technique is a powerful and reliable tool to study scattering effects of earthquake waves in the time domain, in particular when wavelengths of the input motion are comparable to the size of the structural feature. They also demonstrated that a non-planar interface has a great effect on ground motion amplifications due to the generated Love waves which were observed to have much larger amplitudes than those of input motion. Moreover, the duration of the ground shaking in the basin was much longer due to the presence of a high-velocity contrast between the surface layer and bedrock.

In 1985, Sánchez-Sesma (1985) derived and applied Macdonald's solution to study the diffraction of SH waves propagating in a wedge-shaped elastic medium. It was observed that the motion near the wedge was substantially affected by the wedge angle. Paolucci (2002) estimated the fundamental frequency of homogeneous triangular mountains using the Rayleigh's method and then evaluated topographic amplification on this relief by the spectral element method. The results show that topographic irregularities with significant elongations are like to induce wide-band frequency amplifications while isolated cliffs are responsible for amplifications at a narrow range of frequency. Later, Smerzini et al. (2009) presented several analytical methods based on the expansion of Bessel and Hankel wave functions in order to study the anti-plane seismic response of various types of underground structures. Moreover, they also applied the Rayleigh's method to verify that the ground motion amplification was dominated by the fundamental resonance frequency of soil profile.

1.2.1.3 Numerical modeling

Numerical modeling analysis has been widely developed to predict ground motion modifications due to topographic effects. 1D, 2D and more recently 3D numerical simulation, for various steep reliefs such as slopes, ridges, cliffs, and mountains, have been carried out for assessing topographic effects on ground motion (Assimaki et al., 2005; Geli et al., 1988). Thank to the development of computer technology with the updates of software, more and more complex models have been designed. These research works used the finite difference method (Lenti and Martino, 2012; Zahradnik and Urban, 1984), the finite element method (Assimaki et al., 2005), the boundary method (Sánchez-Sesma et al., 1982), the discrete wavenumber method (Bouchon, 1973), and the Aki-Larner method (Geli et al., 1988; Wong and Jennings, 1975). Below is a review of studies that have been performed using numerical modeling.

In 1972, Boore carried out finite difference calculations to analyze the propagation of SH wave in a step-like slope. The results show that topography plays an important role in seismic wave propagation, especially when the wavelengths are comparable to the characteristic model size like slope height (Boore, 1972). It also showed that ground motion changes due to topographic effect vary from amplification to deamplification depending on the frequency contents of the input motion. Ground motion amplifications can reach 75% compared to the motions observed at a site without the effect of topography. Later, Boore (1973) conducted calculations for simple geometrical models and compared the results with observed data near Pacoima Dam during 1971, February 9th, San Fernando earthquake. The results suggest that topography has a large influence on ground motion recorded on the ground surface. The ground motion amplification is significantly frequency-dependent, and the amplification ratio for higher frequency excitation can reach 1.5 times as much as those results due to lower-frequency input motion. Afterwards, numerical investigations of topographic effects on slope model subjected to vertically incident SV waves and P waves were performed using the finite difference method (Boore et al., 1981). The results indicated that scattered Rayleigh waves were considered to be mainly responsible for causing ground motion amplifications. The amplitudes of Rayleigh waves can be as large as 0.4 times the amplitude of the incident waves.

In 1973, Bouchon performed a parametric study on topographic effects using the Aki and Larner method in order to investigate the effect of topography on the surface motion in the cases of incident SH, P and SV waves (Bouchon, 1973). In the numerical simulations, the variation of the topography, the incident angle of input motion, and wavelength of seismic waves were considered. Results showed that the surface topography has a great influence on surface displacement. In the case of a ridge,

ground motion amplification is observed near the top, while deamplification occurs near the bottom. For a case study of the Pacoima Dam, the high accelerations recorded during the San Fernando earthquake are supposed to be amplified by a ratio of 1.5 due to the effect of topography.

Later, Bard used the Aki-Larner technique to conduct a numerical study aimed at investigating the respective influences of surface geometry, elastic parameters and incident wave characteristics on ground motion (Bard, 1982). The topographic effects are found to be extremely depended on the incident wave characteristics and expressed a great complexity. When the wavelength of the incident waves is similar or slightly shorter than the mountain width, ground motion amplification occurred systematically. It is also showed that the complex wave scattering is frequency-dependent and is likely to be closely correlated to the horizontal scale of the topographic structure. Moreover, higher ground motion amplification was observed for incident S waves than for P waves.

In 1983, Ohtsuki & Harumi numerically studied the effect of topography and surface geology on the ground motion. Numerical simulations were made for several types of topography, such as a cliff, a cliff with a soft layer and filled land, using finite element method (Ohtsuki and Harumi, 1983). Their study demonstrated that displacements recorded on the surface are very much influenced by topography, in particular when the incident wavelengths are comparable to the size of the topographic features. Rayleigh waves are generated at the slope toe and slope crest. They also suggested that the amplitude of Rayleigh waves recorded behind the crest can be 35% higher than the amplitude of the incident waves at the free field surface.

Afterwards, the finite-difference method is applied to simulate elastic wave propagation through a 3-D model of the Santa Clara Valley (Frankel and Vidale, 1992). The numerical model (30 (east-west) × 22 (north-south) × 6 (depth) km) corresponded to a large mountain area and was divided into many zones with 4 million grid points. A synthetic motion from a magnitude 4.4 corresponding to the aftershock of the Loma Prieta earthquake was used as input motion. The numerical simulations confirmed topographic amplifications and showed how S waves are converted to surface waves at the edge of the basin. It is observed that Love waves produced at the edge of the basin are the largest arrivals of the transverse waves and Rayleigh waves are produced along the southern margin of the basin. In addition, 2-D simulations were also conducted to analyze the effects of the wave incident angle and impedance on wave conversion at the basin. In another study, Frankel showed that the synthetic seismograms from 3D simulations have a larger amplitude than those derived from a 2D model (Frankel, 1993). Moreover, he simulated the San Andreas Fault to demonstrate how the rupture directivity affects the pattern of maximum ground motions on the surface of the basin. It was concluded that the presence of off-azimuth surface wave arrivals increased the ground motion amplitude in the 3D simulations and these off-azimuth arrivals represent surface waves produced at the edges of the basin.

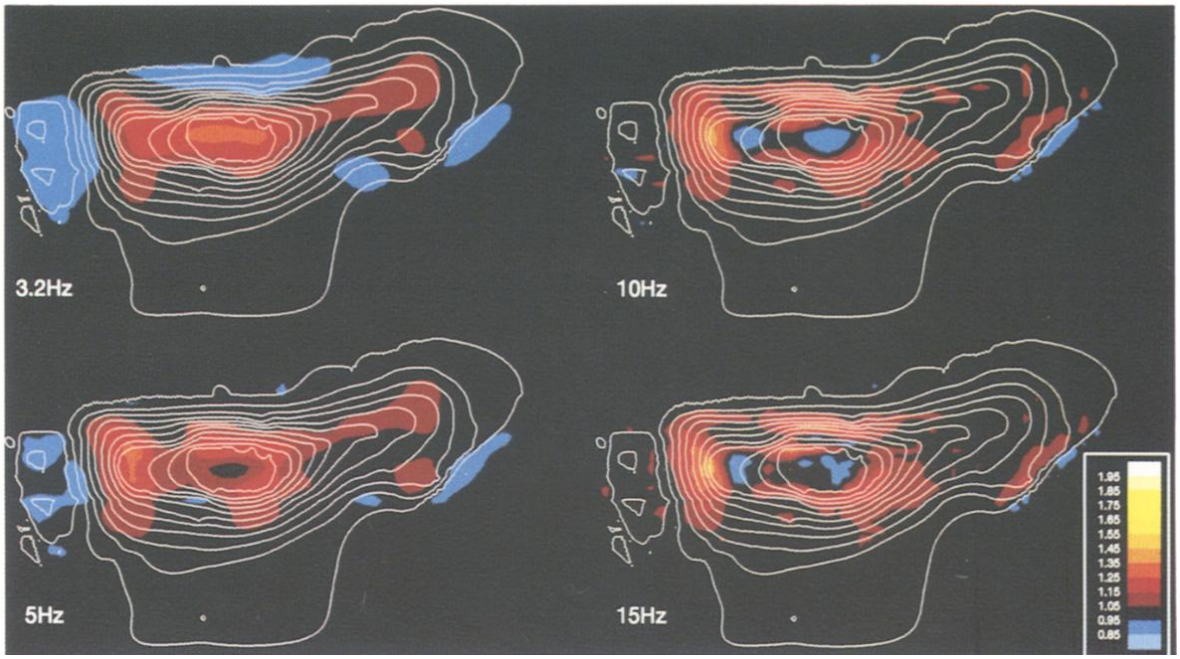


Figure 1.16: Seismic response of the hill model subjected SV waves at different frequencies range. The topographic contour of 5-foot intervals lines are labeled in white (Bouchon and Barker, 1996).

During the 1994 Northridge earthquake, a very high horizontal acceleration peak of 1.58 g was recorded by an analog accelerograph installed at a ridge near the Pacoima Dam, while the peak accelerations recorded by nearby accelerographs at surrounding areas were under 0.5 g (Sep úlveda et al., 2005). In order to understand the high acceleration recording, numerical simulations (Figure 1.16) were carried out (Bouchon and Barker, 1996). The results showed that the ground motions are strongly affected by the topography in the frequency range between 2 and 15 Hz, for which the ground motion is amplified by a ratio of 1.3 to 2 compared to the incident signal. However, numerical prediction underestimated ground motion amplification. A part of amplification is therefore considered coming from the three-dimensional geological structure of the site.

Rayleigh waves are considered as the most important cause of observed ground motion amplifications. They can be generated when compressive waves (P) and shear waves (S) propagate into the media and are diffracted at the free-surface. To accurately describe waves propagation and diffraction, 3D modeling is performed using the discrete wavenumber formulation of indirect boundary integral equation (Durand et al., 1999). The results also show that the maximum ground motion amplification is produced when the geometric size of the topography is comparable to the wavelength of the input motion. The ground motion amplifications calculated from 3D models can reach twice of those computed in 2D models.

Gazetas et al. (2002) reported that the eastern bank of the Kifisos river canyon in Greece experienced heavy damage during the 7 September 1999 M_s 5.9 earthquake. Topography and soil effects were supposed to be the key factors for the ground motion amplifications. Therefore, a parametric study using 2D finite element model and spectral analyses were carried out to evaluate the role of topography and surface geology. The presence of surface soil layer was found to have a significant influence on ground motion amplification whose the maximum value was observed near the

crest. The results suggested that the incident angle controls the amplitude of ground motion amplification because it affects the wave diffraction when vertically propagating SV waves impinge at the surface.

In 1997, Ashford and Sitar conducted a parametric study to investigate the effect of the incidence angle of SH and SV waves on topographic amplifications at a steep slope using generalized consistent transmitting boundaries (Ashford and Sitar, 1997). It is observed that ground motion amplifications were resulting from a combination of waves traveling into the slope and deamplifications occurred when waves were traveling away from the slope. The ground motion amplification can reach a ratio of 2 compared to the input motion. Moreover, the results demonstrated that the presence of surface deposits with low seismic velocities has a much larger influence on ground motion amplification than topography at this site. Later, Ashford et al. performed another parametric study on topographic effects for steep slopes subjected to shear waves with a various angle of incidence (Ashford et al., 1997). The results from numerical simulations indicated that the ground motion amplification can be up two times when the input shear waves are inclined compared to vertical incidence. With decreasing slope angle, the magnitude of the amplification at the first peak decreases from about 25% to about 15%. The amplification factor can be normalized as a function of the ratio of the slope height (H) and the wavelength of the input signal (λ). The peak amplification at the crest of a slope is obtained for a normalized frequency H/λ=0.2 for a slope angle equal to 90 °and a damping ratio equal to 1%.

In 1998, Pitarka et al. simulated the near-fault ground-motion amplification in a kinematic earthquake rupture model using 3D Finite-Difference Method (FDM) and analyzed the effect of basin-edges on the ground motion amplification (Pitarka et al., 1998). In this study, they simulated strong ground motions in a selected region located along the northern edge of the Osaka Basin, which includes the Kobe city area and the fault segments. It can be seen from the results that the coupling of source of the 17 January 1995 Hyogo-ken Nanbu earthquake and basin-edge effects are responsible for the impulsive ground motions with high amplitude and long duration observed in a narrow zone less than 1 km from the basin edge. However, the ground motions depend on the fact that the near-fault ground motion in the basin sediments is very sensitive to the source and the basin edge structure as well.

Frankel and Stephenson (2000) developed a three-dimensional finite difference model to simulate seismic wave propagation for two earthquakes (M_L 4.9 and 3.5). Their results showed the influence of basin edge and surface deposits on the modification of surface waves. Consequently, Wilson and Pavlis introduced a statistical spectral ratio method (median reference method, MRM) to investigate the effect of near-surface geology on ground motion amplifications (Wilson and Pavlis, 2000). Spectral ratios were calculated for all possible couples of stations without considering their locations. Thus, for a given station, a statistically determined amplification factor could be obtained by calculating the median value of all ratios between this station and all the others. Later, this method was used by Poppeliers and Pavlis for assessing topographic effects on the ground shaking in a surface coal mine in Indiana (Poppeliers and Pavlis, 2002). In 2012, by using 3D numerical simulations, Maufroy et al. analyzed site effects on seismic shaking using the MRM and the results were validated using standard spectral ratio method (SSR) (Maufroy et al., 2012). Their results indicated that the amplification factors computed using the SSR are highly dependent on the choice of the reference station. The spectral amplification calculated by the SSR method often over-estimate the amplification computed using the MRM technique. They also showed that the number of reference stations used in the MRM technique has no significant effect on amplification factors. When conducting the study with a randomly located

source, it is found that the amplification factors at different locations are significantly influenced by the location of the source and the direction of wave propagation.

In order to investigate the effect of topographic and structural features on observed concentrated damages near the edge of a canyon during the September 1999 Parnitha (Athens) Earthquake, Gazetas et al (2002) performed 1D and 2D wave propagation analyses using Finite Element method and Spectral Element formulations. The results demonstrated that the topography significantly affected the ground motion in a 50 m wide zone behind the crest of the canyon. Ground motion amplification is also substantially affected by soft soil layers present close to the surface. Ground motion amplifications vary around 1.4 over a broad frequency band including the central frequencies of input motion. Surficial deposits and topographic effect are believed to have played an almost equal role in increasing the intensity of input motion.

In 2001, Sánchez-Sesma et al. proposed an indirect boundary element (IBEM) method technique with a variational criterion in order to reduce the computational time duration at high frequencies using boundary element methods (Sánchez-Sesma et al., 2001). The boundary force density is expanded in terms of a complete set of functions. Weighting functions from the same complete set are used to minimize the error of this approximation. Once a significant subset is selected, the size of the resulting linear system is much smaller than that of the IBEM method as currently applied. Then, Luzon et al. analyzed the ground motion response of different heterogeneous models of sedimentary basins for SH waves using the indirect boundary element method (IBEM) (Luzon et al., 2003). They used approximate analytical expressions for Green's functions to compute displacements for the incidence of SH plane waves in these heterogeneous sedimentary basins. Later, Gil-Zepeda et al. used a hybrid method combining indirect boundary element and discrete wave number to simulate the ground motion in a model of stratified alluvial valleys subjected to incident plane SH waves (Gil-Zepeda et al., 2003). This method is based on the single-layer integral representation for diffracted waves, for which refracted waves can be expressed as a linear superposition of solutions for a set of discrete wave numbers.

Bouckovalas and Papadimitriou presented results of numerical simulations of the seismic response of homogeneous slopes subjected to SV seismic waves (Bouckovalas and Papadimitriou, 2005). The numerical simulations were performed for a series of slope models with variable slope geometry, as well as variable frequency and number of cycles of the input signal. The analyses of their results show that topography induces alternation of amplification and deamplification along the ground surface behind the slope crest. The maximum amplification ratio remains under 1.6. The topographic effect is highly dependent on slope angle and dimensional frequency (ratio between slope height and wavelength of input excitation). In addition, they established a set of approximate relations between topography aggravation factor and dimensionless frequency. Case studies showed that these relations could provide reasonable predictions.

In 2005, another parametric study was conducted to evaluate the effects of local soil conditions on the ground motion at a slope located on the eastern side of the Kifissos river canyon, Greece (Assimaki et al., 2005). The simulations were carried out for a two-layer soil profile overlying bedrock. Results indicate that the obtained amplification could not be explained using the topographic effect alone, and also that the soil profile had much more influenced the calculated ground motions. In addition, the impedance of lateral heterogeneity of the soil plays a significant role in the topographic amplification factor next to the crest. Assimaki and Kausel consequently investigated the contribution of topography,

soil nonlinearity, and soil-structure interactions on amplifications by two-dimensional finite element simulations (Assimaki and Kausel, 2007). Their results suggested that stiff features at the top of ridges may filter high frequencies and soil-structure interactions beneficially affect the topography amplification factors near the crest.

In another work, Assimaki and Jeong performed numerical simulations to assess the influence of topographic amplifications on the damage concentration located at the top of a ridge near the Hotel Montana, Haiti (Assimaki and Jeong, 2013). Assuming elastic homogeneous site conditions, they noticed that the calculated topographic amplifications are not in total agreement with the field observations, both in amplitude and in frequency. However, 1D simulation at hilltop predicts ground motion amplifications with the underestimated amplitude at the same frequencies as the observed ground-motion amplification. Last, they indicated that ground motion amplification is attributed to the fact that soft soil layers of the near-surface traps seismic waves and scattering at the irregular ground surface modify the wave field.

Recently, 3D spectral element mesh was applied in numerical modeling to assess the effect of topography on ground motion modification (Lee et al., 2009). The amplification of ground motion is mainly observed at the crest of hills while the deamplification can be obtained at the bottom of the hills. Strong shaking may occur when high-frequency surface waves travel through small-scale topographic features. In addition, the topography has a significant effect on the propagation of volume and surface waves to surrounding areas and the amplification can reach a ratio of 1.5 compared to the input motion depending on epicenter location and depth. In 2010, Sánchez-Sesma analyzed the seismic response of a three-dimensional rockfill dam model using the Indirect Boundary Element Method (IBEM) (Sánchez-Sesma et al., 2010). The boundaries of the model are discretized into boundary elements whose size related to the shortest wavelength. The preliminary results in the frequency domain show displacement amplitudes for frequencies 0.8, 1.6, 3.2, and 6.4 Hz. A following dynamic analysis using the IBEM was performed by Rodr ́guez-Castellanos et al. to study the amplification of elastic waves in irregular soil profiles (Rodr ́guez-Castellanos et al., 2011). The results demonstrate that condensed mesh adds rigidity to the model and thus the simulations give smaller amplitudes than the reference solutions.

Lenti et al. performed numerical simulations using the finite difference method to analyze the local seismic response in a section of the Nera River alluvial valley in central Italy and they compared the results with those from field observations (Lenti et al., 2009). The calculated amplification was found in agreement with the spectral response from the horizontal-to-horizontal spectral ratios, which demonstrated that ground motion amplification was mainly due to the specific heterogeneities of the valley deposits. Consequently, Lenti and Martino analyzed the interaction of seismic waves with step-like slopes and its influence on the landslide movement (Lenti and Martino, 2012). Parametric analyses in terms of peak ground accelerations, Arias intensities, frequency contents, dip, height and thickness of geological strata were performed using the finite difference method. The results show that the co-seismic x-displacements of the landslides significantly depend on the interaction of seismic waves with slopes. In another study, they carried out an analysis still using the finite difference approach to investigate the influence of the interaction between seismic waves and slopes on seismically induced displacements of existing landslides (Lenti and Martino, 2013). They assessed the relationship between displacements and dimensionless frequencies, the values of the Arias intensity, and the critical accelerations using the regression analysis and then they got conclusions that the

seismic amplification, the coupling of a 2D interaction between seismic waves and slope and the 1D resonance significantly affects the seismically induced displacements.

1.2.2 Influence of the subsurface geology

Surface geology (soil layers) plays an important role in wave propagation near the surface and therefore it causes ground motion amplification or sometimes deamplification (Assimaki and Jeong, 2013). In particular, for the site where topographic reliefs are present, a combination of topographic amplification and soil amplification of ground motion can be observed (Geli et al., 1988). In addition, surficial deposits are often found to have a great influence in ground motion amplification in a certain frequency range depending on the thickness of the soil layer. Field investigations in many earthquakes have shown over the past decades that earthquake damages are more severe over soft surface deposits than on bedrock outcrops (Assimaki and Jeong, 2013; Hough et al., 2010a; Housner and Thiel, 1990). Because most of the buildings are often constructed on sediment deposits that may induce potential influence on the ground shaking, it is worth to take into account the effect of surface deposit when constructing a building. Therefore, numerous instrumental studies, theoretical and numerical investigations on soil layer effect on ground motion amplifications have been carried out to provide a better understanding of this phenomenon. The results confirm that the trapped seismic waves in the surficial layer may cause ground motion amplification because they are reflected and interfered for many times. The interference between these trapped waves will induce amplifications when waves are in resonant patterns, that is to say when the frequency of seismic waves is close to the fundamental frequency of the layer. In the following paragraph, some results from a literature review are illustrating the effect of the surface geology.

Lu et al investigated soil amplification of earthquake ground motion based on the observation records of an array in Chiba, Japan (Lu et al., 1992). It is shown that ground motion amplifications are mostly observed at the top of soft layers and they are similar in three directions. Non-linear response of soil deposits is also observed by analyzing the transfer functions. An "empirical-inferred" amplification method was developed to estimate soil amplification by Atkinson et al. (Atkinson and Cassidy, 2000). The input motions used in this method are derived from the analysis of all regional seismographic data, instead of reference ground motion recorded at bedrock. This method was used at Fraser River Delta, British Columbia in Canada, to assess the effect of deep soft sediments on amplification of ground motions. For weak shaking, the amplification ratio at the Fraser River Delta reaches three to six over a broad frequency range of 0.2 to 4 Hz. When input motion is a signal of high-frequency (f >10 Hz), the ground motion is deamplified. The "empirical-inferred" amplification has larger peaks at specific frequencies, probably due to resonant effects not accounted for in the quarter-wavelength approach.

Based on a number of reliable strong motions recorded during the 1999, 7 September Athens earthquake, Bouckovalas and Kouretzisthe performed a study to assess the effect of the local ground conditions on ground motion amplifications (Bouckovalas and Kouretzis, 2001). They showed that ground motions were substantially amplified due to the presence of stiff soils with the Athens basin and the amplification ratio roughly reaches values which are 40 to 46% higher than those recorded at the bedrocks. It is also found that the seismic excitations were selectively amplified due to soil deposit at a medium-to-high frequency range (3–15 Hz).

The 2010 M 7.0 Haiti earthquake causes widespread damages and ground motion amplifications due to the presence of thick layers of soils are believed to be a key factor in the distribution of damage.

In order to investigate the role of surficial deposit on additional amplifications, seismic stations were deployed by the U.S. Geological Survey to record aftershock ground motions on the top of a hill and at reference site on the foothill ridge adjacent to Hotel Montana. The presence of topographic relief has been used to explain the ground motion amplification, but obviously, it cannot explain severe destructions occurred on site without topographic features. Therefore, D. Assimaki and S. Jeong conducted numerical simulations of 1D and 2D to evaluate ground motion response for a ridge in terms of topographic effect and soil amplification (Assimaki and Jeong, 2013). The study shows that numerical predictions are in agreement with the field observations when the numerical model was created with an appropriate thickness of the soil layer.

1.2.3 Summary

Site effect has been studied by many researchers using field investigations, numerical modeling and theoretical derivations. Instrumental observations provide a reliable evaluation of site effect in a specific site but they face the objective difficulty of intense deployment and monitoring for a long period. Numerical simulation is popular to assess site effects, since it is convenient and low-cost. For simplifying the numerical analyses, advanced constitutive parameters were often abandoned by researchers to reduce the computational work. Moreover, most of these results were obtained based on the analysis of 1D or 2D models. An obvious limitation of such simulation is a model simplification. This is also the reason why the numerical predictions always underestimate the field observation, and it may bias predicted resonance frequencies from the simplified models. 3D numerical models are expected to be more efficient than those of 1D or 2D for studying wave propagation in the near-surface medium and assessing site response. However, it is more expensive to perform 3D numerical analyses than 1D or 2D numerical simulations.

For these studies, almost the same parameters are used in the models created by various techniques. These parameters consist of the geometry of the slope (length, height, and slope angle), a profile of the material (shear velocity, the density of the medium, Poisson's ratio, and Young's modulus) and characteristics of the seismic signal (frequency, duration, and amplitude). In particular, the effects of the presence of subsurface geology on ground motion amplification have been extensively studied and numerous conclusions are reached and confirmed as detailed above. However, the phenomenon of coupling effect of these parameters, e.g. the interaction between topographic amplification and soil amplification, still need to be studied.

1.3 Objectives

The objectives of this research are to contribute to a better understanding of topographic effect and soil amplification, as well as to give clear explanations of differences between observed amplification and numerical results.

The research consists of two routes of investigation. The first phase of the study is intended to evaluate site effect on ground motion amplification using numerical simulations by assessing response characterization of ground motion amplification on the slope ground surface. The second phase of the study is to validate the previous conclusions. For this purpose, we have considered two case studies where field observations or measurements were available. Ground motion amplifications are calculated not only in the time domain but also in the frequency domain using the standard spectral ratio (SSR) method.

This dissertation involves the following aspects:

(1) To perform numerical simulations in order to investigate acceleration amplifications due to topography such as slope (and ridge) in terms of slope angle, slope height as well as coupling with seismic waves.
(2) To perform numerical modeling in order to evaluate the interaction between topographic amplifications and soil amplifications.
(3) To analyze ground motion amplification of a slope in the frequency domain, and validate the results by the comparison with amplification in the time domain.
(4) To carry out back analysis on two case studies where field observations were available in the literature with the objective to compare the results of the numerical simulations with the field measurement, and discuss the potential differences.

1.4 Thesis document structure

Further to this chapter of introduction, the thesis document is divided into 4 chapters.

Chapter 2 mainly focuses on evaluating the effects of topographic parameters on ground motion amplification by analyzing the ground motions provided by numerical simulations along the slope and behind the crest. In this chapter, the interaction between these topographic parameters and seismic wave characteristics are also investigated.

Chapter 3 presents a case study of a ridge in China where accelerations recorded at different points along the slope are analyzed in the time domain and frequency domain. Then, numerical simulations have been performed using the Finite Difference Code FLAC (Itasca) on the same ridge in order to compare the results with the field data.

Chapter 4 concerns the Las Colinas landslide triggered by the Salvador earthquake in 2001 and analyses the possible factors which may have contributed to the trigger of this landslide.

Chapter 5 summarizes the results of the work and gives some possible development and improvement for future works.

Chapter 2 Effects of slope topography on acceleration amplification and interaction between slope topography and seismic input motion

Adapted from Zezhong Zhang, Jean-Alain Fleurisson, Frederic Pellet, 2018. The effects of slope topography on acceleration amplification and interaction between slope topography and seismic input motion, Soil Dynamics and Earthquake Engineering, 113 420-431. DOI: 10.1016/j.soildyn.2018.06.019.

Les effets topographiques sont considérés comme responsables d'une multitude de catastrophes liées aux séismes et ont été invoqués pour expliquer certaines valeurs extrêmes d'accélération enregistrées. Des études de terrain et des études numériques ont été effectuées depuis longtemps pour caractériser la réponse d'un site afin de comprendre l'influence de ses caractéristiques sur les modifications du mouvement du sol. En particulier, la topographie de la pente a attiré l'attention des scientifiques car elle peut aggraver les effets sur les bâtiments situés à proximité du sommet de la pente. Des études paramétriques en termes d'angle de pente, de hauteur de pente, de fréquence du mouvement sismique incident et de son orientation ont été menées. Cependant, la plupart de ces facteurs ont été étudiés de manière indépendante. Par conséquent, une étude plus approfondie de l'amplification due à la topographie de la pente reste toujours nécessaire pour mieux comprendre comment la topographie de la pente affecte le mouvement du sol et comment les différents facteurs interagissent.

Pour évaluer cette amplification topographique, des simulations numériques ont été effectuées avec un modèle de pente élastique linéaire homogène qui a été soumis verticalement à la propagation d'ondes sismiques de type SV. Les analyses numériques ont été réalisées à l'aide d'une ondelette de Gabor avec différentes fréquences et différents nombres de cycles afin d'évaluer l'influence des caractéristiques du mouvement sismique d'entrée. L'étude a porté également sur l'interaction entre la fréquence des ondes sismiques et la taille de la pente. Les résultats ont été analysés et utilisés pour expliquer l'influence de la topographie sur l'accélération enregistrée à la surface du sol le long de la pente, à la fois en termes de facteur d'amplification et d'emplacement où l'amplification maximale est observée.

2.1 Introduction

During earthquakes, local site conditions, including topography (slopes, ridges, and canyons) and geology (sedimentary, basins, and faults), have significant effects on ground motion characteristics and seismic intensity (Assimaki et al., 2005; Geli et al., 1988; Spudich et al., 1996). Site effects can increase or sometimes decrease ground motion acceleration (Fukushima et al., 2000), and thus the presence of a sharp relief can significantly aggravate the disastrous consequences of strong seismic motions (Meunier et al., 2008; Paolucci, 2002). Many field investigations have been conducted after earthquakes and have taken seismic damage related to local site conditions into consideration, such as the 1989 M_w=6.9 Loma Prieta earthquake, the 1999 M_w=7.7 Chi-Chi earthquake, the 2008 M_w=7.9

Wenchuan earthquake, the 2009 M_w=6.3 L'Aquila earthquake in Italy and the 2010 M_w=7.0 Haiti earthquake (Bertrand et al., 2011; Hough et al., 2010b; Tsai and Huang, 2000; Wald et al., 1991; Yin et al., 2009); these earthquakes triggered numerous landslides associated with site effects due to topographic or geological conditions.

The effects of topography have been used by many researchers to explain the large accelerations observed by field accelerographs. For example, during the 1994 Northridge, California, earthquake, a very high horizontal acceleration peak of 1.58 g was recorded by an analog accelerograph installed at a ridge near the Pacoima Dam, while the peak accelerations recorded by accelerographs in the surrounding areas were under 0.5 g (Sepúlveda et al., 2005). A similar observation was made during the destructive Haiti earthquake (Guo et al., 2014). Field observations have qualitatively noted that topographic irregularities led to the modifications of seismic ground motion. However, there is a lack of detailed field recording of ground motion along slopes; therefore, it is difficult to truly quantify the effects of topography on ground motion. Numerical modeling analysis has been widely developed to predict ground motion modifications (Bouchon and Barker, 1996; Geli et al., 1988; Havenith et al., 2003; Tripe et al., 2013). The quantitative prediction of acceleration amplification is difficult because of the complexity of the physical phenomena of wave diffraction associated with a combination of topographic and geological effects. There are also differences between field observations or measurements and numerical predictions. Recorded ground motions are often larger than numerical predictions (Geli et al., 1988; Paolucci, 2002). Such discrepancies have been attributed to many factors (Bard, 1995; Del Gaudio and Wasowski, 2007; Semblat et al., 2002; Semblat and Pecker, 2009) such as the presence of a loose soil layer at the surface, wave-field incident angle and orientation, wave type, and three-dimensional (3D) topography geometry. Another cause of complexity is the location of the monitoring points. Ground motion modification is frequency-dependent and can vary from amplification to de-amplification along the surface of the slope (Boore, 1972); maximum amplification is not necessarily located at the exact crest of the slope but could be at a short distance behind the crest (Bouckovalas and Papadimitriou, 2005; Tripe et al., 2013). Buildings are often located at a distance behind the crest, and thus any acceleration amplification in this region can increase seismic destruction. It is, therefore, necessary to evaluate how the topography affects the acceleration amplification on the ground surface.

Many studies have investigated the influence of topography on acceleration amplification using numerical methods incorporating a slope model with sharp corners (Lenti and Martino, 2012; Tripe et al., 2013). However, natural slopes often have smooth edges resulting from weathering and water erosion. Rayleigh waves, inducing ground motion amplification, are generated due to wave diffraction around slope corners (Jafarzadeh et al., 2015; Ohtsuki and Harumi, 1983), and it is therefore imperative that we get a better understanding of the effect of slope corner curvature on seismic motion modification, since this could be one of the reasons for the differences between observational data and numerical results.

This paper will focus on characterizing acceleration modification along a slope under seismic loading and evaluating the effects of topography, signal frequency and slope edge curvature on acceleration amplification. First, results from numerical simulations will be presented in order to show typical characteristics of acceleration on the ground surface. Then, effects of the slope angle, slope height and curvature of the slope edge will be assessed through a comparison of the acceleration amplifications for different model configurations. Finally, a comparison of the amplification modifications on the ground surface for different frequencies and different numbers of cycles will be

provided to demonstrate the influence of the seismic input motion. For this step, the analyses are based on slopes with different geometrical configurations in terms of slope angle and slope height to investigate the interaction between slope and seismic waves.

2.2 Numerical models

To characterize amplifications of the acceleration on the ground surface along the slope and behind the crest, a series of numerical simulations were performed using the Finite Difference code FLAC8.0 developed by Itasca (Itasca, 2016). Calculation of the distribution of the acceleration along the slope surface was achieved using a linear elastic soil model a density of ρ=2000 kg/m^3, Young's modulus of E=500 MPa, Poisson's ratio of ν=0.3, and Shear wave velocity V_s=310 m/s. The typical slope model geometry used in the numerical analysis is shown in Figure 2.1.

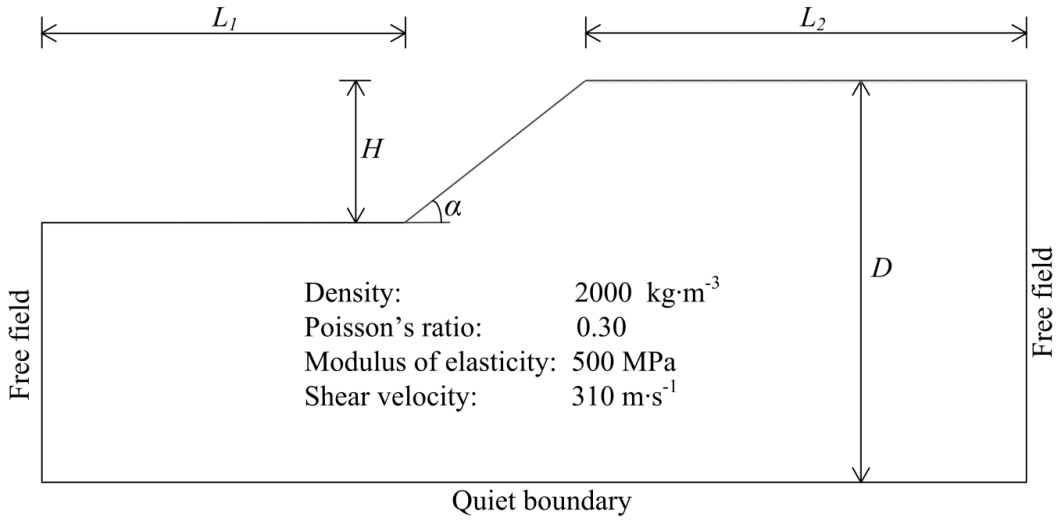


Figure 2.1: Geometry of the numerical model for L_1=200 m and L_2=500 m, D-H=150m.

The seismic input motion is a Gabor wavelet (Figure 2.2) with a peak ground acceleration (PGA) of 0.5 m s^{-2}, which is applied at the base of the slope model as a vertical SV wave. To study the effect of the frequency of the input signal on the acceleration amplification, the wavelet frequency was varied in the range 1 to 10 Hz. Acceleration time history is given by Equation 1.

$$a(t) = \sqrt{\alpha e^{-\beta t} t^{\gamma}} \sin\,(2f\pi t), \tag{1}$$

where f is the central frequency of the signal, t is time, α, β and γ are parameters controlling the shape of the acceleration time history. Corresponding details are listed in Table 2.1.

Table 2.1: Parameters controlling the shape of acceleration history

cycles	1	2	4	6	12
α	2,800,000	63,000	3,100	200	6.5
β	35	22	12	7	3.5
γ	5.7	5	5	5	5

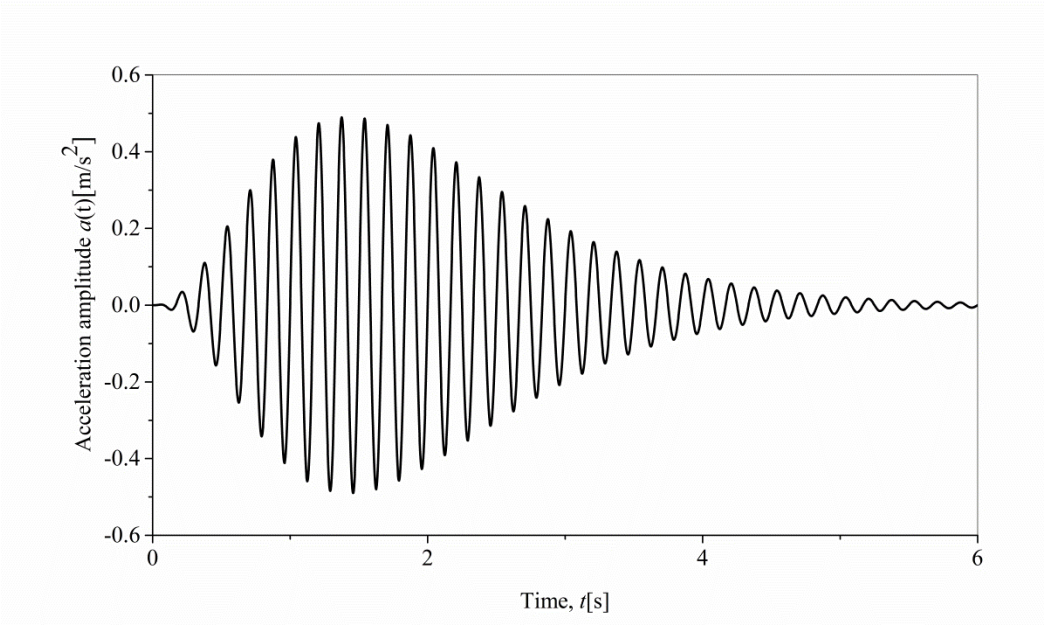


Figure 2.2: Acceleration time history for the Gabor wavelet for the central frequency f=6 Hz.

In the numerical model, quiet boundaries and free field boundaries (Figure 2.1) are used in order to absorb waves approaching the boundary, thus preventing any wave reflection into the model. The solutions of quiet boundaries were proposed by Lysmer and Kuhlemeyer (Lysmer, 1969), who set normal and tangential dampers to the base of the model to absorb the incident wave so that it cannot return inside the model. This is an effective way to simulate a half-space boundary. Free field boundaries have the same purpose and employ dampers coupled with grids of the lateral vertical boundaries of the model in order to simulate the conditions of a half-space. The accuracy of the numerical analysis using absorbing boundaries has been verified and is in good agreement with analytical predictions (Bouckovalas and Papadimitriou, 2005).

Rayleigh damping is applied to compute the energy dissipation. The damping equation is given as a matrix (Itasca, 2016), which comprises components of the mass (M) and the stiffness (K) matrices:

$$C=\alpha M+ \beta K, \tag{2}$$

where α is the proportional constant of the mass matrix and β the proportional constant of the stiffness matrix. The equation will reach minimum damping at the following:

$$\xi_{min}=(\alpha\beta)^{1/2}, \text{ and} \tag{3}$$

$$\omega_{min}=(\alpha/\beta)^{1/2} \tag{4}$$

Although the viscous elements applied in Rayleigh damping are frequency dependent, the independent frequency response can be considered over a limited frequency range by selecting the appropriate parameters of damping ratio and central frequency. In the current study, a damping ratio of 5% was set for the whole model. The frequency of the seismic input motion is selected as the central frequency.

Usually, the observation points located at the free field boundaries on the left or right side of the model are used as reference points (Lenti and Martino, 2012; Tripe et al., 2013) to calculate the topographic amplification. However, the accelerations for the two reference points are different because of the difference in the thickness of the material between the reference point and the model base. Therefore, in the present study, the amplification factor was computed as the ratio between the

absolute value of the peak horizontal ground motion obtained at a given point of the 2D model and the peak horizontal acceleration observed on the ground surface of a corresponding 1D model. The 1D model was built with the same material and the same depth from the observation point to the base of the corresponding 2D model. Using the same loading and boundary conditions as the corresponding 2D model, the acceleration time history obtained on the ground surface of the 1D model subjected to the dynamic analysis was used as reference acceleration.

2.3 Topographic effects on acceleration

2.3.1 Analysis of typical results

The acceleration time histories using the numerical analyses were recorded on the ground surface at different observation points. The acceleration amplification factors along the ground surface were calculated by being normalized with the acceleration at corresponding reference sites. The typical results of acceleration amplification on the ground surface of the model are presented in Figure 2.3 and 2.4 for incident SV waves with a central frequency f=6 Hz.

The distribution of the amplification factor along the slope surface for a slope angle of 20 ° is given in Figure 2.3. The acceleration amplification factors vary around 1, which shows that acceleration along the surface of the slope alternates between amplification and de-amplification. The curve presents several peaks; the highest peak, i.g., the largest amplification factor, is located at the crest of the slope. Behind the crest, several peaks can be observed and their amplitude progressively decreases towards 1 when the observation point is far from the crest. The distance between two successive peaks is constant and equal to 47 m, which is comparable with the wavelength λ=52 m.

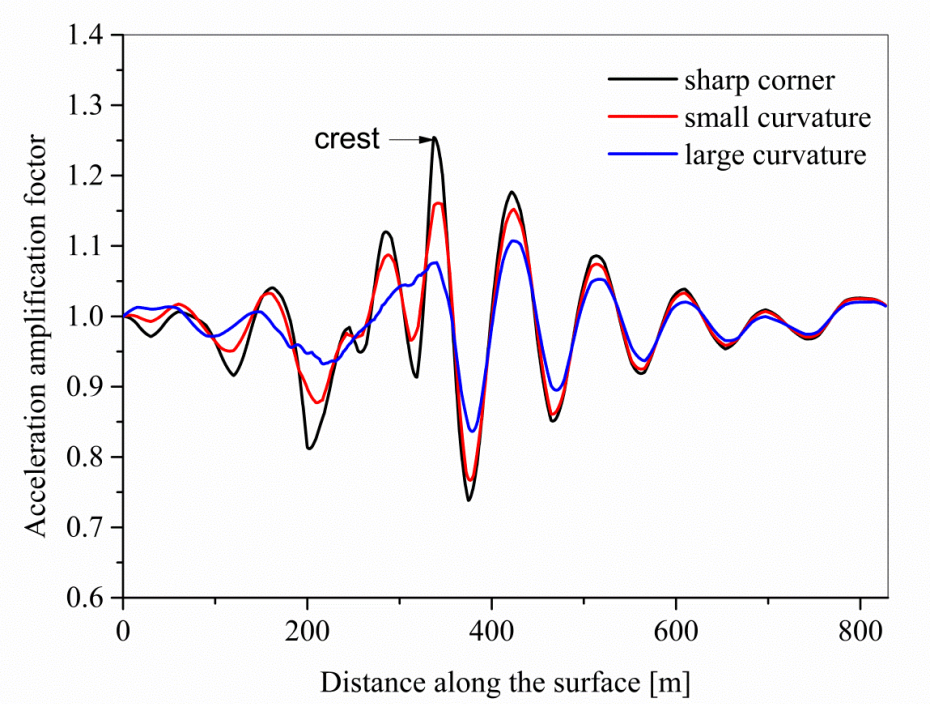


Figure 2.3: Acceleration amplification factor along the surface, for slope angle α=20 ° and slope height h=50 m subjected to a seismic wave with central frequency f=6 Hz. Three lines with different color represent amplification factors of slopes with sharp corners and round corners.

Figure 2.4 shows the distribution of the amplification factor in the case of a slope angle of α=45 °. The curve is less regular than in the previous one, and presents secondary peaks (enclosed in the green square frame). The maximum acceleration amplification corresponding to the highest peak is obtained at a distance of 32.5 m behind the crest.

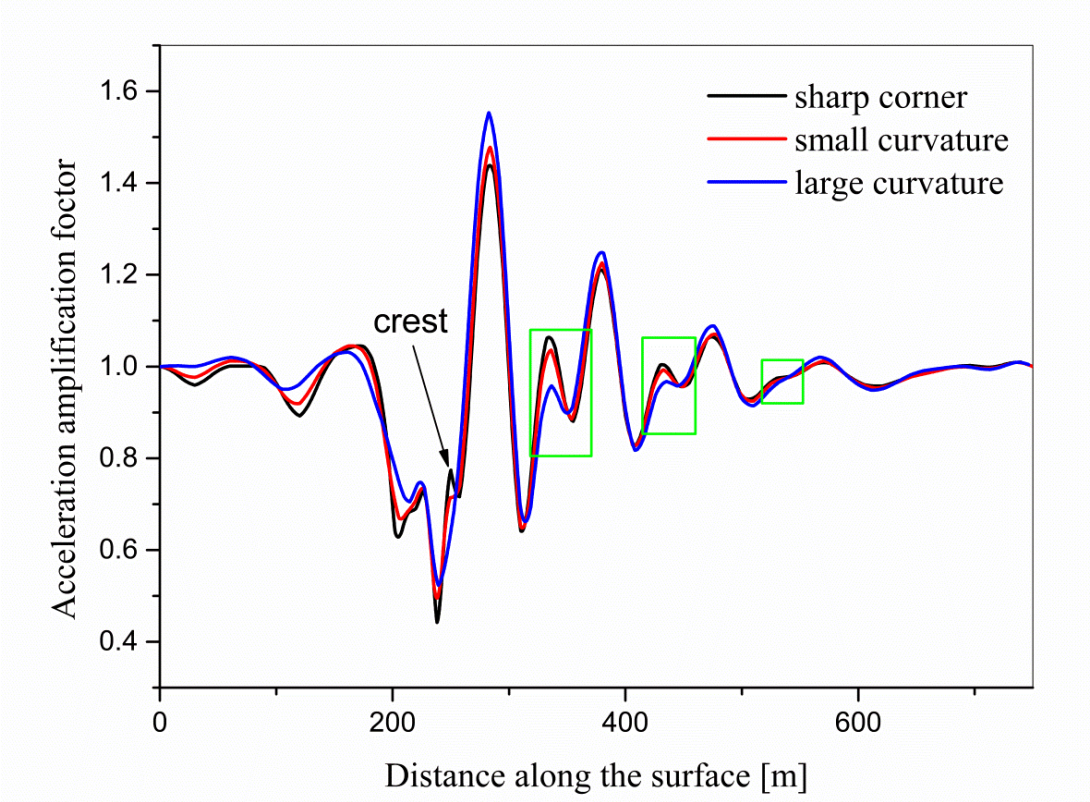


Figure 2.4: Acceleration amplification factor along the surface, for slope angle α=45 ° and slope height h=50 m subjected to a seismic wave with central frequency f=6 Hz. Three lines with different color represent amplification factors of slopes with sharp corners and round corners. The green frame encloses the secondary peak.

Comparisons of acceleration amplification factors along the ground surface of slopes with different edge curvatures quantified by the curvature radii for each configuration (Table 2.2) are also given in Figures 2.3 and 2.4. The curves of the amplification factors have similar trends, for which the peaks and valleys are observed at the same position. At the crest, the peak acceleration amplification significantly decreases with an increase in the corner curvature for a slope angle α=20 °. The acceleration amplification factor at the crest of the slope with a sharp edge reaches 1.25, while it is 1.08 for the slope with a smoother slope edge.

Table 2.2: Curvature radii for the models

Slope angle/ °	10	15	20	25	30	35	40	45
	0	0	0	0	0	0	0	0
Curvature radius/m	200	170	100	90	75	60	50	25
	400	340	200	180	150	120	100	50

The above results can be attributed to the physical phenomena of wave propagation, reflection and diffraction. When incident SV waves impinge on the free surface, reflected SV waves and P waves are generated, resulting from the coupling effects between P waves and SV waves caused by the displacement and traction continuity conditions on the free surface (Achenbach, 2012). As can be seen in Figure 2.5, $\theta_0(=\alpha)$ is the incident angle for the SV wave. θ_1 and θ_2 are reflection angles for the SV and P-waves, respectively. To meet the boundary displacement and stress conditions at the free surface, a simple relationship can be derived based on Snell's law as follows (Achenbach, 2012):

$$\sin\theta_0 = k^{-1}\sin\theta_2, \text{ and} \tag{5}$$

$$\theta_0 = \theta_1, \tag{6}$$

where k is the material constant, defined by the ratio between the P wave velocity and SV wave velocity:

$$k = \frac{V_p}{V_s} = \left[\frac{2(1-\nu)}{1-2\nu}\right]^{\frac{1}{2}}, \tag{7}$$

where ν is Poisson's ratio. When ν=0.3, k=1.87.

In the current study, numerical analyses were performed for a slope angle $\alpha \leq 45°$, and the reflection angle of SV waves is $\theta_1 \leq 45°$. The reflected SV waves at the oblique surface cannot reach the upper surface. When the reflection angle of P waves $\theta_2 > 90° - \theta_0$, the reflected P waves will reach the upper surface. For $\theta_2 = 90° - \theta_0$, a slope angle of 22.2 ° can be calculated using Equation 5. For $\theta_2 \geq 90°$, the reflected P waves travel along the oblique surface, and the critical slope angle is 32.3 ° for θ_2=90 °. For 22.2 °<α<32.3 °, the reflected P waves can directly reach the upper surface and superimpose on the incoming SV waves and the generated Rayleigh waves near the crest. The amplitude of reflected P waves is determined by the slope angle of 22.2 °<α<32.3 °, which is given by Equation 8 (Achenbach, 2012):

$$A_1 = -A_0 \frac{k\sin 4\alpha}{\sin 2\theta_1 \sin 2\alpha + k^2 \cos^2 2\alpha}, \tag{8}$$

where A_0 is the amplitude of the incident SV wave.

By substituting (5), (6) and (7) into (8), A_1/A_0 is obtained as a function of the slope angle, which is plotted in Figure 2.6. The amplitude of reflected P waves increases with the slope angle when the slope angle is less than 32.3 °. As long as the slope angle remains above 32.3 °, the amplitudes of reflected P waves approach zero. This is because when the slope angle is greater than 32.3 °, the reflected P waves transform into surface waves propagating along the free surface.

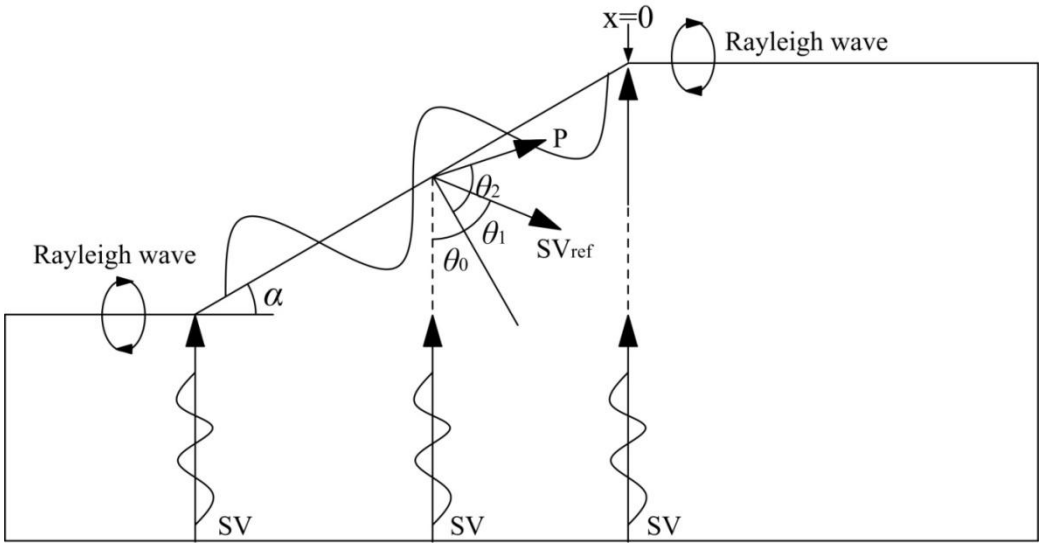


Figure 2.5: Propagation of incident SV waves, reflected SV waves and P waves and diffracted Rayleigh waves in the slope model.

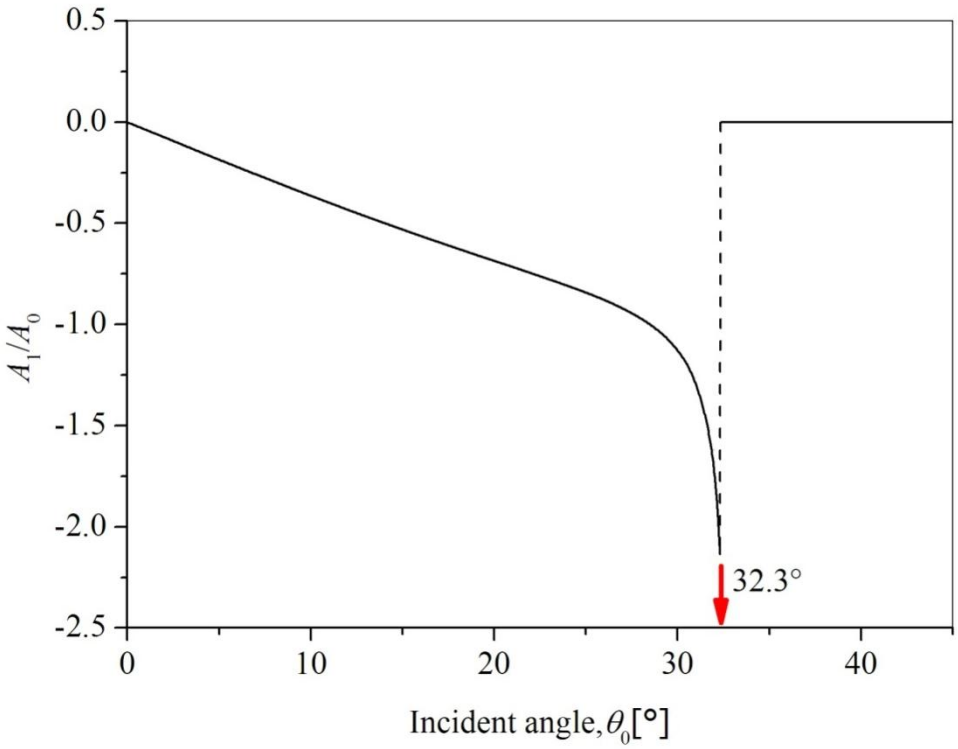


Figure 2.6: Amplitude ratio of a reflected P wave as a function of the incident angle. The red arrow points to the critical angle 32.3 °.

In addition, Rayleigh waves are strongly produced at the slope toe and slope crest due to wave diffraction; these propagate in a "flattened" elliptical particle motion along the ground surface (Asten, 2004; Jafarzadeh et al., 2015; Ohtsuki and Harumi, 1983). According to Boore et al. (Boore et al., 1981), the amplitudes of generated Rayleigh waves could be 0.4 times as much as those of the incident waves and vary with changing angles of the wedge corner.

According to the above theoretical derivation, when the incident angle θ_0 is lower than 22.2 °, the reflected P waves and SV waves propagate downwards and thus the acceleration amplification on the upper ground surface is caused only by generated Rayleigh waves. Therefore, acceleration

amplification can be simplified to the phenomenon of superposition of two encountering waves. Let us suppose two waves with the same wavelength are given by Equation 9 and 10.

$$y_1 = A_1 \cos(\omega t + \phi_1 - 2\pi r_1/\lambda), \text{ and} \tag{9}$$

$$y_2 = A_2 \cos(\omega t + \phi_2 - 2\pi r_2/\lambda), \tag{10}$$

where A_1 and A_2 are the maximum amplitudes, ω is the angular frequency, ϕ_1 and ϕ_2 are the initial phase angles, r_1 and r_2 are the path lengths and λ is the wavelength. Then, using the rule of vector superposition, the superposed amplitude A given by Equation 11 can be obtained.

$$A = \sqrt{A_1^2 + A_2^2 + 2A_1A_2 \cos[\phi_2 - \phi_1 - 2\pi(r_2 - r_1)/\lambda]} \tag{11}$$

According to Equation 11, the largest constructive interference is generated for a phase difference $\Delta\phi = \phi_2 - \phi_1 - 2\pi(r_2 - r_1)/\lambda = 2k\pi$, while the largest destructive interference is generated for $\Delta\phi = \phi_2 - \phi_1 - 2\pi(r_2 - r_1)/\lambda = (2k+1)\pi$. Considering that Rayleigh waves are produced near the crest, the path difference between the generated Rayleigh waves and the incoming SV waves for each point on the upper surface is controlled by the distance between the observation points and the crest. Thus, when the distance to the crest increases, more phase differences between the generated Rayleigh waves and the incoming SV waves are produced. This is the reason why the acceleration amplification factors vary around 1 and the distances between the neighboring peaks (constructive interference) and valleys (destructive interference) of the curve of the acceleration amplification factor remain the same. This distance should be equal to the wavelength of the Rayleigh wave. Similarly, for an incident angle θ_0>32.3 °, the reflected P waves travel to the upper surface and are involved in superposition with Rayleigh waves and SV waves. Therefore, secondary peaks of the curve of the acceleration amplification factor are produced due to the complex phenomenon of wave superposition in terms of three different waves at the same frequency.

2.3.2 Effects of the slope angle

To evaluate the effects of the slope angle on the acceleration amplification on the ground surface of slopes, 8 slope configurations with a slope angle varying from 10 ° to 45 ° were modeled and subjected to numerical simulation. The acceleration time history on the ground surface was recorded and amplification factors were calculated by being normalized by reference acceleration. Figure 2.7 gives a comparison of acceleration amplification factor along the ground surface behind the crest of slopes with different slope angles. It can be seen that amplification factors fluctuate around 1 and significant differences in amplitude appear with variations of the slope angle. The maximum ratios range between 1.08 and 1.54 in terms of the slope angle varying from 10 ° to 45 °. For slope angles lower than 30 °(exactly 32.3 °) the maximum amplification factor steadily increases with the increasing slope angle, while it decreases when the slope angles are greater than 35 °. This observation agrees with previous theoretical analyses: the amplitude of the reflected P waves strongly increases with the slope angle for slope angles lower than 32.3 ° and they reach the largest amplitude for slope angle of 32.3 °. Additionally, the reflected P waves transform into surface waves and propagate along the ground surface as long as the slope angle remains above 32.3 °.

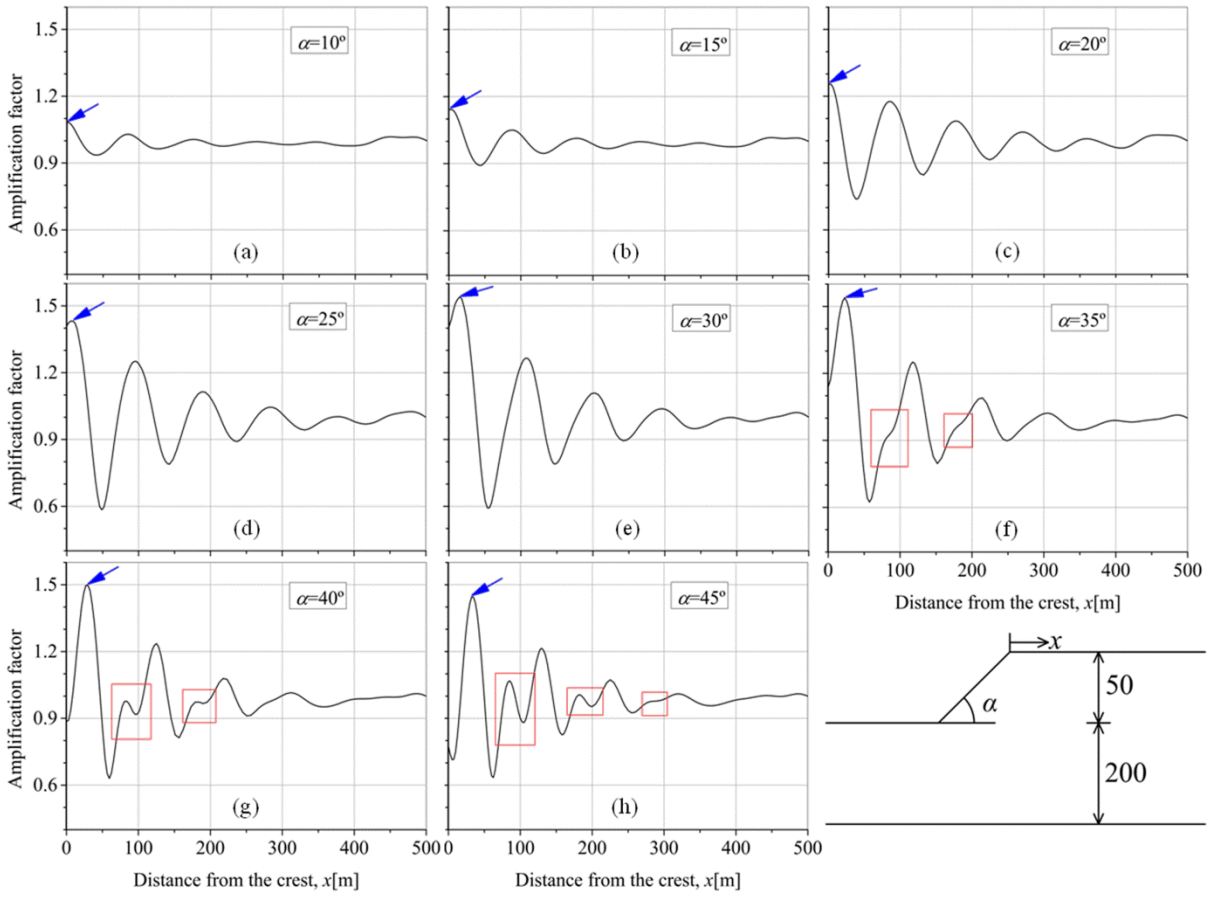


Figure 2.7: The maximum amplification factor as a function of distance from the crest. (a)-(h) Results from numerical analyses of the slope model with varying slope angles ranging from 10 ° to 45 ° in case of slope height h=50 m. The blue arrows point to the maximum acceleration amplification and the red frame encloses the secondary peak.

When the slope angle is less than 20 °, the acceleration amplification factors remain under 1.3, and the maximum amplification factors are obtained at the crest (the blue arrow points to the maximum amplification in Figure 2.7). Although it is often reported that the maximum acceleration amplification is obtained at the crest (Ashford and Sitar, 1997; Tripe et al., 2013), it appears that this is not always the case. In the current study, the maximum acceleration amplification was produced at a short distance behind the crest and depended on slope angle. It was also found that this distance increases with slope angle when the slope angle is greater than 20 °. For instance, for slope angles equal to 25 ° and 45 °, the maximum acceleration amplifications were obtained at 5.7 m and 33 m behind the crest, respectively. Secondary peaks of the amplification factor curve were observed when the slope angles were greater than 32.3 ° (as shown in the red square frame). This is because the reflected P waves transform into the surface wave and involve in the complex wave superposition on the ground surface. The same phenomena can be found in three-slit interference experiments (De Raedt et al., 2012).

Figure 2.8 shows the distance between the location of the maximum amplification and the slope crest as a function of the slope angle. It can be seen that for slope angles lower than 20 ° (exactly 22.2 °), the maximum amplification was obtained at the crest, while the maximum acceleration amplification was observed on the ground surface behind the crest when the slope angles were greater than 22.2 °. In such a situation, because P waves can propagate to the ground surface, the highest value of acceleration amplification does not necessarily occur at the crest due to the phase difference in the waves involved in superposition.

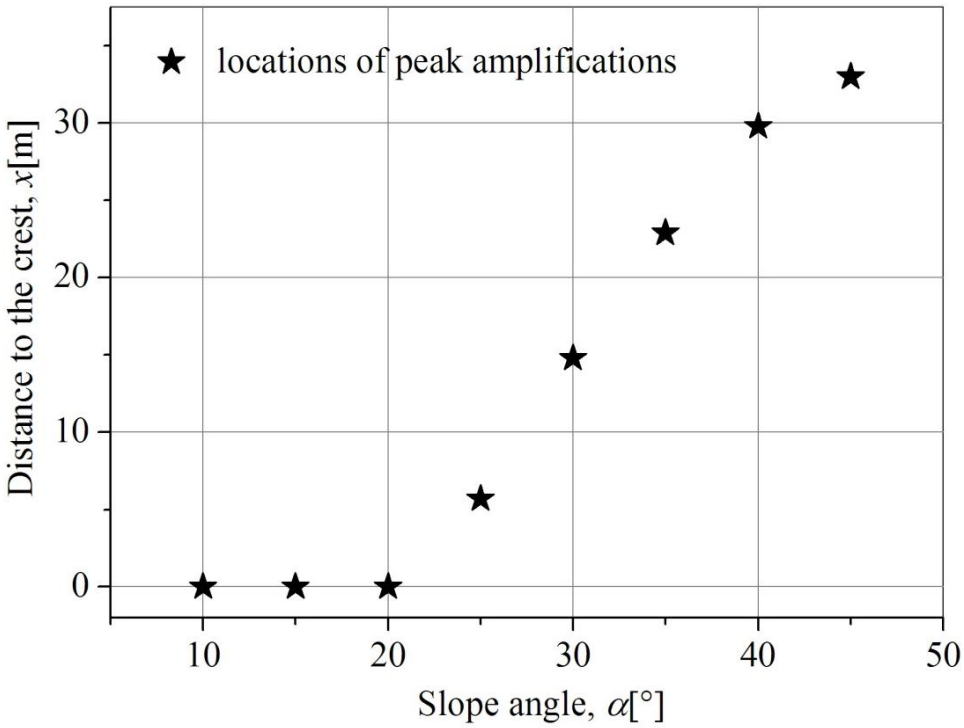


Figure 2.8: Location of the maximum amplification as a function of the slope angle. For slope angle α>22.2 °, the maximum amplification is observed at a short distance behind the crest.

2.3.3 Effects of the slope height

The effects of slope height were evaluated for slope models with different slope heights. In order to separate the effects of slope height from the amplification caused by varying slope angles, we configured two groups of models with a slope angle of either 25 ° or 45 °. The results are shown in Figure 2.9 and Figure 2.10. It can be seen that the acceleration amplifications are significant and affected by the varying slope heights. For each group of the results, the curves of the acceleration amplification factor are similar in shape.

Figure 2.9 presents results of amplification factors along the upper ground surface for a slope angle α=45 °. Generally, the maximum amplification factor is higher for slopes greater than 50 m. The maximum amplification factor of 1.58 is observed at 33.3 m behind the crest for a slope height of 90 m. The maximum amplification factor increases sharply with the slope height when the slope height is less than 50 m, while it gently increases as long as the slope height is comparable to or larger than the wavelength. The assumed SV velocity of 310 m/s was used for the soil material in the slope model subjected to input motion with a 6 Hz central frequency. Thus, the wavelength is about 52 m. Due to a large difference between the wavelength and slope height (e.g. h=20 m), there is not much wave diffractions which is mainly responsible for the topographic amplification. Therefore, as the slope height increases from 20 to 50 m, the amplification factor increases by 0.29, while the increment is only 0.06 for slopes rising from 60 m to 90 m.

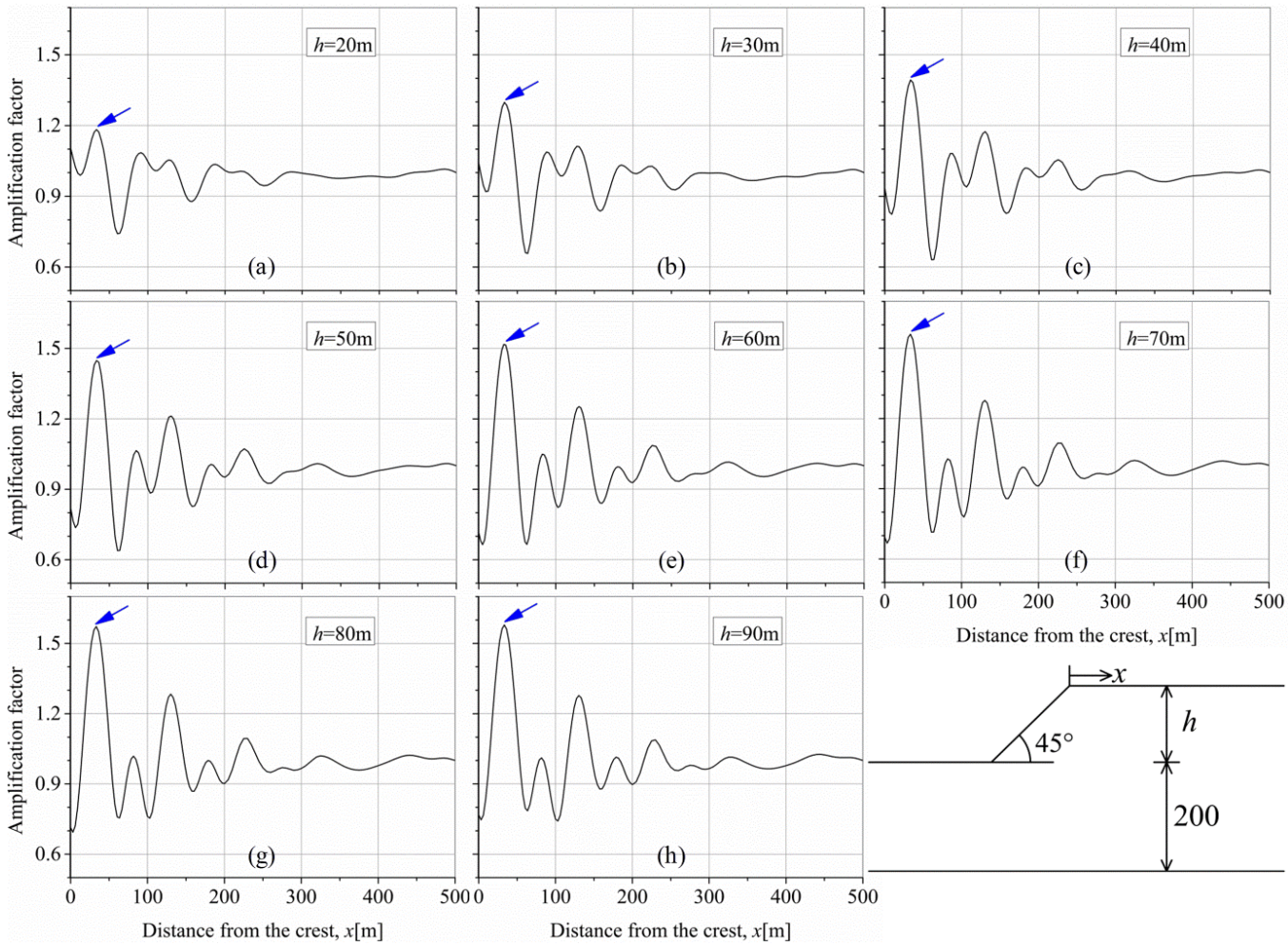


Figure 2.9: Acceleration amplification factor as a function of distance from the crest in case of slope angle α=45 °. (a)-(h) Results from numerical analyses of the slope model with varying slope height ranging from 20 to 90 m. The blue arrows point to the maximum acceleration amplification.

Amplification factors along the upper ground surface of the slope with a slope angle α=25 ° are plotted in Figure 2.10, which generally shows slightly lower peak amplifications compared to those for α=45 °. The difference is due to the fact that no secondary peak is observed for the amplification factor curves as the reflected P waves cannot be transformed to surface wave for a slope angle α=25 °. The maximum amplification is obtained for h=70 m. The ratio between the slope height and the wavelength can significantly affect not only the amplification amplitude but also the location where the largest amplification is observed. Namely, when the wavelength is smaller than the slope height, this location remains fixed for varying slope heights, e.g. h=70, 80, 90 m. However, for a wavelength lower than the slope height, the wave field can be modified due to wave scattering. Therefore, the location where the largest amplification is observed moves closer to the crest with increasing slope height, e.g. h=20, 30, 40, 50, 60 m.

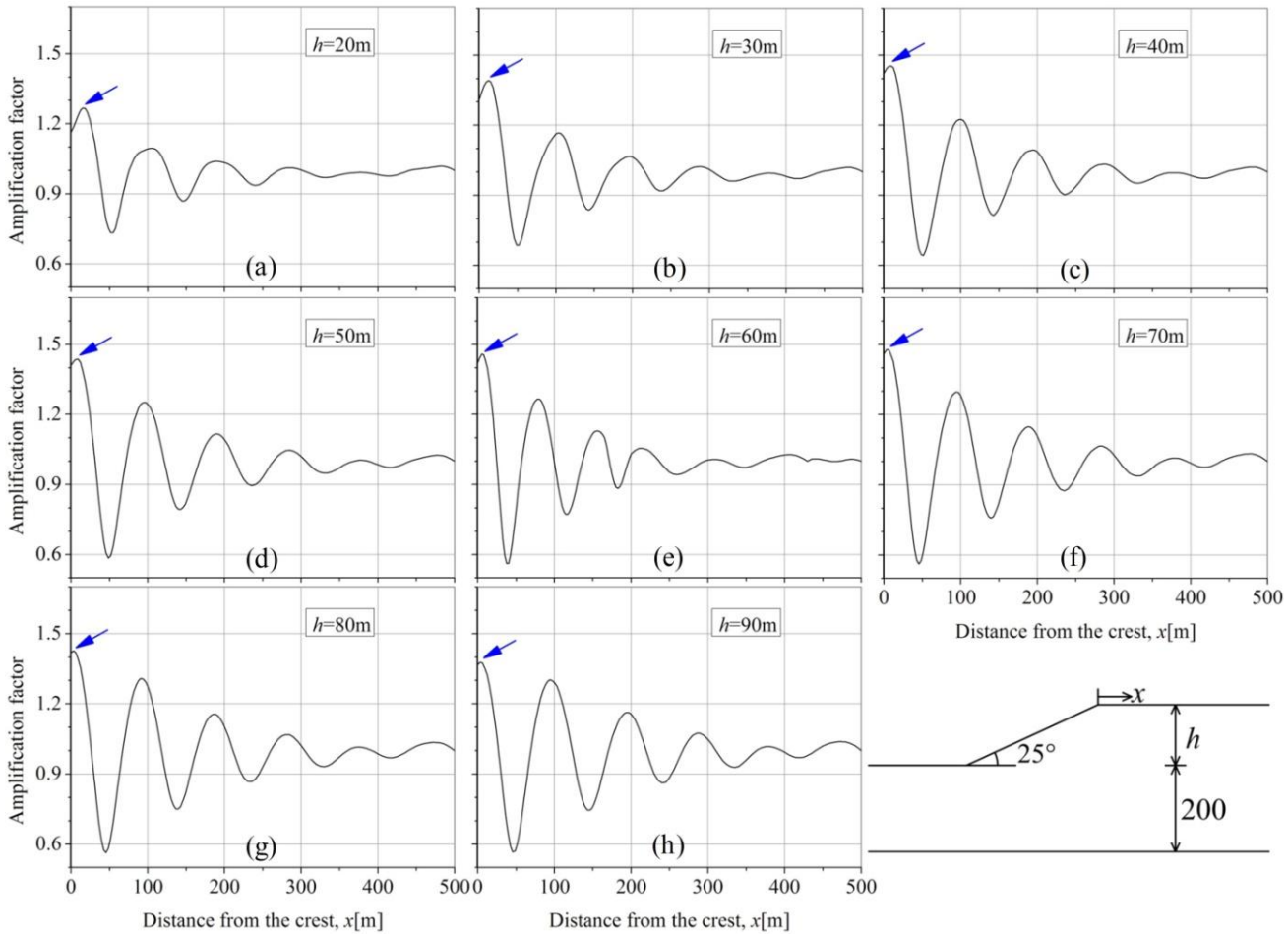


Figure 2.10: Acceleration amplification factor as a function of distance from the crest in case of slope angle α=25°. (a)-(h) Results from numerical analyses of the slope model with varying slope height ranging from 20 to 90 m. The blue arrows point to the maximum acceleration amplification.

2.3.4 Effects of curvature of the slope edge

Slope models with different curvatures of the slope edge were analysed to evaluate the effect of slope edge curvature on the acceleration amplification. Note that the curvatures of the slope edge are quantified by the curvature radii for each configuration (Table 2). The results presented in Figure 2.11 show substantial differences in the acceleration amplification factors along the ground surface of the slope, due to the variation of the slope edge curvature. For slope angles of 25°, the difference in amplification factor between slopes with sharp corners and those with large edge curvatures reaches 0.22. The acceleration amplification factors for slopes with sharp corners are larger than those with smooth corners when the slope angle is less than 30° (exactly 32.3°); this difference can reach 18%. When the slope angle is close to the critical angle of 32.3°, the amplification factor may increase or decrease with increasing corner curvatures depending on the corner curvature ratio. The reason is that a small curvature correspondingly varies the slope angle close to the critical angle of 32.3° when the slope angle is slightly greater or less than 32.3°, while the slope angle becomes much smaller or larger than 32.3° when there is a large corner curvature.

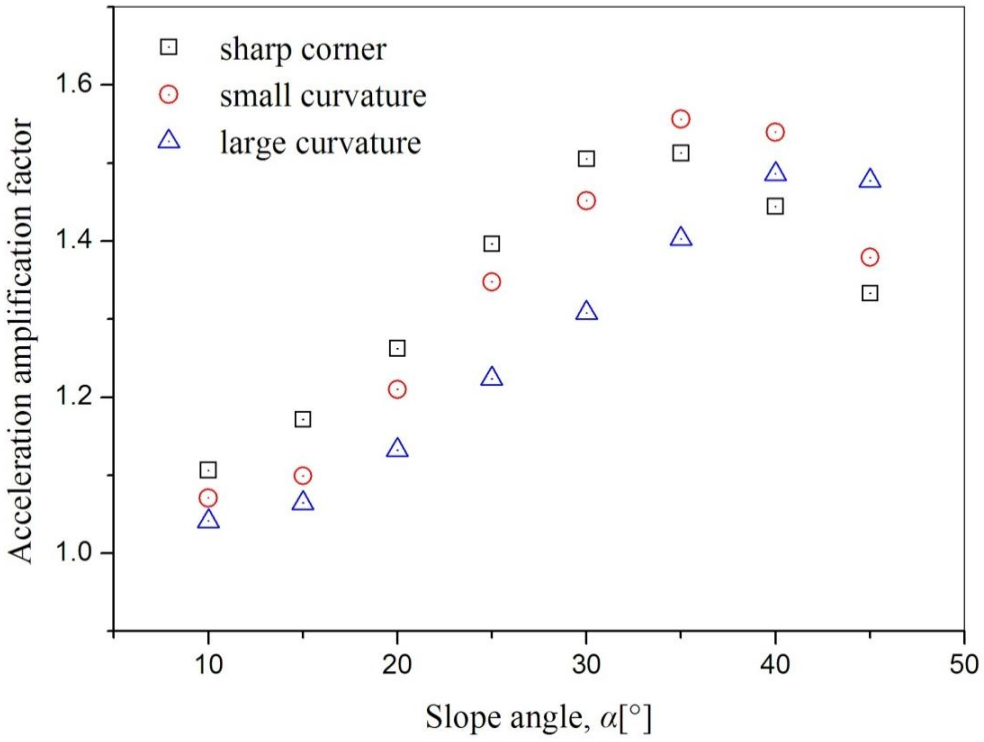


Figure 2.11: Amplification factor as a function of slope angle. Squares represent results of a slope with the sharp corner; cycles represent results of a slope with corners of small curvature; triangles represent results of slopes with corners of large curvature.

To characterize the acceleration amplification on the upper surface of slopes with different curvatures of the slope edge, a series of models investigated variations in the edge curvature of the slope model subjected to a seismic input motion with the central frequency of 6 Hz. The first model has a slope angle of 20 °and slope height of 50 m, with the other geometrical parameters as shown in Figure 2.1. The other models were created by varying the edge curvature of the first model, e.g., the second model has a curvature radius of 200 m for the upper slope corner, while another model has the same curvature radius for the lower slope corner, and the last model has two slope corners with curvature radii of 200 m. Figure 2.12 compares the acceleration amplifications along the ground surface for slopes with different slope corner curvatures. It can be seen that the amplification factor is significantly affected by the curvature ratio, particularly in the vicinity of the slope. The upper edge and lower edge of the slope are responsible for acceleration amplifications at different locations. Namely, the difference in the amplification factor near the slope toe is mainly caused by the variation of the lower corner curvature, while the difference near the crest is primarily attributed to the change of the upper corner curvature.

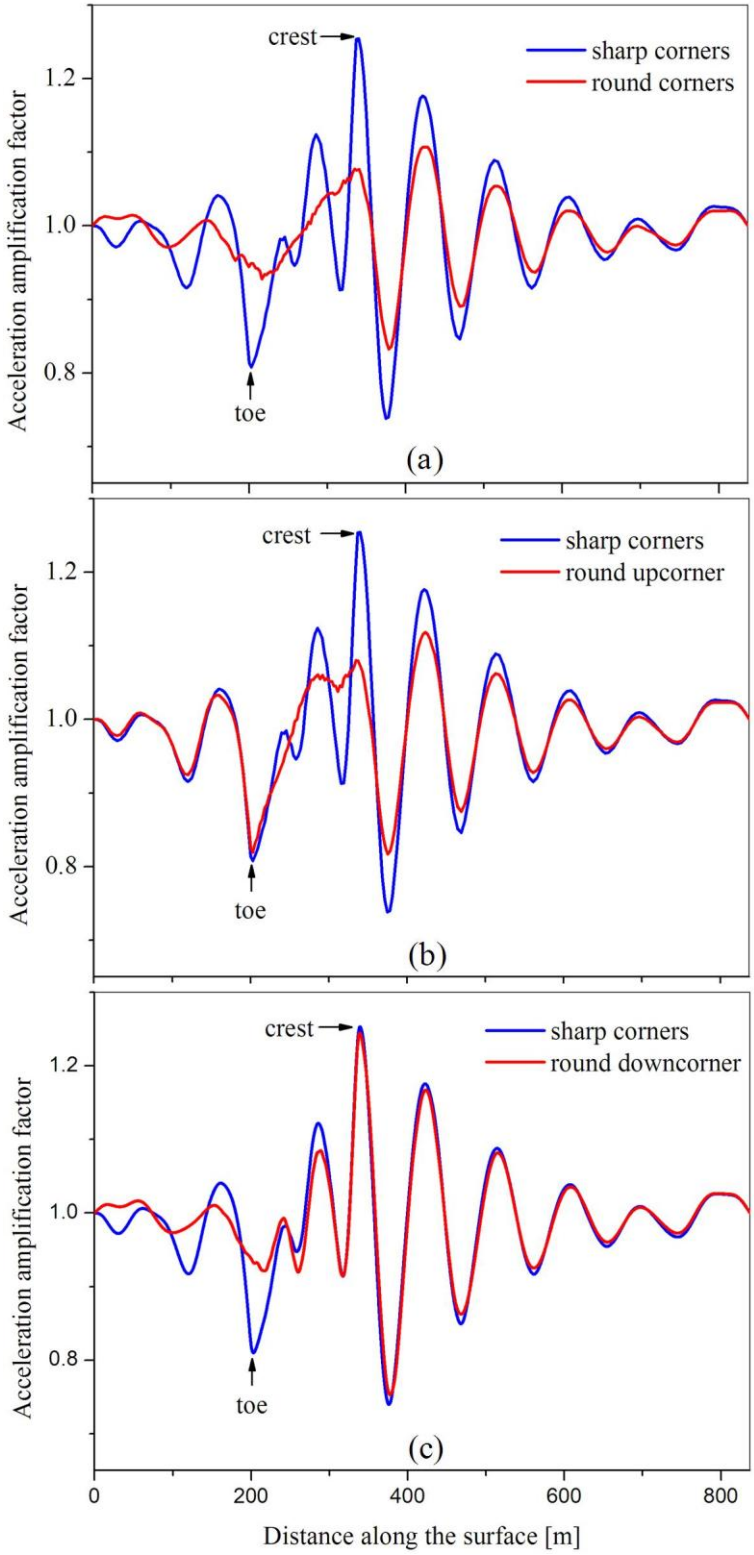


Figure 2.12: Amplification factor on the ground surface for slope with sharper corners and slope with round corners (a), the upper round corner and the lower sharp corner (b) and the upper shape corner and the lower round corner (c), for slope angle α=20 ° and slope height h=50 m, subjected to a seismic wave with central frequency f=6 Hz.

2.4 Influence of seismic input motion

The topographic effect has been reported to be very significant when the input motion wavelength is comparable with the geometric size of the irregularity, while it can be negligible for excitation in very low frequency (Ashford and Sitar, 1997; Ohtsuki and Harumi, 1983), i.e., relatively long wavelengths compared to the topographic relief size. For studies on the topographic effect of the slope, ridge or canyon, it is accepted that the ground motion amplification is primarily caused by diffraction of incident waves at the slope, depending on the ratio between the wavelength of the input motion and the size of topographic relief. It is, therefore, necessary to investigate the influence of the seismic input motion on acceleration amplification. Two groups of models were investigated with varying model geometries and subjected to seismic input motion with varying central frequencies from 1 Hz to 10 Hz. In the first group of models, the slope angle varies from 10 ° to 45 ° with an interval of 5 °; the other geometrical parameters are shown in Figure 2.1. In the second group of models, the slope height varies from 20 to 90 m while the slope angle remains at 45 °. In addition, a slope model with a slope angle α=45 ° and slope height h=50 m was subjected to numerical simulation to evaluate the effect of the number of cycles of seismic input motion.

2.4.1 Effects of signal frequency

Comparisons of maximum amplification factors on the upper ground surface as a function of slope angles for different central frequencies of input motion are given in Figure 2.13. A substantial difference in the acceleration amplification is observed due to the variation of the input motion frequency. For numerical simulations subjected to input motion at low frequencies, e.g. 1 Hz and 2Hz, the acceleration amplification factors remain at a low level, around 1.1. This is because the wavelength is much larger than the slope size and thus no significant wave diffraction is produced. When the input motion frequency is above 3 Hz, it can be seen that ground motion is strongly amplified in terms of significant topographic effect. The amplification curves observed are similar in shape when the frequency is greater than 2 Hz.

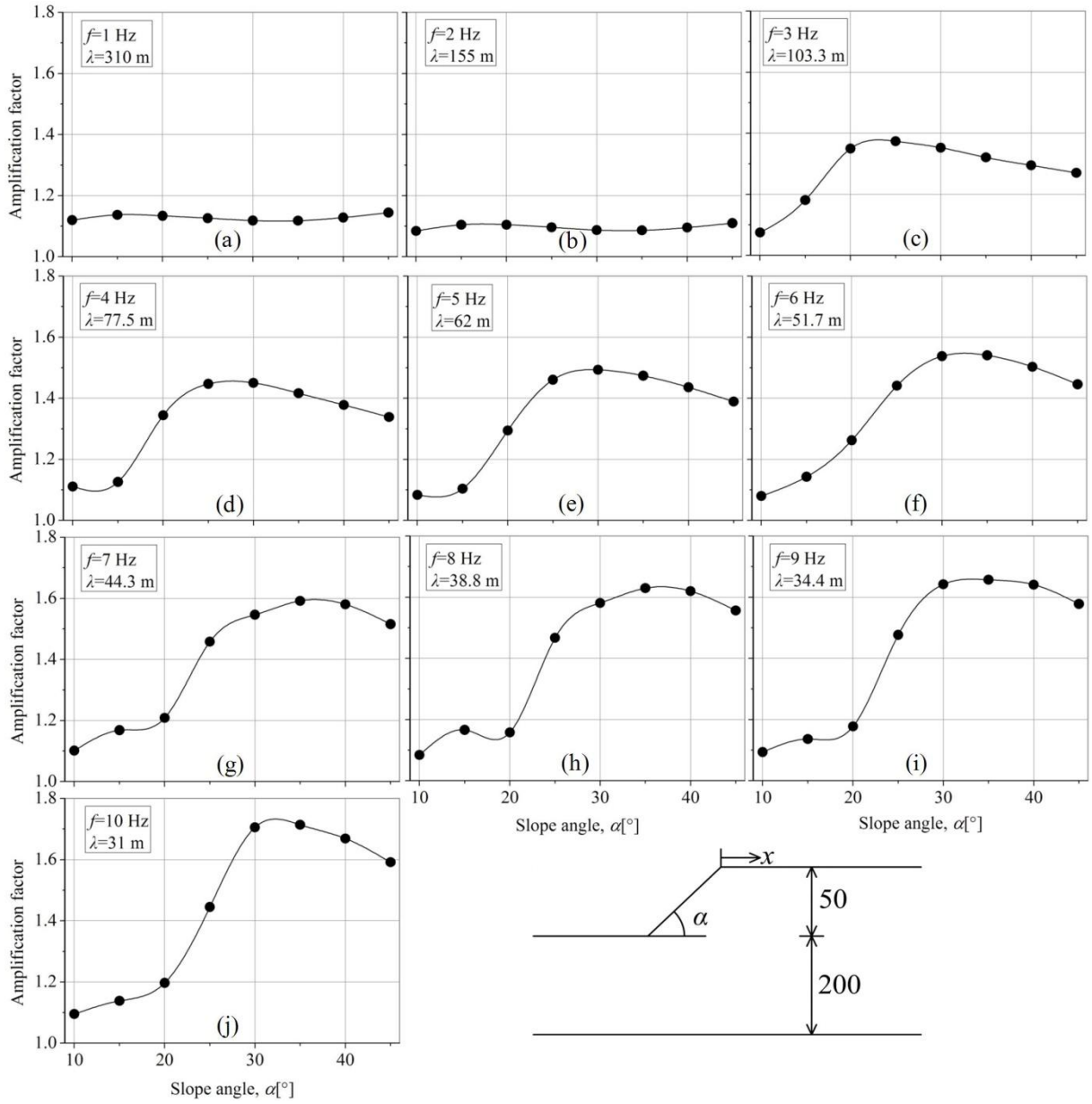


Figure 2.13: Acceleration amplification factor as a function of slope angle of configurations subjected to a Gabor wavelet with different frequencies for slope height h=50 m.

In Figure 2.14, the effects of signal frequency acceleration amplification can be clearly detected in terms of the ratio between the height and the wavelength. For frequencies ranging from 3 to 6 Hz, the acceleration amplification factor increases with the slope height. When the frequency is higher (7-10 Hz), the curves of the amplification factor increase and then decrease with the increase of the slope height. However, for the frequencies f=1 Hz and 2 Hz, the acceleration amplification factors remain steady at a low level because the wavelength is much larger than the slope height. With an increase of input motion frequency, the maximum amplification factor is obtained for a smaller slope height showing that the acceleration amplification is significantly affected by size relationship between the wavelength (frequency) and the slope height.

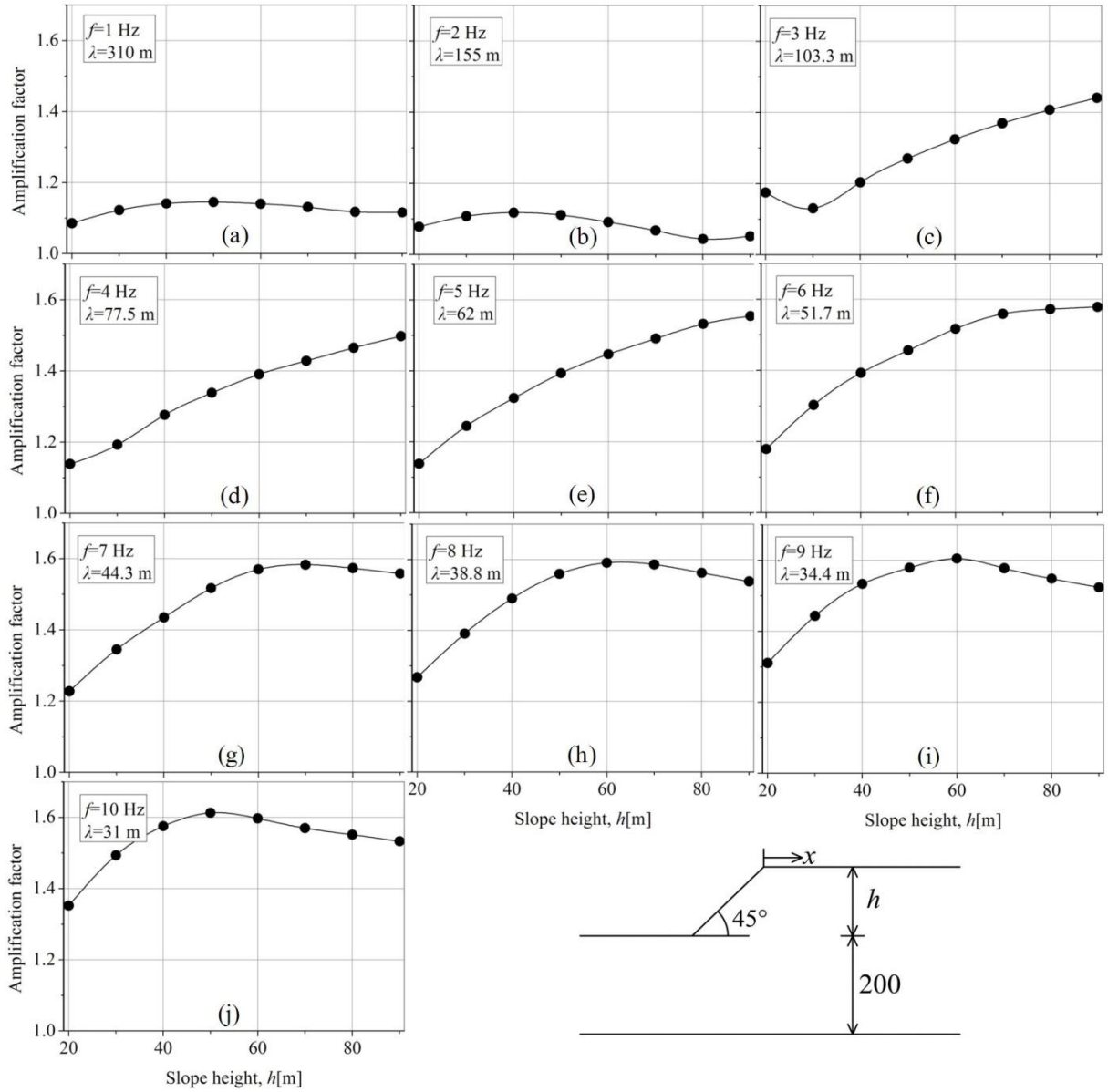


Figure 2.14: Acceleration amplification factor as a function of slope height of configurations subjected to a Gabor wavelet with different frequencies for slope angle α=45 °.

2.4.2 Effects of the number of cycles of seismic input motion

Earthquake duration has been reported to strongly increase with earthquake magnitude, which is one of the most important features of earthquake waves (Castello et al., 2007; Kempton and Stewart, 2006). The number of cycles determines the duration of input motion of univocal frequency. Therefore, Gabor wavelets with cycles of 1, 2, 4, 6 and 12 and Ricker wavelet with 1 cycle were applied to the slope model to assess the effect on the acceleration amplifications. The recorded ground motions are normalized by the reference acceleration and are presented in Figure 2.15, which depicts the seismic motion response as a function of distance to the crest of the slope.

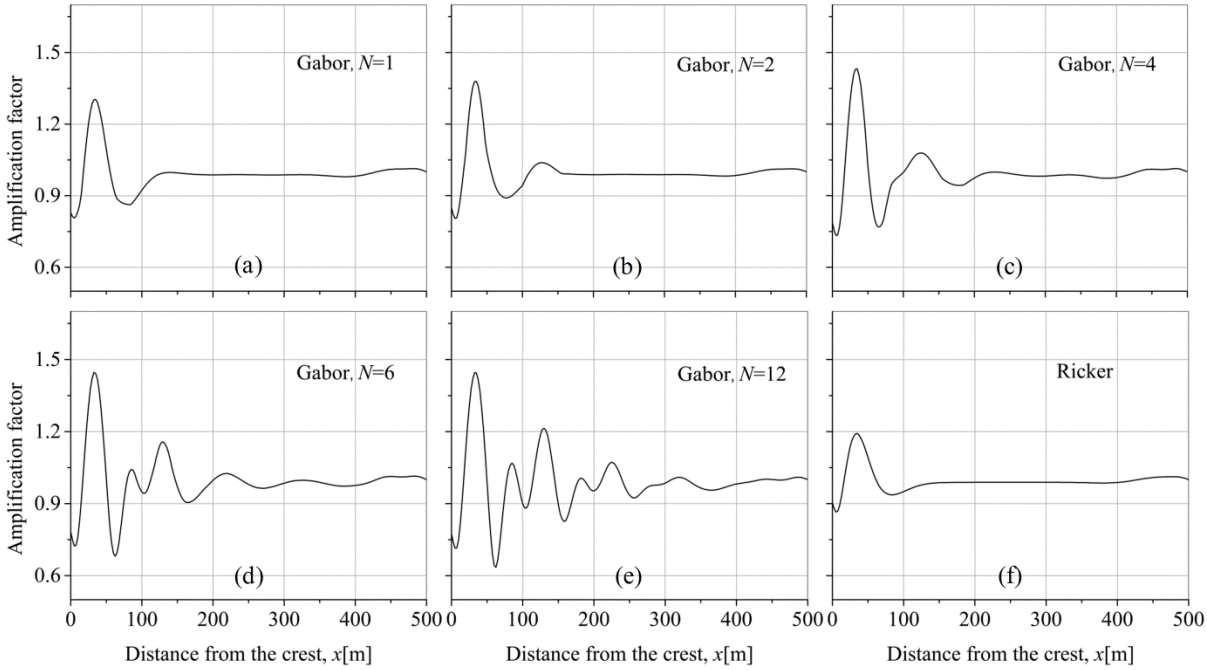


Figure 2.15: Acceleration amplification factor as a function of distance from the crest of a slope subjected to a Gabor wavelet with different significant cycles and a Ricker wavelet for a slope angle α=45 ° and slope height h=50 m.

It can be observed that there are two main characteristics of ground motion amplification in terms of the number of cycles. First, the maximum amplification factor increases substantially with the number of cycles of input motion. The peak amplification factor increases with the number of cycles. For fewer cycles (<4), the difference is significant. For Ricker wavelet excitation, the shape of the curve of the amplification factor is similar to those obtained for the Gabor wavelet, but with a smaller amplification factor. Second, for a higher number of cycles, more secondary peaks of acceleration amplification are obtained. Therefore, long duration (more cycles of input motion) could be responsible for the acceleration amplification that occurs at a large distance to the slope crest.

2.5 Conclusions

Numerical analyses of site effects of slope topography subjected to wavelets with different frequencies were conducted to characterize the acceleration amplification along the surface behind the crest of a slope, and evaluation of the topographic effect on acceleration amplification. The results show significant changes in the acceleration amplification factor due to variations in the slope angle, slope height, signal frequency and signal cycle.

Generally, the acceleration amplification factors along the ground surface behind the crest vary intensely around a value of 1. The topographic effect on ground motion amplification significantly decreases with an increase of the distance to the crest and it tends to zero in the vicinity of the free-field boundary. The intensity of amplification and the distribution of the maximum amplification on the ground surface behind the slope crest changes significantly with slope angle. The maximum amplification is obtained for the model with a slope angle of 32.3 °. The maximum amplification does not necessarily occur at the crest and depends on the slope angle; it is often observed a short distance behind the crest. For a slope angle greater than 32.3 °, secondary peaks of the curve of the amplification factor are seen with an increase in slope angle. In addition, slope height has a significant effect on the magnitude of the acceleration amplification; however, it does not affect the distribution of the

maximum amplification factor when the wavelength is less than the slope height. The edge curvature of the slope can also substantially affect the acceleration amplification. The acceleration amplification observed on the upper ground surface is primarily attributed to Rayleigh waves diffracted in the vicinity of the slope crest.

The problem of topographic amplification is strongly associated with characteristics of the input motion. The frequency content of the input motion has a substantial influence on the amplification magnitude when the wavelength of input motion is less than or comparable to the slope height. The ratio between the slope height and the wavelength can significantly affect not only the amplification amplitude but also the location where the largest amplification is observed. With an increasing number of cycles, the amplification values increase and secondary peaks of the curve of acceleration amplification are produced, which also increase with an increase in the number of cycles of input motion.

In general, the results reveal that there is an interaction between slope topography and input motion. However, the slope topography has a complex effect on the acceleration amplification in terms of the ratio between the wavelength and the slope size, in particular at small-scale sizes. In addition, other factors such as 3D effects and material heterogeneity are not considered in the study. Therefore, it is necessary to conduct more analyses under various conditions in the frequency domain.

Chapter 3: Site effects on seismic ground motions at Xishan Park ridge in Zigong, Sichuan, China

Adapted from Zezhong Zhang, Jean-Alain Fleurisson, Frederic Pellet, 2018. A case study of site effects on seismic ground motions at Xishan Park ridge in Zigong, Sichuan, China. Engineering Geology. DOI: 10.1016/j.enggeo.2018.07.004.

Dans le chapitre 2, nous avons étudié l'amplification topographique en considérant un modèle de pente et en analysant les résultats dans le domaine temporel, ce qui permet d'analyser le mouvement du sol dans le modèle en fonction du temps et de nous aider à comprendre facilement les résultats. Cependant, les ondes sismiques dépendent toujours de la fréquence. La modification du champ d'onde due à une irrégularité topographique est également fortement affectée par la fréquence des ondes sismiques. En particulier, aux hautes fréquences, l'amplification des mouvements du sol sur un site spécifique peut être augmentée (ou parfois réduite) en raison de la présence de particularités à petite échelle (par exemple, la présence possible de formations superficielles, d'intercalations et de fissures dans les roches). Par conséquent, l'analyse des données dans le domaine fréquentiel est un moyen efficace pour mieux comprendre les divers phénomènes qui ne peuvent pas être expliqués dans le domaine temporel. De plus, les simulations numériques devraient être basées sur des investigations géotechniques et des comparaisons avec les mouvements du sol observés.

Dans ce chapitre, les amplifications de site associées au mouvement du sol enregistré sur la crête du parc Xishan à Zigong dans le Sichuan en Chine et produites par le tremblement de terre de Wenchuan en 2008, ont été évaluées à l'aide de la technique du rapport spectral standard (SSR) et de la méthode de la valeur moyenne quadratique de l'accélération (a_{rms}). Une analyse numérique 2D utilisant la méthode des différences finies (logiciel FLAC, Itasca) a ensuite été effectuée et les résultats ont été comparés aux données mesurées sur le terrain.

3.1 Introduction

It has long been recognized that seismic ground motions are modified by local geological and topographic features, such as sedimentary basins, hills, slopes and ridges. In particular, site effects can amplify ground motion, which significantly aggravates the destructive damage that occurs during earthquakes. Examples of such phenomena were observed during the 1989 M_w=6.9 Loma Prieta earthquake (Harris, 1998), the 1999 M_w=7.7 Chi-Chi earthquake (Tsai and Huang, 2000), the 2008 M_w=7.9 Wenchuan earthquake (Bo et al., 2009; Luo et al., 2014), the 2009 M_w=6.3 L'Aquila earthquake (Bertrand et al., 2011; Chiarabba et al., 2009) and the 2010 M_w=7.0 Haiti earthquake (Hough et al., 2010b). Instrumented field studies of topographic effects during earthquakes have qualitatively shown modifications to the ground motion (Assimaki and Jeong, 2013; Hough et al., 2010b; Pellet et al., 2005); however, quantitative evaluations of ground motion amplification remain rare.

Methods for evaluating site effects were developed over decades. One of the most popular methods is the SSR technique. This consists of calculating the ratio between spectra of seismic signals

recorded at a specific study site and at a reference site located on bedrock (Borcherdt, 1970). The key step is to choose a reference site that is not affected by any site effect. Another spectral ratio technique is the Nakamura method (Nakamura, 1989), which is based on the spectral ratio between the horizontal and vertical components of a ground motion recorded at the same station. This method is mainly applied to micro-tremors or, sometimes, to strong motions (Guo et al., 2014) and allows the estimation of the predominant resonance frequency at the local site under consideration. The advantage of this technique is that the selection of a reference site is not needed; however, this method only predicts the fundamental frequency (Dravinski et al., 1996).

Numerical simulation is another popular method to assess site effects, since it is convenient and low-cost. The method is based on geomechanical modeling of the site resulting from geological and geotechnical investigations and predicting wave propagation through the model. The outcomes in terms of calculated recordings at different points of the model can be validated through comparisons with observed ground motions. However, numerical studies that evaluate topographic effects usually give lower amplifications than those measured in field studies (Geli et al., 1988; Paolucci, 2002; Semblat et al., 2002). This can be attributed to many factors, such as the presence of surface materials with low seismic properties, the incidence angle and orientation of the wave field, the wave type, and the three-dimensional (3D) geometry of the topography. Investigations of topographic amplifications with respect to variations in slope angle (Ashford and Sitar, 1997; Bouckovalas and Papadimitriou, 2005; Tripe et al., 2013), topographic irregularity (Nguyen and Gatmiri, 2007), wave incidence angle (Ashford and Sitar, 1997), and wave frequency (Boore, 1972; Tripe et al., 2013) have been widely performed using numerical simulations. A comprehensive review of numerical methods for estimating topographic amplifications can be found in Semblat and Pecker (2009).

The city of Zigong is located in a hilly area characterized by rocky slopes. This city of 3 million inhabitants lies in the southern part of the Sichuan Basin. Seismic activity along several nearby active faults (Figure 3.1a), such as the Longmenshan, Longquanshan and Huayingshan, can produce ground shaking in the study area. Furthermore, this area faces severe seismic hazard because of its complex structural and local topographic conditions. Some studies have been performed, including investigations on seismic hazard (Assimaki et al., 2005) and the relevant site effects (Yang et al., 2011). In 2007, 8 accelerographs were deployed along a ridge located in Xishan Park in Zigong, in order to measure the ground motion amplifications induced by the topography. Wang and Xie (Wang and Xie, 2010) processed the accelerations recorded by these accelerographs during the 2008 Wenchuan earthquake. Their results showed that the maximum ground motion amplification was observed on the hilltop in the frequency range of 1-10 Hz. No substantial spectral amplification was observed at low frequencies (f <2 Hz). Yang et al (2011) performed a numerical simulation to assess the site effects at the Xishan Park ridge and confirmed that the high ground motion amplifications were due to the presence of soft material at the ridge toe. However, investigations on the topographic effects of this ridge are still lacking; a more thorough analysis of the observed ground motion amplifications is needed to analyze the influence of topographic features at the small-scale or of near-surface geological conditions (e.g. the presence of sandstone and marlstone intercalations).

In the current study, the ground motion observed during the 2008 M_w=7.9 Wenchuan earthquake is analyzed using the SSR method. The results from the numerical model are then compared with the instrumented observations. The ground motion amplification is also estimated using observed and simulated ground motions, employing the root-mean-square acceleration (a_{rms}) method in the time domain. The seismic input used in the numerical simulations consists of real earthquake waves, in

contrast to the studies performed by Tripe (Tripe et al., 2013), Nguyen (Nguyen and Gatmiri, 2007) and Lenti (Lenti and Martino, 2012), in which the analyses were performed on ideal model slopes subjected to artificial accelerations.

3.2 Study area

The study area (Figure 3.1a) is situated 246 km to the southeast of the Wenchuan earthquake's epicenter, in a hilly region within the Sichuan Basin, which is characterized by small, shallowly incised hills with elevations between 20-100 m. This area includes the Changyan and Huangjuepo faults (Yang, 2008) and is close to several active faults, such as the Longquanshan and Longmenshan faults (Guo et al., 2014). The rock material is primarily made up of Jurassic mudstones, limestones and sandstones, as well as Quaternary deposits that are mainly distributed along the river (Yang, 2008). The selected ridge is a 72 m high hill, located in the Xishan Park, within the Zigong urban area. This hill has an average slope angle of 15 °, with local considerable variations (Figure 3.1c).

Bedrock outcrops along the toe and the lower part of Xishan Park ridge consist of massive sandstones (quartz, feldspar-rich) interbedded with shales (J. Wasowski personal communication, 2017). At the middle and upper parts of the ridge, the bedrock is mostly covered by Quaternary deposits, including sandy-clayey colluvium with rock boulders, silty clay and artificial fill soil, which does not exceed a few meters of thickness. In addition, the sedimentary sequence is folded with beds dipping about 25 °at the base of the ridge and 30-40 °at its upper part, in the SE or SSE direction.

The local site effects have been reported to aggravate earthquake disasters (Assimaki et al., 2005). An accelerometer array has been in operation since 2007 on the ridge at Xishan Park in order to assess possible seismic ground motion amplifications due to local morphological conditions. This study site was selected because of its apparently simple morphology. The transverse section of the ridge is slightly elongated in the NW-SE direction (Figure 3.1b). There are three reasons for the selection of this site: First, the site is located in a hilly area, where there is considerable topographic relief may potentially induce ground motion modifications. Second, the area is near several active faults. In this region, low-intensity earthquakes always break out from shallow sources, and their high intensities due to active faults are often reported (Lei et al., 2013; Yang, 2008). Third, the rocky formations are covered by thin surficial deposits, and therefore almost all the accelerographs are installed directly on the rock material (Wang and Xie, 2010; Yang et al., 2011). This consequently appears to be a promising site for separating the effects of surficial deposits amplification and topographic amplification.

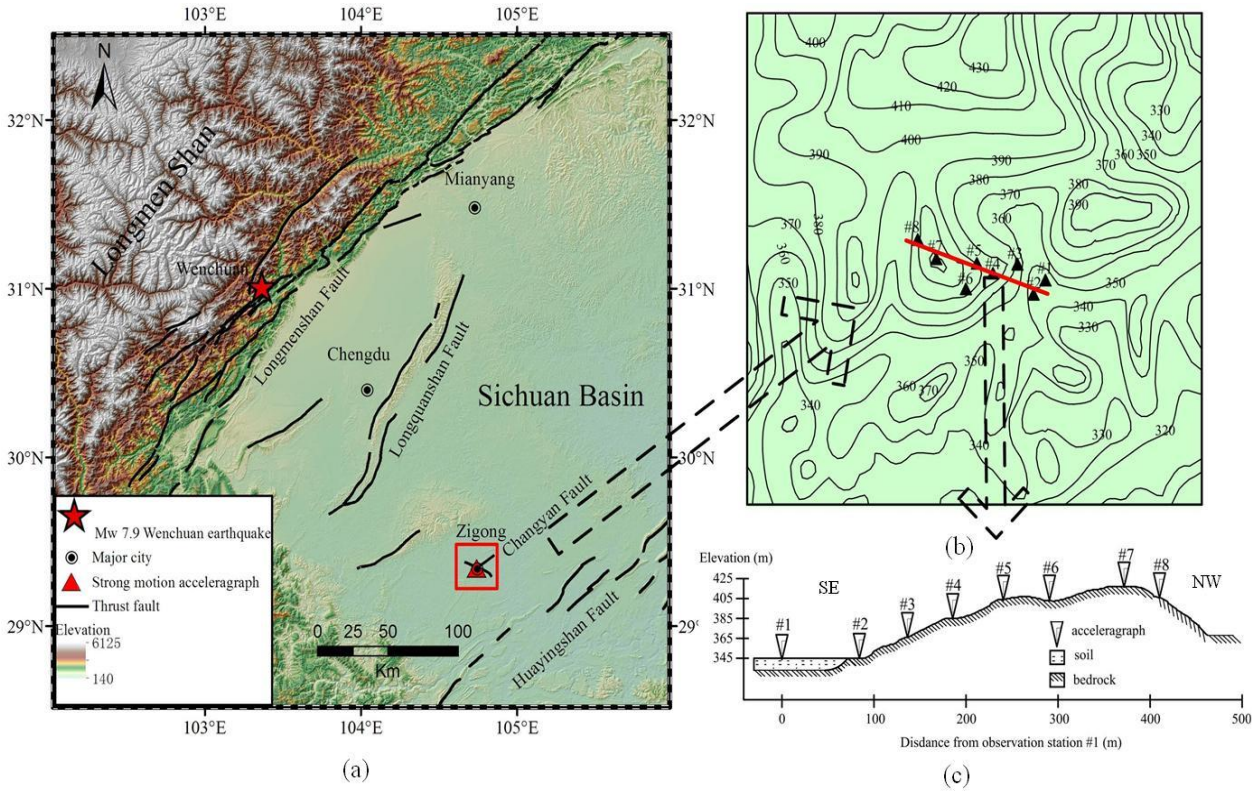


Figure 3.1: Schematic map showing the location of the monitoring stations and local topography. (a) Bird's eye view map, indicating the location of the Zigong study area, which is about 246 km away from the epicenter of the 2008, M_w 7.9 earthquake. Several other active faults that frequently trigger seismic activity are also indicated on the map (Xu et al., 2005; Yang, 2008). (b) Local topographic map, showing the location of the accelerographs installed along a profile across the ridge. (c) Section of the ridge, showing the distribution of the accelerographs along the ridge slope.

3.3 Methodology and Data

The ideal way to evaluate topographic effects is to measure the ground motion at two sites for which all the parameters are the same, except for the topographic features. This is impossible in reality. However, we can choose two different but nearby sites that have similar geological conditions, one of which is located on a relatively flat area; the site effects can then be defined by comparing the ground motion response recorded at the two sites. Based on this idea, Borcherdt (Borcherdt, 1970) proposed the SSR method. The basic procedure consists of comparing data from sites where amplifications are expected, such as those situated on soft sediments, in basins, and on slopes and ridges with data from a nearby 'reference site' located on bedrock.

To carry out this method, it is first necessary to isolate the site effects from the other effects involved in wave propagation and generation. Indeed, a recorded acceleration can be defined as:

$$A(\omega) = S(\omega)T(\omega)R \quad (1)$$

where $A(\omega)$ is the ground motion received by the accelerograph, $S(\omega)$ is the source function of the seismic signal, $T(\omega)$ is the transfer function for the transmission path, and $R(\omega)$ is the amplification function corresponding to the site effects.

Given the spectra $A_1(\omega)$ and $A_2(\omega)$ of recordings of the same event, acquired at the reference and at the studied site, respectively, the SSR method yields a valid estimation of site effects if the reference

site satisfies two conditions. Firstly, it should be located on horizontal bedrock that is not affected by site effects. Secondly, the reference site should be located close to the study site, to ensure that the relative propagation transfer functions $T_1(\omega)$ and $T_2(\omega)$ and the spectral energy $S_1(\omega)$ and $S_2(\omega)$ radiating from the source towards the two stations are as similar as possible. Specifically, the distance between the two sites should be much smaller than the distance from the epicenter.

Under such conditions, it can be assumed that $S_1(\omega)=S_2(\omega)$, $T_1(\omega)=T_2(\omega)$ and, $R_1(\omega)=1$, and we obtain

$$\frac{A_2(\omega)}{A_1(\omega)} = R_2(\omega) \tag{2}$$

To carry out instrumented observations depicting topographic effects on ground motion, an array of 8 accelerographs has been deployed along the Xishan Park ridge since 2007. Each observation station consists of an accelerograph, a power source and communication equipment. The digital strong motion accelerograph consists of 3 'Episensor' accelerometers, developed by Kinemetrics, which record one vertical (UD) and two horizontal components (EW and NS) of ground motions in a bandwidth between 0 and 200 Hz.

The acceleration time histories collected during the 2008 M_w=7.9 Wenchuan earthquake are shown in Figure 3.2. The #1 station was installed on soil and the recorded ground motion was obviously amplified due to geological effects; it is therefore not suitable for use as a reference site. The #2 station was chosen as the reference site because it was installed on bedrock at the toe of the ridge. To evaluate the site effects in the frequency domain, data were processed as follows (Figure 3.3): (1) Baseline corrections were performed for all the acceleration time histories used in our study. (2) Time history windows, including the maximum SV wave amplitudes (from 40 s to 80 s), were chosen from the baseline-corrected data. (3) The windowed time histories were processed using a bandpass filter in the range between 0.1 Hz and 20 Hz. (4) Data in the time domain was transformed into the frequency domain using the fast Fourier transform (FFT) method. (5) The FFT spectra were smoothed using a FFT filter with a 20-point window. (6) Spectral ratios were obtained by dividing the spectrum of ground motion at each studied point by the spectrum of ground motion recorded at the reference site for each of the three components, respectively.

In FFT calculation, a frequency Δf = 0.025Hz was used as the spacing between two adjacent frequencies. This is derived from the equation

$$\Delta f = \frac{f_s}{N} = \frac{1}{T_s} \tag{3}$$

where f_s is the sampling frequency (200 samples per second), N is the number of samples (8000), T_s is the duration of the windowed seismic signal (40 s).

Spectra derived from FFT were smoothed to remove high-frequency noise without affecting the overall signal shape. The FFT Filter smoothing method consisted of the following steps (OriginLab, 2017): (1) The mean of the first 1% data points and the mean of the last 1% data points were calculated. (2) A straight line was traced through these two points and subtracted from the input data. (3) FFT was performed on the dataset acquired in the last step. (4) A low-pass parabolic filter was applied. (5) The inverse fast Fourier transform (IFFT) was performed on the filtered spectrum. (6) Finally, the baseline was added to the dataset. For the FFT filter smoothing method, a running average carried out over a 20-point window was adopted. Each value $\{f_i \mid i=1,2, \ldots,N\}$ of the smoothed time series was obtained

by averaging data points $\{f_m \mid i- n_{pts}/2 < m < i+ n_{pts}/2\}$, where $\{f_i \mid i=1,2, \ldots, N\}$ are the input data points and n_{pts} is the variable defining the window point number.

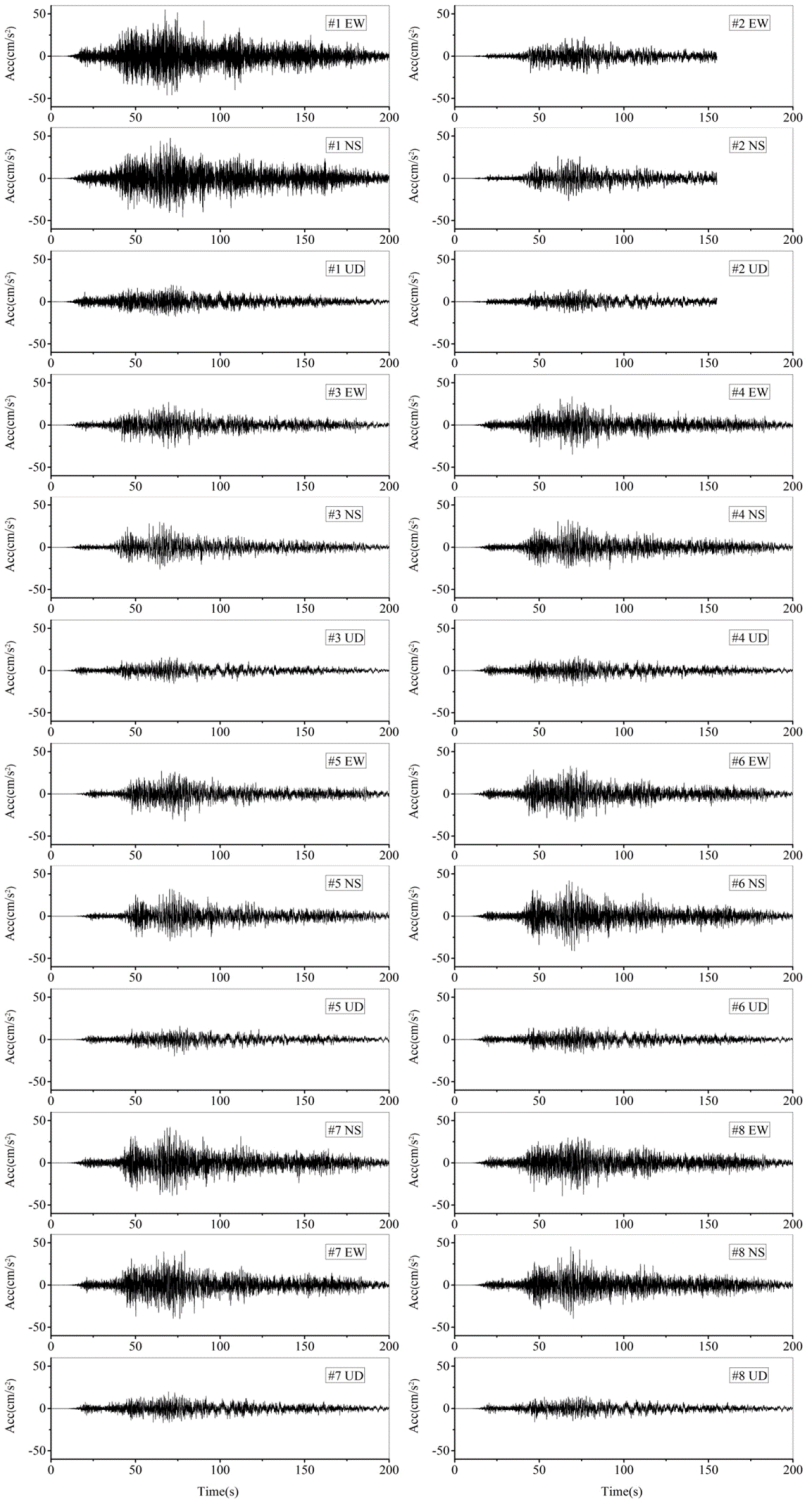


Figure 3.2: Acceleration histories recorded by the accelerograph array on the Xishan Park ridge during the Wenchuan earthquake. The time history recorded at the #2 station is shorter, but this does not affect the results as time histories windowed from 40 s to 80 s were chosen for analysis.

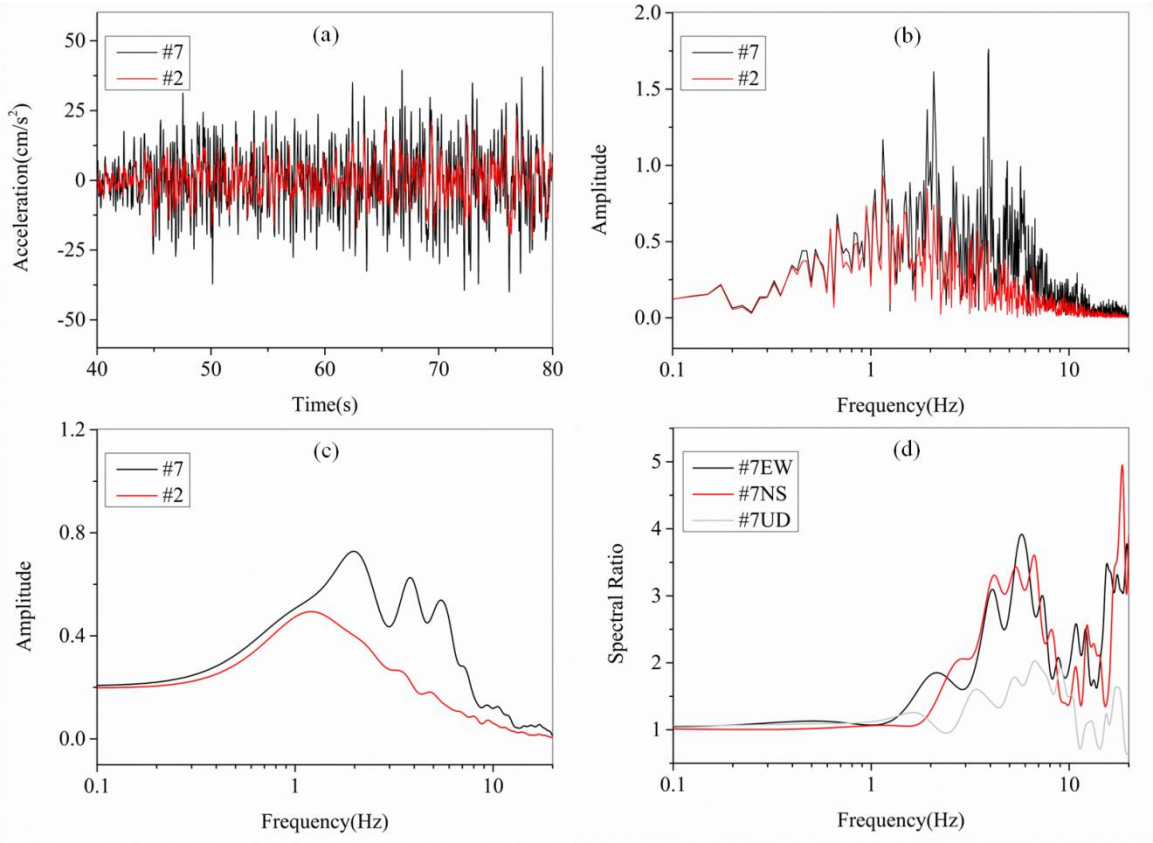


Figure 3.3: Stages of data processing at the #2 (reference) and #7 stations. (a) Windowed accelerations, including the maximum peaks of the SV waves; (b) FFT amplitudes of the windowed accelerations; (c) FFT amplitudes smoothed using a digital FFT filter; (d) spectral amplification ratios at #7 in three directions, respectively.

3.4 Site effects on ground motion

3.4.1 Effects of topography

Figure 3.4 presents the FFT amplitudes of recorded ground motions and the spectral ratios between each specific site and the reference site (the #2 station). The figure shows significant differences in the FFT amplitude, depending on the observation station considered. Spectral energy is mainly concentrated between 0.5 and 6 Hz, and there are two significant peak amplitudes in the frequency ranges of 1-2 Hz and 3-6 Hz for the EW component. A similar pattern is observed for the NS component. On the other hand, at the reference site, there is only one amplitude peak near a frequency of 1 Hz. This indicates that the signal is significantly amplified in a frequency range of 3-6 Hz. The spectra at low frequencies (below 1 Hz) do not show any significant amplification. This is explained because the low-frequency signals have larger wavelengths that make them pass easily through topographic features without substantial wave diffraction. Rock material on the ridge has S-wave velocity of 1000 m/s at frequencies lower than 1Hz; thus, the wavelengths are larger than 1000 m, which is significantly larger than the ridge height (about 72 m) or width (about 370 m). Due to such a large difference between wavelength and ridge dimension, it is difficult to expect any substantial generation of wave diffractions. The spectrum at the top of the ridge (the #7 station) shows peaks in amplitude at 2, 4 and 6 Hz for the EW component, while the peak frequencies in the NS direction are found at 1, 2.5 and 4 Hz. The differences, in terms of observational direction, have been reported to possibly be due to 3D topographic effects (Paolucci, 2002), effects of near-surface geological settings

(Pischiutta et al., 2012), and polarization (Del Gaudio and Wasowski, 2007, 2011; Spudich et al., 1996). Furthermore, the peaks of the spectra for the EW component obtained at station #6 occur at 2 and 4 Hz. The additional peak amplitude at station #7 at 6 Hz could be caused by small-scale topographic features and local variation of the lithologic characteristics (intercalations, fracturing and weathering) between stations #6 and #7, which suggests that site effects can be closely related to the size relationship between topographic geometry and wavelength (frequency).

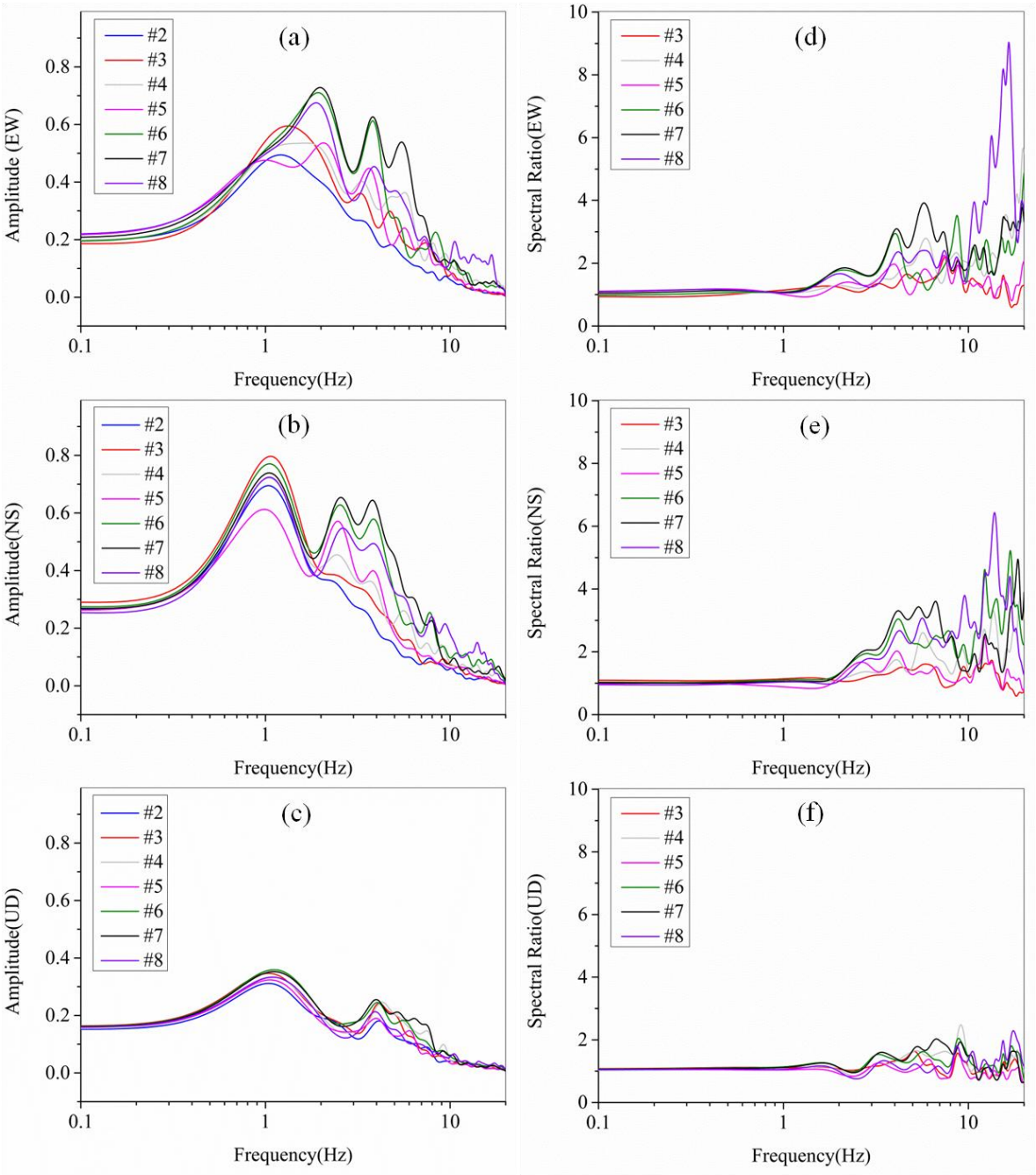


Figure 3.4: FFT amplitude spectra observed at sites #2-8 and spectral ratios relative to station #2 for components East (a, d), North (b, e) and vertical (c, f).

It can also be observed that for the NS component the peak amplitudes are slightly larger and the peak frequencies are lower in comparison to the EW direction. This could depend on 3D topography and near ground surface geological setting including interbedded shales and significant folds, which contributes to differences in ground motion responses for the two horizontal components. For the UD

(vertical) component, the spectra are relatively smooth, and there are no significant differences among the different observation stations. Larger spectral amplitudes can be related to P and Rayleigh waves produced by wave reflection and diffraction when SV waves impinge on the free surface, especially in the vicinity of the ridge toe and top.

In order to analyze the spectral amplification in the frequency domain, the station located at the toe of the ridge (#2) was selected as the reference. Spectral ratios relative to it were computed for the three components of ground motions recorded at all the other stations (#1, #3-8). The spectral ratios of each component for stations #3-8 are plotted in Figure 4. Systematic spectral amplification was obtained at frequencies larger than 2 Hz for both the EW and NS components. For the NS component, the maximum spectral amplification was seen at station #7 in the frequency range between 3 and 8 Hz. In the higher-frequency domain (>8 Hz), the largest spectral amplification was obtained at station #8. A similar pattern of spectral amplification was observed for the EW component, with the only difference being that, in the frequency range between 8 and 10 Hz, the maximum amplification was obtained at station #6. Small-scale features of relief, such as rock fracturing and ridge step, have a strong impact on the ground motion amplifications at high frequency. Thus, the observed very high amplifications at station #8 at frequencies larger than 10 Hz, are likely due to small-scale factors. Moreover, substantial differences of amplification at such high frequencies were observed for the two horizontal components, that suggests a significant possible azimuthal dependence of small-scale relief effects on ground motion modification.

3.4.2 Effects of surficial soft deposit

The major amplitude peaks of the FFT spectra of the accelerations recorded at stations #2 to #7 were obtained in the frequency range between 1 and 2 Hz. However, the peak with the highest amplitude was observed at station #1 in the frequency range between 6 and 8 Hz (Figure 5), although no visible amplitude peaks were seen at the other stations. It is conjectured that, in presence of a surficial soft deposit of low shear wave velocity overlying a stiffer substratum, the seismic waves including SV waves, P waves and generated surface waves are trapped within the upper layer, and their overlapping and interference determine a high energy concentration at a specific site resonance frequency. Thus, it is likely that this phenomenon is responsible for the spectral amplification observed in the frequency range 6-8 Hz at station #1. The spectral amplifications for the NS and EW components at station #1 have comparable peak amplitudes obtained at the same frequencies.

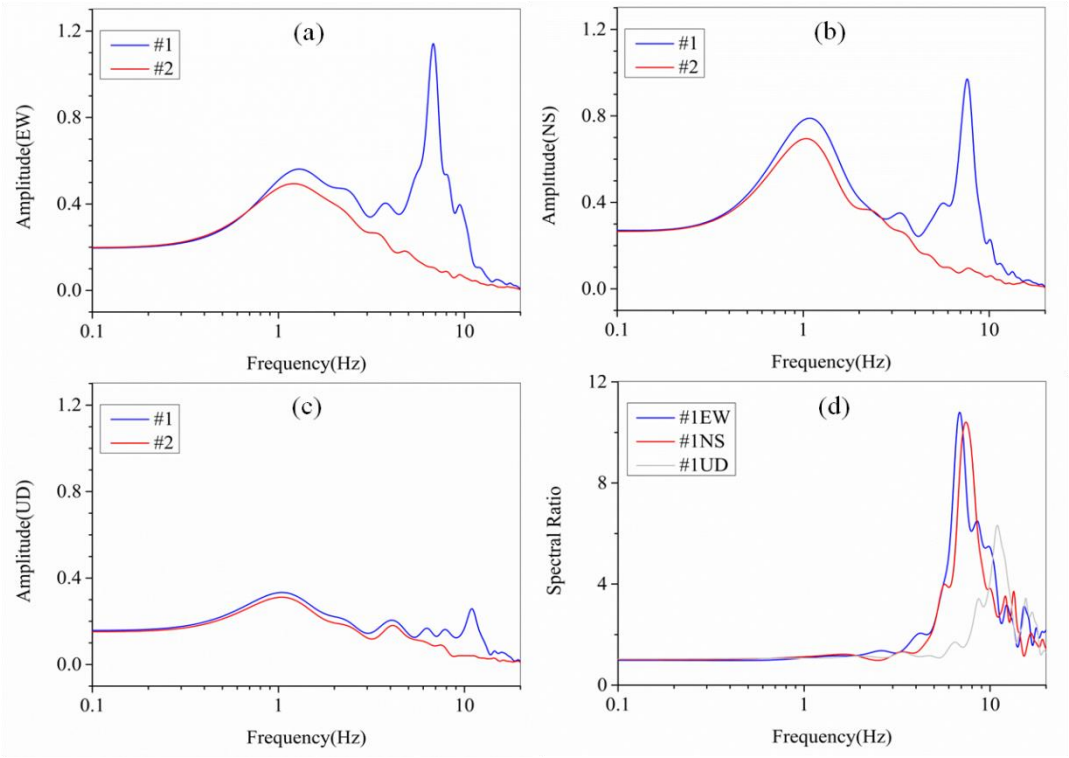


Figure 3.5: FFT amplitude spectra (a, b, c) for sites #1 and #2 in three directions and spectral ratios between them (d). The results show that there is significant amplification between 7 and 8 Hz, which is correlated to the soil layer resonance frequency.

When the incident SV waves impinge on the free surface, reflected SV waves and P waves are generated (see Figure 3.6), resulting from coupling effects between the P and SV waves caused by displacement and traction continuity conditions on the free surface. P waves are longitudinal waves and vibrations occur along the propagation direction. Rayleigh waves are also strongly produced in the vicinity of the slope corners and their elliptical particle motion tends to be considerably 'flattened' when a soft surface layer overlies a stiff bedrock (Asten, 2004), thus contributing to the observed greater horizontal than vertical motion. Therefore, vertical motion can be detected on the ground surface. The peak amplification for the vertical component at station #1 is observed in the frequency range between 8 and 12 Hz, which is similar to that obtained for the vertical component at other stations. All the spectral ratios for the vertical component have lower amplitudes than those of the horizontal components, but the horizontal spectral ratios and the corresponding vertical ones resemble one another in their frequency characteristics.

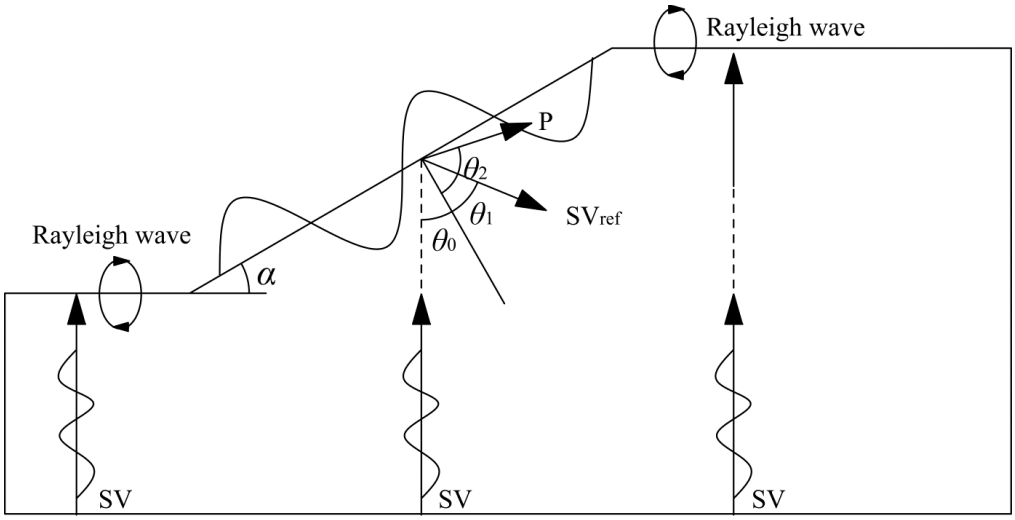


Figure 3.6: Propagation of incident SV waves, reflected P waves and SV waves and diffracted Rayleigh waves near the slope.

3.5 Numerical analysis

A 2D, full-scale prototype ridge model was created and analyzed using the finite difference method program FLAC 8.0 developed by Itasca (Itasca, 2016). Since there is a lack of specific data for the study site, the material properties were obtained from a literature-based statistical database on the soil and bedrock in the study area. The statistical shear wave velocities of the bedrock are plotted in Figure 7. With regard to soil weathering conditions, the shear wave velocities of the soil and bedrock in the whole half-space were set to V_{soil}=250 m/s and V_{rock}= 1000 m/s. The detailed parameters are listed in Table 1. Rayleigh damping with a small damping ratio of 0.5% was applied to the model material. Calculation points were selected to correspond to the accelerograph station locations.

The acceleration time history recorded at station #2, with a modification in its amplitude, was applied at the bottom of the ridge model. There are three reasons why it is necessary to modify the acceleration before it is used as signal input. First, in a numerical model consisting of an ideal medium free from damping and site effect, the wave amplitude recorded on the ground surface is twice as much as that of the incident waves, because of interference between incident and reflected waves at the free surface. Second, ground motion recorded at station #2 should be deamplified due to the site effect. Third, seismic wave energy can be attenuated when it travels through the media due to material damping. Therefore, the input signal representative of the waves at the base of the model was obtained through the following steps: (1) The initial numerical simulation was carried out using the recording obtained in the NS direction at station #2 as input. (2) The input signal was reduced by an amount depending on the ratio between the peak spectral amplitude of the predicted acceleration at station #2 and that of the original instrumental recording. (3) The simulation was repeated using the reduced input signal and the results compared with the experimental recording. Steps (2) and (3) were repeated until there was an optimal agreement between predicted and experimental peak values. In this way, the application of a reduction of 24.7% to the original acceleration recorded at station #2 was adopted to define the input signal.

To determine the unknown soil thickness under station #1, 1D models with different soil depths were tested, and the selected signal input was applied to the bases of these models. A preliminary estimate of the fundamental frequency of the elastic response for the simple shear condition was

obtained by the theoretical equation $F_o = V_s/4h$ (where F_o is the resonance frequency, V_s is the S-wave velocity and h is the soil thickness). By observing the spectral ratio (Figure 3.5) of ground motion recorded at station #1, significant spectral amplification was seen in the frequency range 6-8 Hz. A material with a shear wave velocity of 250 m/s was used in a numerical simulation to mimic the soft deposit. Thus, the thickness of the soft deposit can be derived according to the theoretical equation as 7.8-10.4 m. Numerical analyses for 1D models with a soil depth of 6-10 m were carried out. The FFT amplitudes of the ground motion obtained from these 1D numerical simulations are displayed in Figure 8. Since the largest peak amplitude was observed in the frequency range 6-8 Hz for the 1D model with an 8 m soil layer, this was used as the soil thickness in the 2D numerical analysis.

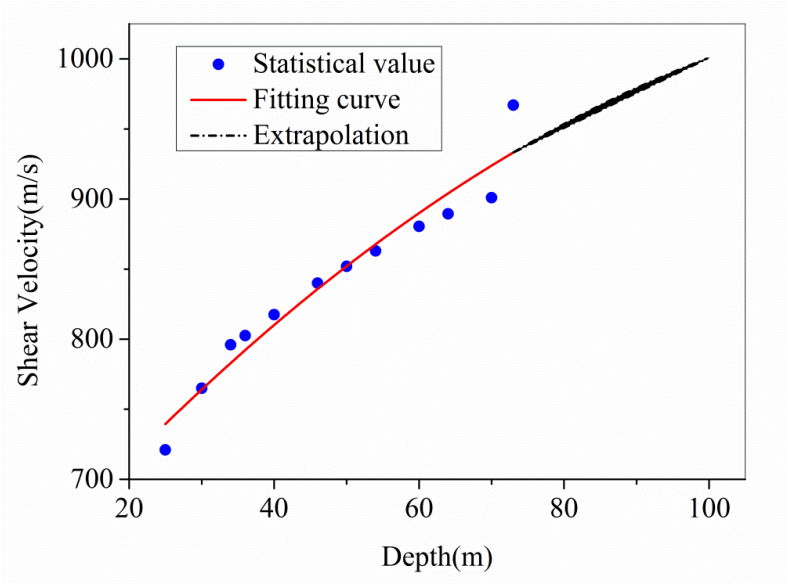


Figure 3.7: Statistical shear wave velocity of the bedrock in the study region.

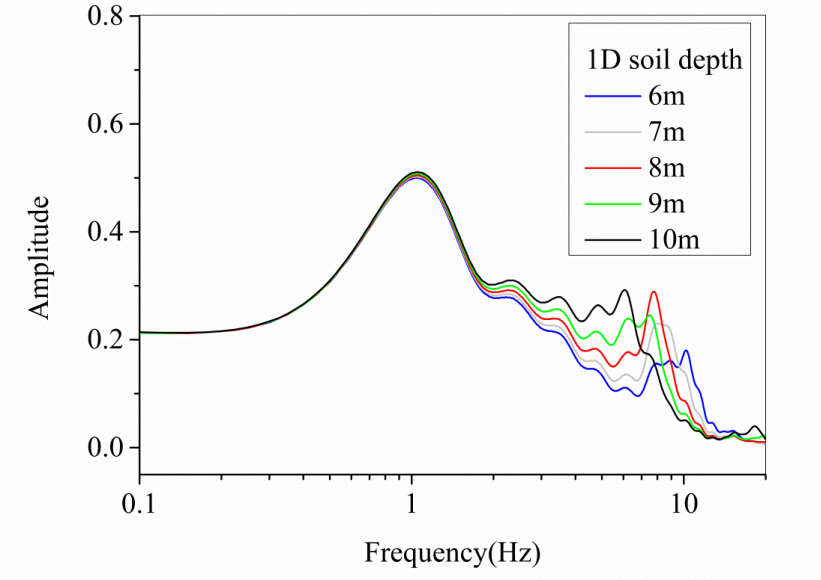


Figure 3.8: The FFT amplitude spectra of ground motion obtained from 1D numerical simulations.

Table 3.1: Material parameters used in the numerical simulations.

	Density (kg/m^3)	Young modulus (MPa)	Poisson's ratio	Shear wave velocity (m/s)
Soil	1850	307.6	0.33	250
Bedrock	2000	5208	0.30	1000

3.5.1 Results of the analysis in the frequency domain

Figure 3.9 presents FFT spectra of the ground motion in the frequency domain. The results from both the numerical simulations ("predicted") and observations relative to the NS component ("recorded") are given in the same plot for comparison. Overall, Figure 3.9 shows that the ground motion obtained from the observations and numerical simulations are similar, although the latter slightly overestimates amplitudes at low frequency and underestimates those at high frequency. However, the peak amplitudes are obtained at the same frequencies, which demonstrates that the properties considered for the rock and soil material were correctly defined.

For frequencies of 2–4 Hz there is a significant difference between the results derived from the numerical simulations and those of the observations; at the sites on the hill, the computed spectra give smaller peaks of amplitude or even some small valleys. For FFT amplitudes of field recordings, peaks are seen at 2-4 Hz at stations #2-8, even though they are small at station #2 and 3. Amplitude differences can be related to the different effect of the topographic amplification of the ridge at frequency 2-4 Hz, which is enhanced at stations #4-8, but is attenuated at stations #2 and #3 installed at the ridge toe. In the numerical simulation, corresponding peaks can be found at frequencies of 2-4 Hz at stations #4-8 and small valleys are observed at stations #2-3. This clearly shows that, in a frequency range of 2-4 Hz, the ridge model has a strong deamplification effect at the ridge toe, while it is less than expected on the ridge top. It should be noted that the input signal, applied to the bottom of the numerical model, is derived from the recording at station #2 located at the ridge toe and thus has reduced energy in the frequency range of 2-4 Hz due to the significant deamplification effect. This can partly explain the lower peaks in the FFT amplitude of numerical simulations at the frequency range 2-4 Hz compared to the field observations. It is also possible that the presence of interbedded layers in the ridge and 3D topography play a role in further amplifying ground motion at such frequencies.

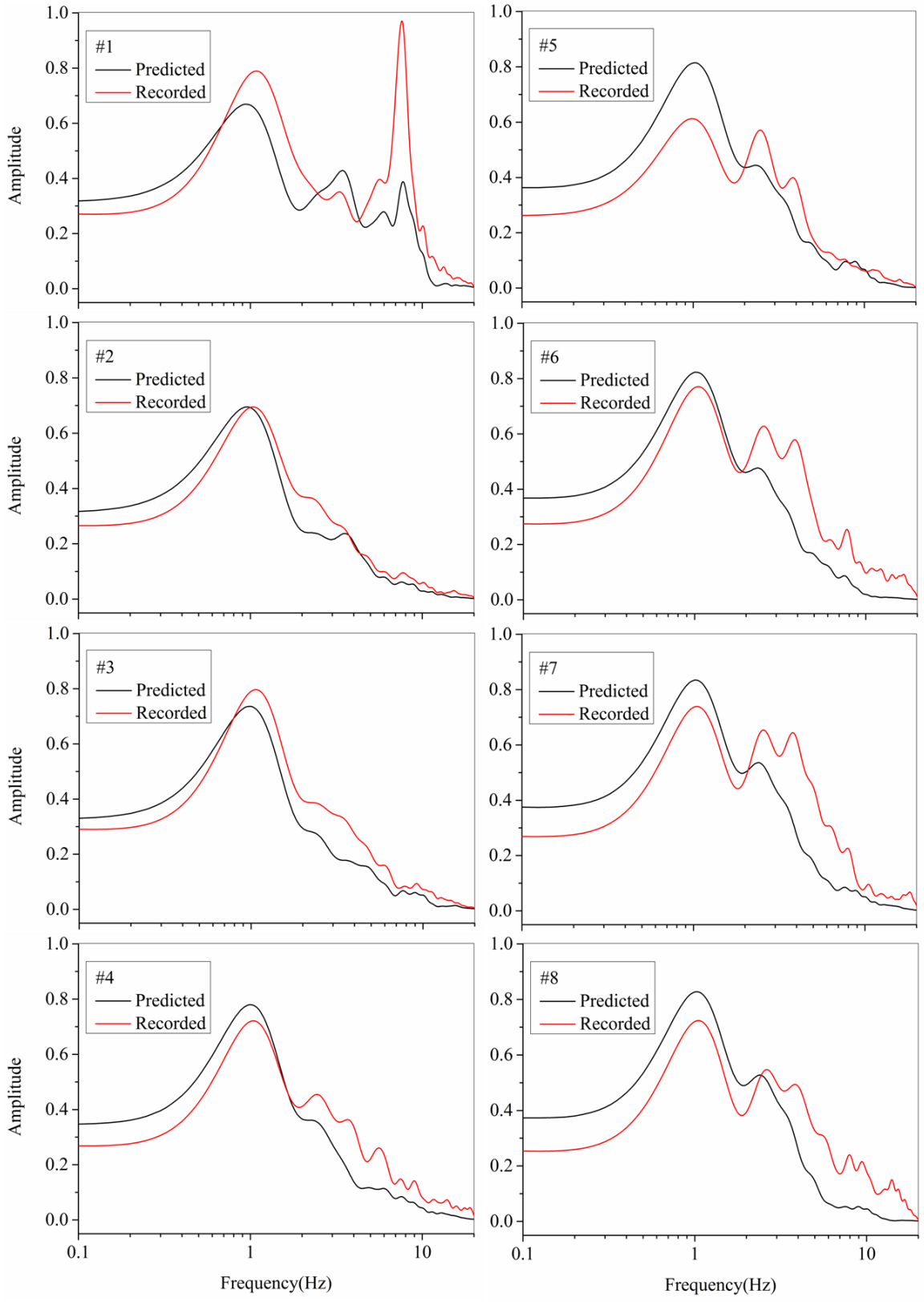


Figure 3.9: FFT amplitudes of recorded and computed ground motion for each observation station. Similar trends are observed between the field observations and the numerical results.

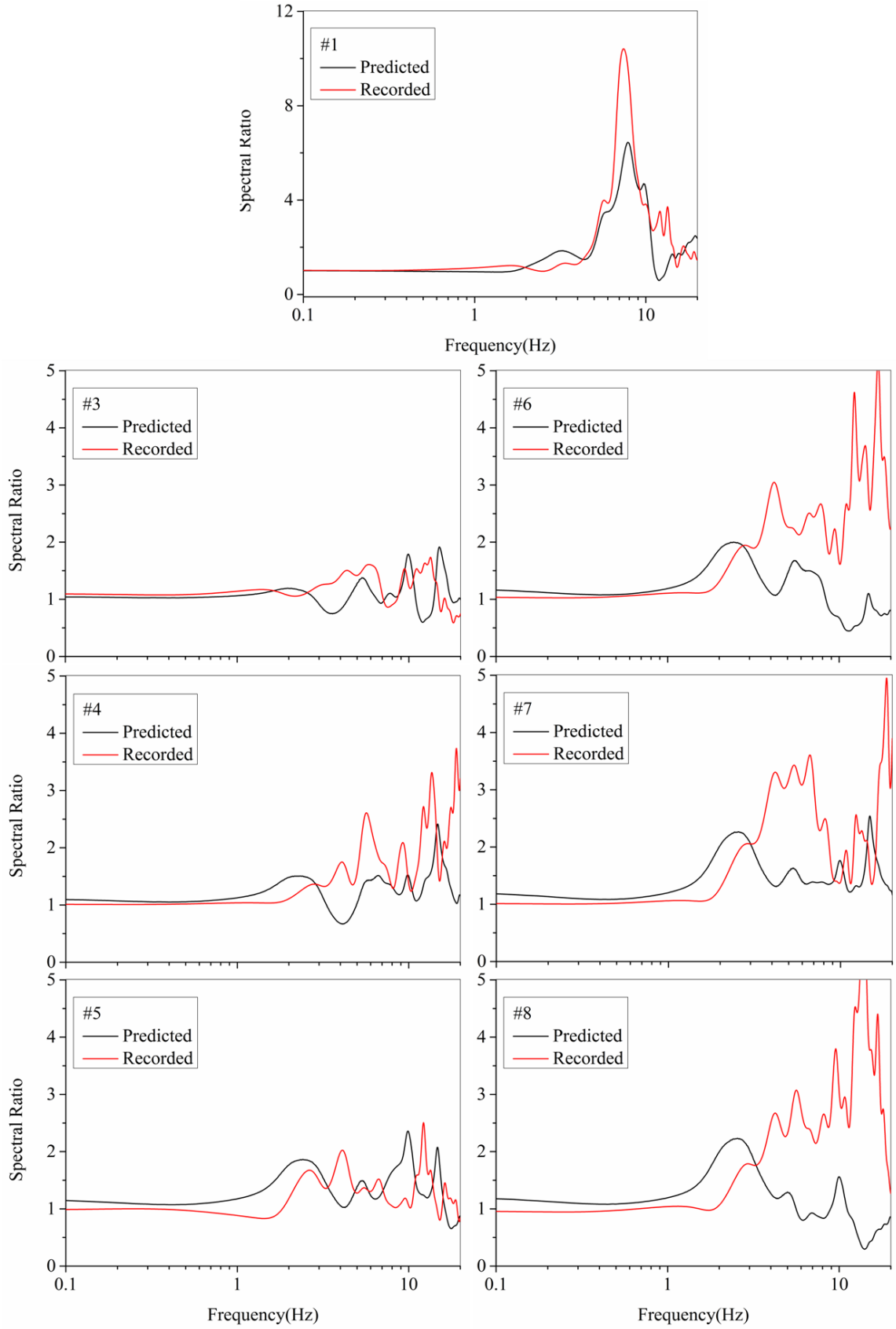


Figure 3.10: Spectral ratios of observed and computed ground motions for each observation station.

Figure 3.10 displays the spectral ratios calculated for all the observation stations in terms of both simulated and recorded ground motions. A similar pattern for the recorded and numerical spectra is obtained at observation station #1, for which the largest spectral amplifications are observed in a

frequency range between 6 and 8 Hz; the simulated values are not much lower than the experimental ones. At observation stations #3-5, the simulated spectral ratios display amplitudes that are comparable to the observed spectral ratios. In contrast, at stations #6-8, the numerical simulations strongly underestimate the ground motion amplification at frequencies greater than 3 Hz and, in fact, deamplification can occur at higher frequencies. The possible reasons for the differences between the simulated and experimental spectral ratios of ground motions are as follows: (1) 3D effects in the surface topography are ignored due to model simplicity in the simulations. (2) The simplified 2D model does not account for local changes in the subsurface geology due to weathering processes, e.g. existing buried layers. (3) A Rayleigh damping ratio was used for the whole model domain to quantify wave energy dissipation. It does not adequately represent the attenuation for frequencies > 3 Hz and thus too much energy was absorbed for waves arriving at sites with a relatively long path.

Different seismic recordings show different characteristics due to the effect of the wave source and propagation path, which may affect ground motion amplification. Since the local seismic arrays have not recorded other earthquakes, international databases of earthquake recordings were used for signal inputs to the numerical simulation (Table 3.2), in order to evaluate the effect of characteristics of input ground motion on amplification. All the selected earthquake recordings were obtained from accelerometers set up on bedrock. They have different amplitudes, frequency content and duration, and therefore can be used in a numerical simulation to mimic random seismic events. The comparative results of ground motion amplifications for the ridge model subjected to recordings from different earthquakes are shown in Figure 3.11. It can be seen that the differences in ground motion amplification in terms of signal input characteristics are so slight that they can be ignored compared with the site effects.

Table 3.2: Seismic recordings used in the numerical simulation

earthquake	Magnitude	Peak of acceleration (gal)	Strong-motion station	Hypocentral distance (km)	Site Geology
El Salvador 2001-01-13	M_w:7.6	187.0	UCA station PA	95.7	rock
Chichi 1999-09-20	M_w:7.6	35.1	CWB station TAP069	118.1	rock
Izmit-Kocaeli 1999-08-17	M_w:7.4	40.2	KOER station 769	86.3	rock
Michoacan 1985-09-19	M_s:8.1	97.6	UNR station SUCH	228.0	rock
Chamoli 1999-03-28	M_w:6.6	61.1	IITR station tehr	89.7	rock

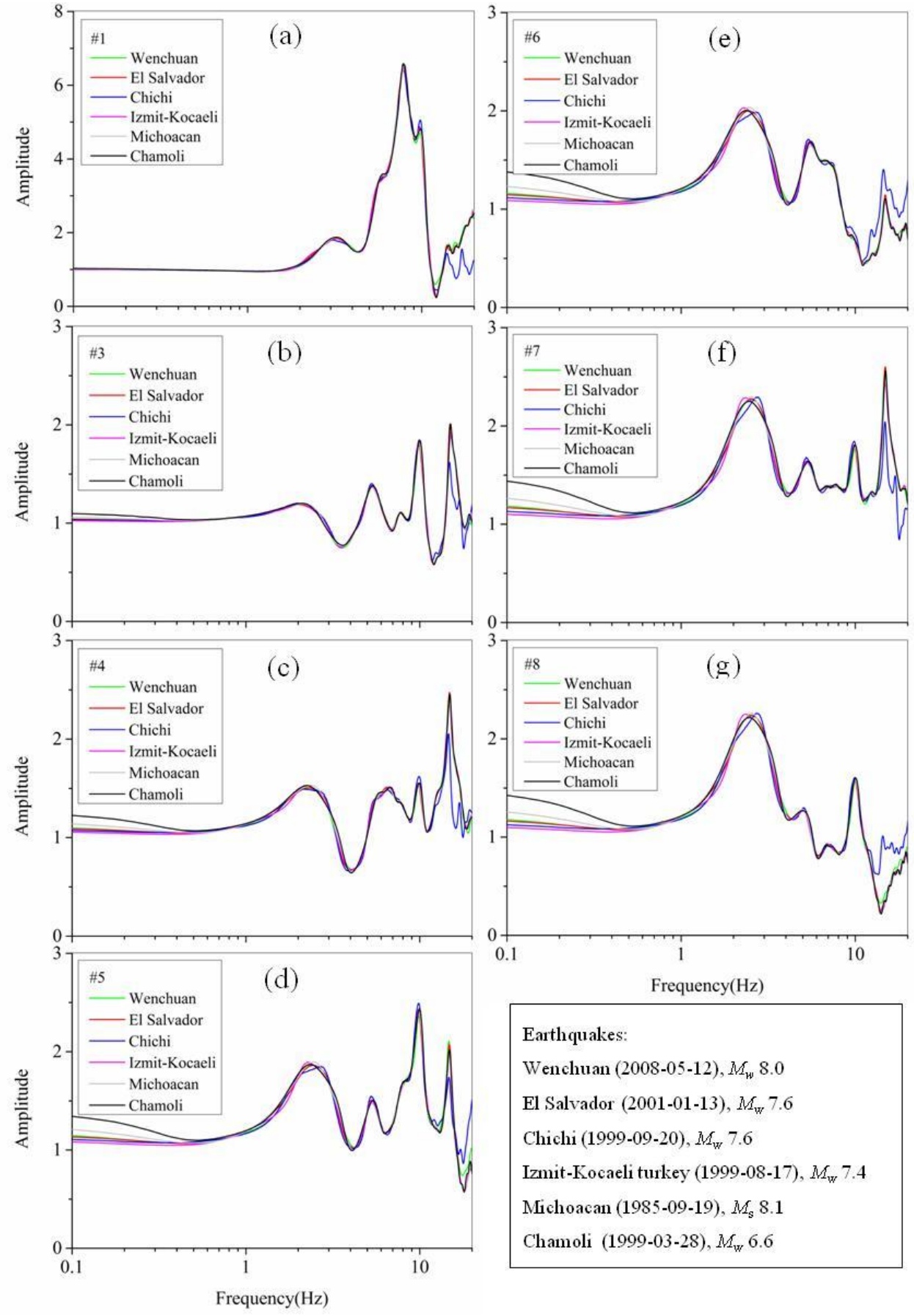


Figure 3.11: Comparison of spectral amplification ratios for the ridge model subjected to different input motions.

3.5.2 Results of the analysis in the time domain

Time domain analysis, which gives the behavior of a signal over time, processes the data over a time interval. This allows analysis of ground motion with respect to time for the signal. A common way to obtain acceleration amplification in the time domain is to compute the ratio of the recorded peak acceleration at a given site and at a selected reference site. However, as a random parameter of ground motion, peak acceleration does not necessarily represent or characterize entire acceleration time histories, which involve other parameters such as frequency, duration and amplitude, for two reasons. First, for strong earthquakes ($M_s \geq 5$) occurring close to the recording site, as a parameter that is assessed over a short time interval, the peak acceleration cannot account for the large-scale features of the entire ground motion, including its source and propagation properties. Therefore, highly random variations are observed, even for quite similar site conditions, earthquake magnitudes and distances from the epicenter. Second, even though the magnitude of the peak acceleration is correlated to the earthquake duration, it is subject to saturation phenomena (Hanks and McGuire, 1981); if the duration of a strong earthquake is beyond a certain value, the peak acceleration does not increase further.

Because of these limitations for using the peak acceleration as a parameter of ground motion, the root-mean-square acceleration is proposed to represent the main characteristics of the ground motion. The a_{rms} is a broadband integral measure, which is certainly a more stable method of representing ground motion than the single value of peak acceleration, possibly related to an individual high-frequency amplitude measurement in the time domain.

In this respect, Arias (Arias, 1970) proposed a new metric for measuring ground motion intensity through a variable called "Arias intensity" (I_A), which is defined as:

$$I_A = \frac{\pi}{2g} \int_0^{T_d} a^2(t)\, dt \tag{4}$$

where T_{d} is the duration over which the signal remains above a threshold, and a(t) is the acceleration time history.

The seismic waves arriving within selected windows, mainly consisting of S waves, are used in the analysis in the present study. The ground motion can be regarded as a stationary process, so the energy per unit time can be represented as:

$$a_{rms}^2 = \frac{1}{T_d} \int_0^{T_d} a^2(t)\, dt \tag{5}$$

The ratio of the a_{rms} value between the site under consideration and the reference site is then used to represent ground motion amplification. The amplification ratios for the horizontal components are given in Figure 3.12.

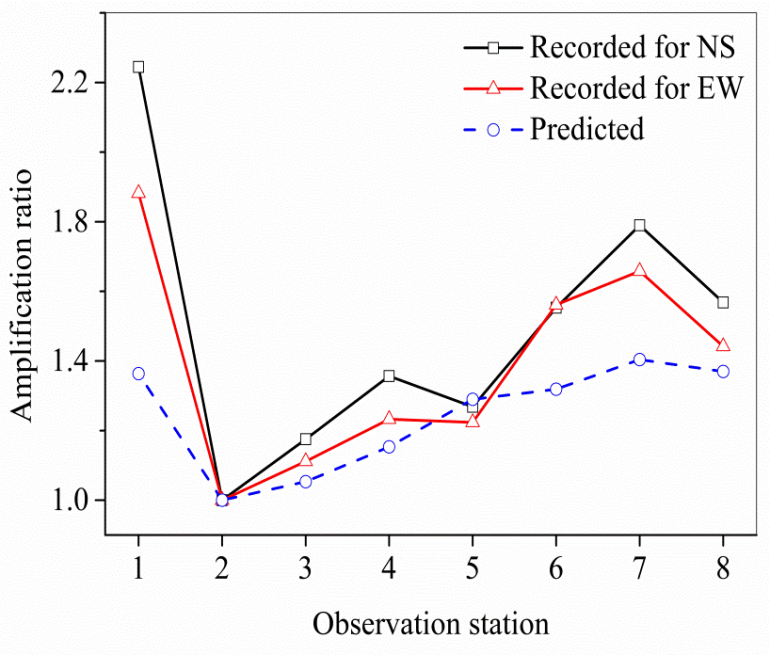


Figure 3.12: Amplification of ground motion in terms of a_{rms} ratios at the 8 observation stations with respect to the reference station (#2) for the NS and EW components of the recorded ground motion and the horizontal ones predicted by the ridge model.

The ground motion amplifications for the field observations are slightly higher at the majority of the observation stations than those seen from the simulations. This is in agreement with the analysis in the frequency domain. The amplification ratios are usually lower than 2.0, except for the high value of 2.3 at station #1 that was obtained for the NS component. In the field observation, the ground motion amplifications at station #1 are much higher than those at other stations because of the presence of a soil layer that traps the waves and may therefore amplify them. The highest amplification ratio along the ridge was obtained at station #7, which is situated at the top of the ridge. The simulated ground motion amplifications are relatively low compared to the corresponding recorded values, especially those at stations #1 and #7. For the underestimated amplification at station #7, this is in agreement with previous studies (Ashford and Sitar, 1997; Geli et al., 1988), who found that the amplification ratio at the crest of a ridge slope remains lower than 2 even though the wavelength of the signal is comparable to the ridge width. In addition, the underestimation of amplification at station #1 could be due to an impedance contrast, assumed by the model, that is lower than the real one, or by the inability of the simulation to reproduce wave trains (e.g. surface waves) arriving at the site and travelling horizontally through the alluvial deposits.

3.6 Conclusions

In the present study, the available acceleration time histories recorded by accelerographs located along a ridge during the 2008 M_w=7.9 Wenchuan earthquake were analyzed using the SSR technique in order to characterize the effect of the ridge on ground motion amplifications. Numerical simulations were performed for comparison. The results underline that the amplification values change with the location of the monitoring station. Among the stations located on the hill, the amplification was found higher at the top of the ridge; however, the strongest ground motion amplification was obtained at station #1, located on soil material at the foot of the ridge.

The results reveal that site amplification is mainly observed at frequency ranges between 3 and 8 Hz and between 10 and 20 Hz, while the FFT spectra show that the signal energy is mainly distributed in a frequency range between 1 and 6 Hz. At frequencies lower than 10 Hz, the amplification ratios remain under 4 at stations on the hill. At observation station #1, the maximum spectral amplification factors (larger than 10) were obtained at a frequency range 6-8 Hz due to the geological effect resulting from the presence of a soil layer. It is possible that small-scale factors, are responsible for the high spectral amplification at high frequencies (f >10 Hz) observed at station #4 and #8 for the EW component and at stations #6 and #8 for the NS component. The ground motion amplifications for the NS component are slightly higher than the corresponding ones for the EW component, which suggests a possible azimuthal dependence of site effect.

The simulated results are generally in good agreement with the recorded data, although the simulations reflect a slight overestimation at low frequencies and an underestimation at higher frequencies. Moreover, the "simulated" peaks of the spectral amplifications are almost lower than those derived from the field records. Significant underestimation of the predicted amplification is observed at high frequencies (f>3 Hz). The strong attenuation effect on input motion at high frequency highlights the shortcoming that a signal damping ratio does not adequately represent the energy dissipation in the numerical simulations. Analyses in the time domain also predicted amplification ratios lower than 2, except for the NS component at station #1, where the amplification ratio reached 2.3.

In general, discrepancies between the predicted amplifications and the field observations can be observed in both the frequency domain and the time domain. Changes in ground motion amplification are affected by a variety of factors; in particular, in the frequency domain, topographic amplifications associated with small-scale factors and local variation of lithologic characteristics (possible presence of intercalations, fracturing and weathering), show complex behaviors. In addition, the simplified model neglects 3D effects, material heterogeneity, etc., which may lead to an underestimate or overestimate of the ground motion amplification, in particular at high frequencies.

Chapter 4: Site effects contributing to triggering the Las Colinas landslide during the 2001 M_w=7.7 El Salvador earthquake

Adapted from Zezhong Zhang, Jean-Alain Fleurisson, Frederic Pellet, 2018. Numerical evidence of site effects contributing to triggering the Las Colinas landslide during the 2001 M_w=7.7 El Salvador earthquake. Landslides. DOI:10.1007/s10346-018-1040-y.

Les conditions géologiques et morphologiques locales d'un site spécifique peuvent être très complexes et donc augmenter l'intensité du mouvement du sol, et être à l'origine de glissements de terrain. La crête de Las Colinas au Salvador peut être un bon exemple de ce type de configuration, car sa géologie est complexe avec un ensemble formé de coulées pyroclastiques, de cendres brunes, de dépôts pyroclastiques tendres et d'un fin paléosol et il présente des pentes abruptes. Les mouvements de sol extrêmement élevés enregistrés à proximité du site lors du séisme du Salvador en 2001, sont supposés résulter d'effets de site, et être ainsi à l'origine du glissement de terrain catastrophique qui s'est produit.

Dans ce chapitre, afin de caractériser les amplifications du mouvement du sol dues aux effets de site, des études paramétriques portant sur les paramètres géométriques et géologiques du site ont été conduites avec un modèle de pente élastique linéaire, qui a été soumis verticalement une onde SV de type Gabor. Elle est destinée à étudier le rôle de chaque facteur, tel que la géologie de surface, l'angle de et la hauteur de la pente, sur l'amplification du mouvement du sol, et à évaluer la manière dont ils produisent l'amplification du mouvement du sol. Ensuite, une analyse dynamique sur le modèle de pente réel pour différentes grandeurs sismiques a été réalisée et une rupture de pente basée sur le déplacement a été créée pour évaluer la stabilité de la pente de Las Colinas.

4.1 Introduction

Landslides are one of the most devastating natural threats, as they cause property damage, land devastation, and fatal injuries and even adversely affect a variety of natural resources such as water supplies and forests (Crosta et al., 2005; Fan et al., 2012; Pellet et al., 2005; Yin et al., 2009). In particular, earthquake-induced landslides have been widely reported because they occur frequently and are extremely destructive (Jibson et al., 2004; Khazai and Sitar, 2004). Along with earthquake source and path effects, site effects often play an important role in triggering seismic landslides (Assimaki et al., 2005; Lenti and Martino, 2012; Meunier et al., 2008). Therefore, field investigations and experimental studies that consider seismic damage related to local site conditions are often conducted after earthquakes (Bertrand et al., 2011; Hough et al., 2010b; Tsai and Huang, 2000; Wald et al., 1991; Yin et al., 2009).

In most cases, site effects have been considered to explain the high accelerations recorded by field instruments. As a typical example, during the 1994 Northridge earthquake, a very high horizontal acceleration peak of 1.58 g was recorded by an analogue accelerometer installed at a ridge near the Pacoima Dam, while the peak accelerations recorded by nearby accelerographs in surrounding areas

were less than 0.5 g (Sepúlveda et al., 2005). Generally, site effects are assessed by using traditional theoretical methods that consider models that separately analyse simple topographic or geological configurations. Such methods often underestimate the effect of seismic waves propagating through complex geometry and do not consider interactions between the geometrical and geological effects on the frequency content of the input signal. For a given frequency range, these interactions may induce extremely high ground motion amplifications. There is clear instrumental evidence that site surface features have a considerable influence on the amplitude with respect to the frequency characteristics of shaking (Faccioli, 1991; Geli et al., 1988).

Ground motion amplifications at specific sites, with spatial geometries such as slope, ridge, hill and basin or geological settings such as strata and structural faults, have been modelled in many papers by using numerical simulations (Fleurisson and Bourdeau, 2006; Geli et al., 1988; LeBrun et al., 1999; Paolucci, 2002; Sánchez-Sesma and Campillo, 1991) but the results often underestimate the field observations or measurements. Previous studies (Bard, 1995; Del Gaudio and Wasowski, 2007, 2011; Semblat et al., 2002; Semblat and Pecker, 2009) have pointed out that subsurface geology, surface deposits, three-dimensional (3D) geometry, wave-field incident angle and orientation play important roles in ground motion amplification. Therefore, numerical predictions from a simplified topographic model usually underestimate the field observations. Moreover, the quantitative prediction of acceleration amplification is also difficult due to the complexity of the physical phenomena of wave diffraction associated with a combination of topographic and geological effects.

The focus of this paper is on evaluating site effects in the context of a landslide (Figure 4.1) triggered by the 2001 M_w=7.7 earthquake in El Salvador. In 2001, on January 13 and February 13, two earthquakes struck El Salvador with magnitudes of M_w=7.7 and M_w=6.6, respectively, and caused more than 1000 casualties due to earthquake-induced landslides (Bommer and Rodríguez 2002; Jibson et al. 2004). As a consequence, slope stability has been a problem of major concern in El Salvador (Crosta et al., 2005; Jibson et al., 2004; Konagai et al., 2002). According to earthquake disaster investigations (Jibson and Crone, 2001), evidence of slope movement, including trees shearing off the slope, boulders dislodging from their positions and deep fissures forming along the slope top edges, indicate that extremely strong ground motion occurred at the ridge. During the 2001 M_w=7.7 earthquake in El Salvador, a high horizontal acceleration peak greater than 0.7 g (Figure 4.2) was recorded by a nearby analogue accelerograph installed at Santa Tecla. 0.7 g is a very high level of acceleration that occurred farther than 100 km from the epicenter; however, it appears that shaking at the Las Colinas slope top was greater. This extremely strong shaking, resulting from the presence of the steep slope and thick, loose to poorly consolidated, and weak pyroclastic deposits, was the main contributing factor that triggered the Las Colinas landslide.

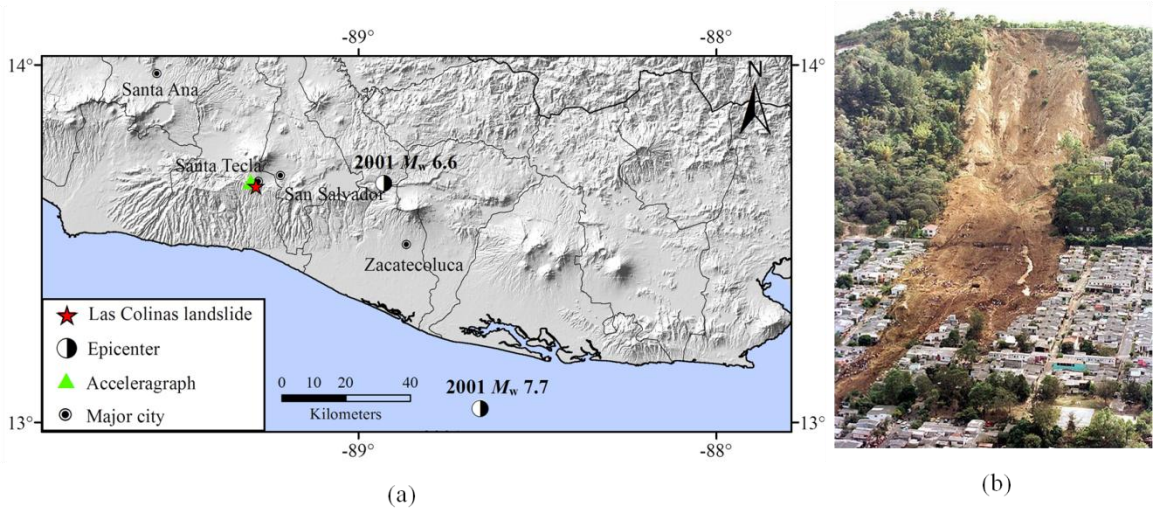


Figure 4.1: (a) Map showing the location of the Las Colinas landslide and epicentre of the 2001 earthquakes on January 13 and February 13 in El Salvador; (b) a photograph by the United States Geological Survey (USGS) showing the Las Colinas landslide (triggered by the January 13, 2001, M_w=7.7 El Salvador earthquake) that induced long-range movement.

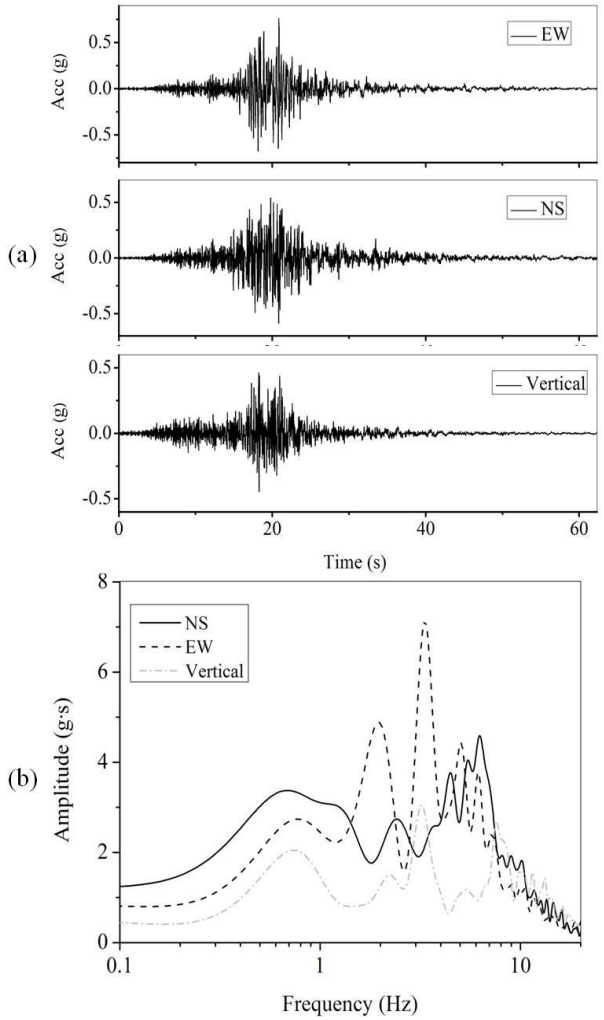


Figure 4.2: Observed accelerations (a) at Santa Tecla Station, and the corresponding FFT spectra (b).

In this paper, the Las Colinas landslide is analysed and site effects are shown to be the main reasons for triggering the landslide. Numerical simulations were performed on various 2D slope geometries and geological layers, and analyses of the seismic response were conducted to estimate the effects of topography and geology on the ground motion amplifications. The purpose of the parametric analysis is to understand the role of the geological layer, slope angle, and slope height on the ground motion amplification and then to estimate if site amplification is responsible for the triggering of the landslide.

4.2 Characterization of the Las Colinas landslide in El Salvador

El Salvador, located in Central America, is part of a circum-Pacific belt of volcanic and earthquake activity, characterized by rough topography and high seismicity that often triggers landslides (Bommer and Rodríguez, 2002). The largest earthquake of the 20th century was produced in this country on 7 September 1915, with a magnitude of Ms 7.8 and a source depth between 45 and 60 km (Ambraseys and Adams, 2001). Earthquakes that affect El Salvador are generally produced from two main sources of seismicity. The first source of seismicity affecting El Salvador is the Benioff–Wadati zone of the subducted Cocos plate, due to the convergence with the Caribbean plate in the Middle America Trench at an estimated rate of 7 cm/year (Dewey and Suárez, 1991). Another source of seismicity that can affect El Salvador is a zone of upper-crustal seismically active faults extending across the country from west to east. As a result of their shallow source and their proximity to main population centres, these earthquakes have induced considerable destruction in El Salvador, more than that caused by earthquakes in the subduction zone (White and Harlow, 1993).

The Las Colinas landslide, a rapid earth flow, occurred on a slope with a height of approximately 160 m. The total volume of landslide material was 250,000 m^3, which travelled approximately 700-800 m downhill from the landslide source. A scarp formed approximately 20 m behind the crest of the slope and developed with a very steep slope angle of approximately 32 ° in the upper half of the oblique free surface (see Figure 4.3). Two types of volcanic materials, including soft, weak pyroclastic deposits and stronger volcanic cinders (Jibson and Crone, 2001), are broadly distributed and present in the areas where landslides occurred during the January 2001 El Salvador earthquake. Numerous landslides are produced in sites with pyroclastic deposits, which are highly prone to sliding. The harder volcanic cinders also produced landslides because they primarily consist of boulders that easily dislodge from steep outcrops and roll down steep slopes (Jibson and Crone, 2001). A thin buried layer of palaeosol with weak cohesion, considerably prone to slip, is presented as a buried layer of volcanic cinder. Ground motion amplification generally occurs since the presence of these weak geological layers results in trapped seismic waves, which promotes landslide triggering.

4.3 Methodology

To characterize ground motion amplification due to potential site effects on the Las Colinas slope, a series of numerical simulations were performed using the finite difference code FLAC8.0 (Itasca, 2016); several groups of models were investigated with varying model geometry and geology subjected to seismic input motion with different central frequencies or cycles. Since this slope can be regarded as infinite in the direction perpendicular to the landslides, all the models were analysed in 2D for simplification. A linear elastic soil constitutive model is employed in numerical simulation.

Therefore, the model is valid to mimic continuous and homogeneous materials that show the linear stress-strain relationship (Bouckovalas and Papadimitriou, 2005). The detailed material properties are presented in Table 1. The typical slope model geometries used in the numerical analyses are shown in Figure 4.3.

A good knowledge of the detailed topography and underground structure in the Las Colinas area was acquired through field surveys and in-situ testing. A survey on slope topographic description at site was conducted with a laser-based theodolite (Laser Ace 300) by (Konagai et al., 2002) in 2001. In addition, a geotechnical investigation started with 12 drills to depths ranging between 33 m and 90 m. Then standard penetration tests (SPT) and additional in-situ field tests were performed in June 2001 to determine the underground structure. Laboratory testing and field soil testing, including SPT, direct shear test, downhole seismic velocity, unconsolidated triaxial test, were conducted to determine the material properties (Lotti and Associati, 2001). Mechanical properties of the soils at the site are presented in Bourdeau's dissertation (Bourdeau, 2005)

Table 4.1: Material properties used in the numerical simulations (Bourdeau, 2005)

	Density (kg/m^3)	Young's modulus (MPa)	Shear wave velocity (m/s)	Cohesion (KPa)	Angle of friction (^{o})	Poisson's ratio
Pyroclastic flows	1900	5793	1100	200	60-80	0.26
Brown cinders	1530	1322	570	30-40	30-33	0.33
Palaeosol	1760	1521	570	5-10	20-24	0.33
Pyroclastic deposit	1500	62	120	60-80	30-35	0.43

Two groups of homogeneous models, composed of brown cinders, with varying slope angles and slope heights were designed to isolate and assess the topographic effect on ground motion amplifications. In the first group of models, the slope angle varies from 25 ° to 60 ° with an interval of 5 ° whereas the other geometrical parameters do not change. In the second group of models, six models of different slope heights, h=40 m, 60 m, 80 m, 100 m, 120 m and 150 m, were built to evaluate the effect of slope height on ground motion amplification. The original model has a height of 160 m, and the other models are created by varying the vertical distance between the crest and slope toe. To this end, the slope toe (left side of the model in Figure 4.3c) was raised while the actual slope geometry kept in place.

The effects of low-velocity surface layers were evaluated on 4 different profiles for different combinations of geological layers. The first model profile corresponds to a homogeneous geological model that is composed of pyroclastic flows with a shear wave velocity of 1100 m/s. The second model is composed of pyroclastics flows and brown cinders. The geometry of this model is the same as the real slope (see Figure 4.3a), but the layers of pyroclastic fall deposits and palaeosol were replaced by brown cinders. The third model was composed of pyroclastic flows, brown cinders and pyroclastic fall deposits, and this model was used to evaluate the role of the thick pyroclastic fall deposit. The last model, with the same geometrical and geological conditions as the natural slope, was built to assess the effect of the approximately 1.5 m thick layer of palaeosol on the ground motion amplification.

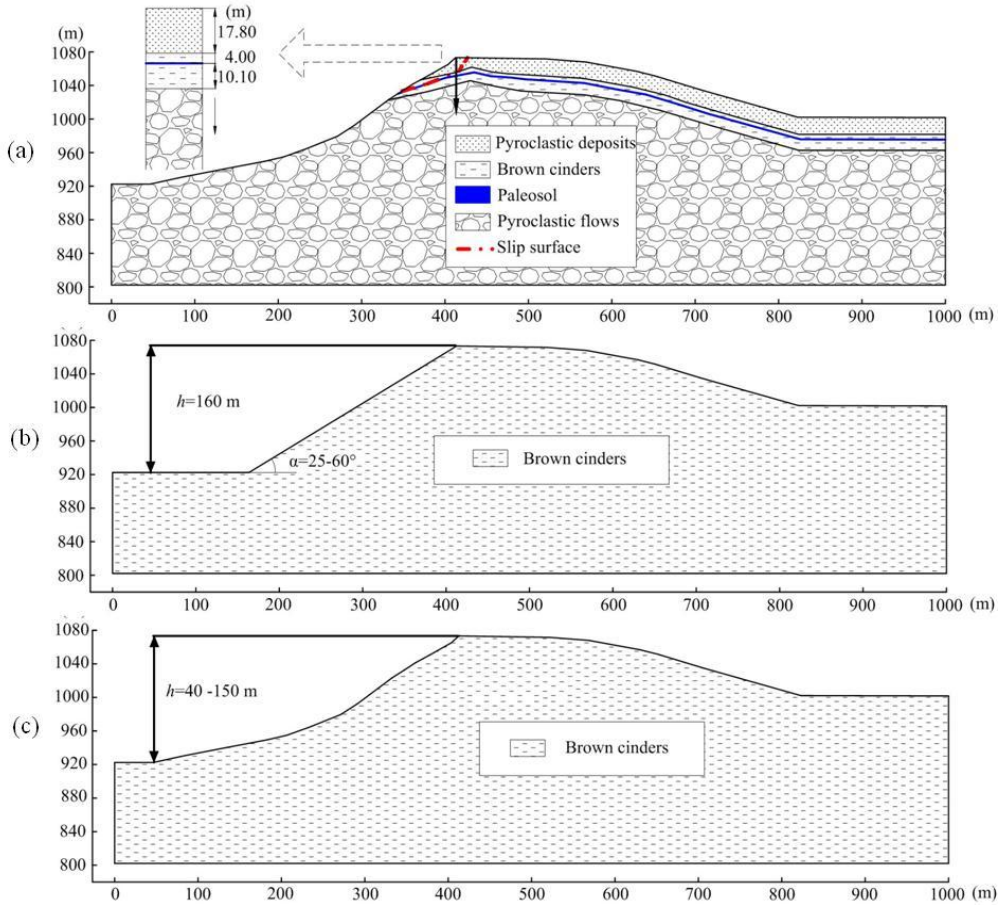


Figure 4.3: The 3 groups of slope models that were numerically simulated. (a) Actual slope model; (b) model with varying slope angle; and (c) model with varying slope height.

To avoid the multiple frequency signal effects of seismic inputs, a single-frequency Gabor wavelet with a peak ground acceleration (PGA) of 0.5 m s^{-2} and 6 cycles was applied at the base of the slope model as a vertical SV wave. The acceleration time history $a(t)$ is given by Equation 1.

$$a(t) = \sqrt{\alpha e^{-\beta t} t^{\gamma}} \sin(2f\pi t) \quad (1)$$

Where f is the central frequency of the signal; t is time; and α, β and γ are parameters controlling the shape of the acceleration time history. The corresponding details are listed in Table 2.

To determine the central frequency of the input motion, a 15 s time history window of the real seismic recorded at Santa Tecla station was applied to the homogeneous model and the model with the observed geometrical and geological conditions. Then, the observed horizontal accelerations at the crest of these two models were analysed with the fast Fourier transform method. The results are shown in Figure 4 4. Three peaks at 1-2 Hz, 4-5 Hz and 6-8 Hz are observed. To constrain the wavelength lower than the slope height, 7 Hz is selected to be the central frequency of input motion.

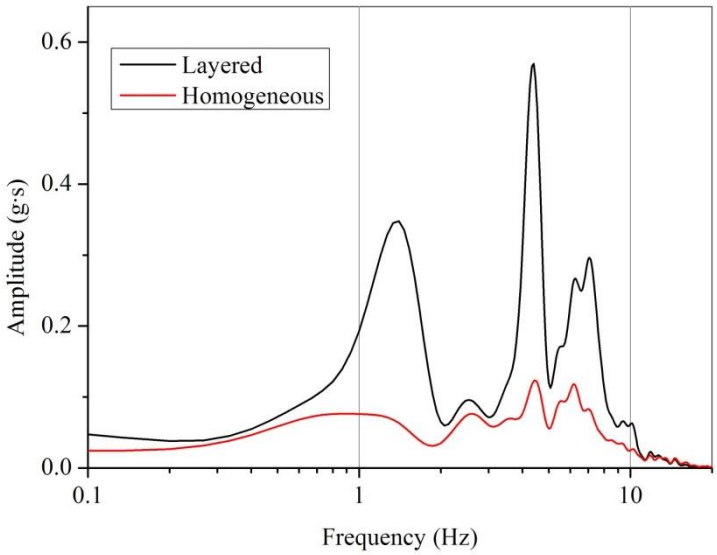


Figure 4.4: The spectra of the horizontal accelerations obtained from the numerical analyses of the homogenous and layered models subjected to windowed seismic waves.

Table 4.2: Parameters for controlling the number of cycles

Number of cycles	**1**	**2**	**4**	**6**	**12**
α	2,800,000	63,000	3,100	200	6.5
β	35	35	12	7	3.5
γ	5.7	5	5	5	5

In addition, seismic input with different central frequencies varying from 1 Hz to 10 Hz and cycles *N*=1, 2, 4, 6 and 12 was applied to a model with the same geometrical and geological conditions as the actual slope to analyse the effect of seismic input motion on ground motion amplifications.

According to Kuhlemeyer and Lysmer (Kuhlemeyer and Lysmer, 1973), the size of the elements should be smaller than approximately one-tenth to one-eighth of the wavelength associated with the highest frequency component of the input wave to ensure accurate representation of wave transmission through a model. In present analyses, the highest frequency of input motion is 10 Hz and the shear wave velocity of the softest material (Pyroclastic deposit) is 120 m/s. Consequently, the element size for this material should be less than 1.2 m. Similarly, the element size in the material of Pyroclastic flows should be less than 11 m. In fact, elements size in Pyroclastic deposit are less than 1 m, in Pyroclastic flows less than 5 m and those in the other materials are assigned a size smaller than 3 m.

To prevent the reflection of outwardly propagating waves back into the model, quiet boundaries were applied as absorbing boundaries at the base of the models. Quiet boundaries were proposed by Lysmer and Kuhlemeyer (Lysmer, 1969) and are created by adding normal and tangential dampers at the base of the model so that the incident wave is absorbed at the base and cannot return inside the model. The solution of quiet boundaries is an effective way to simulate a half-space boundary. The attached dashpots provide viscous normal and tangential tensions that are given by the following equations:

$$t_n = -\rho C_P v_n \quad (2)$$

$$t_s = -\rho C_S v_s \quad (3)$$

Where v_n and v_s represent the normal and tangential components of the velocity at the boundary; ρ is the mass density; and C_P and C_S are the P and S wave velocities respectively.

Additionally, free-field boundaries were applied as lateral boundaries with the purpose to prevent artificial wave reflection. The system uses dampers attached to grids of the lateral vertical boundaries of the model to simulate the conditions of a half-space. The free-field boundary consists of a one-dimensional (1D) free-field grid, simulating the behaviour of a full-space model. These free-field grids supply conditions that coincide with those in the infinitely extended medium; thus, laterally propagating plane waves suffer no distortion at the boundary. In fact, the lateral boundaries allow the free-field grids to be attached to the main grids with viscous dashpots to prevent wave reflection as the quiet boundary. The accuracy of numerical analyses that use absorbing boundaries has been verified, and numerical results are in good agreement with analytical predictions (Bouckovalas and Papadimitriou, 2005).

Rayleigh damping is used to account for energy dissipation. The damping equation is given by a matrix equation (Itasca 2016), which includes the mass (M) and the stiffness (K) matrices:

$$C=\alpha M+\beta K \tag{4}$$

Where α is the proportional constant of the mass matrix and β is the proportional constant of the stiffness matrix. Equation (4) will reach minimum damping when the minimum critical damping (ξ_{min}) and the minimum frequency (ω_{min}) are described by the following equations:

$$\xi_{min}=(\alpha\beta)^{1/2} \tag{5}$$

$$\omega_{min}=(\alpha/\beta)^{1/2} \tag{6}$$

Rayleigh damping, applied in numerical modelling to absorb wave energy, is frequency-dependent. To achieve an approximately frequency-independent response within a limited frequency range, it is necessary to select the appropriate damping ratio and central frequency parameters. In the current study, a minimum damping ratio of 0.5% was set for the entire model to prevent indefinite oscillations. The frequency of the seismic input motion was selected as the central frequency.

Finally, the amplification factor was computed as the ratio between the peak horizontal acceleration (the absolute value) obtained at a given point of the 2D model and that observed on the ground surface of a corresponding 1D model. The 1D model was built with the same material and the same depth from the slope crest to the base of the corresponding 2D model. It should be noted that the material of the 1D model is the same as the bedrock of the multi-layer 2D model.

4.4 Analysis of the results

4.4.1 Effects of slope angle

Figure 4.5 shows the distribution of the peak horizontal ground motion amplification behind the crest in the time domain for the Gabor wavelet with a central frequency of 7 Hz. It is observed that slope angle has a significant influence on ground motion amplification.

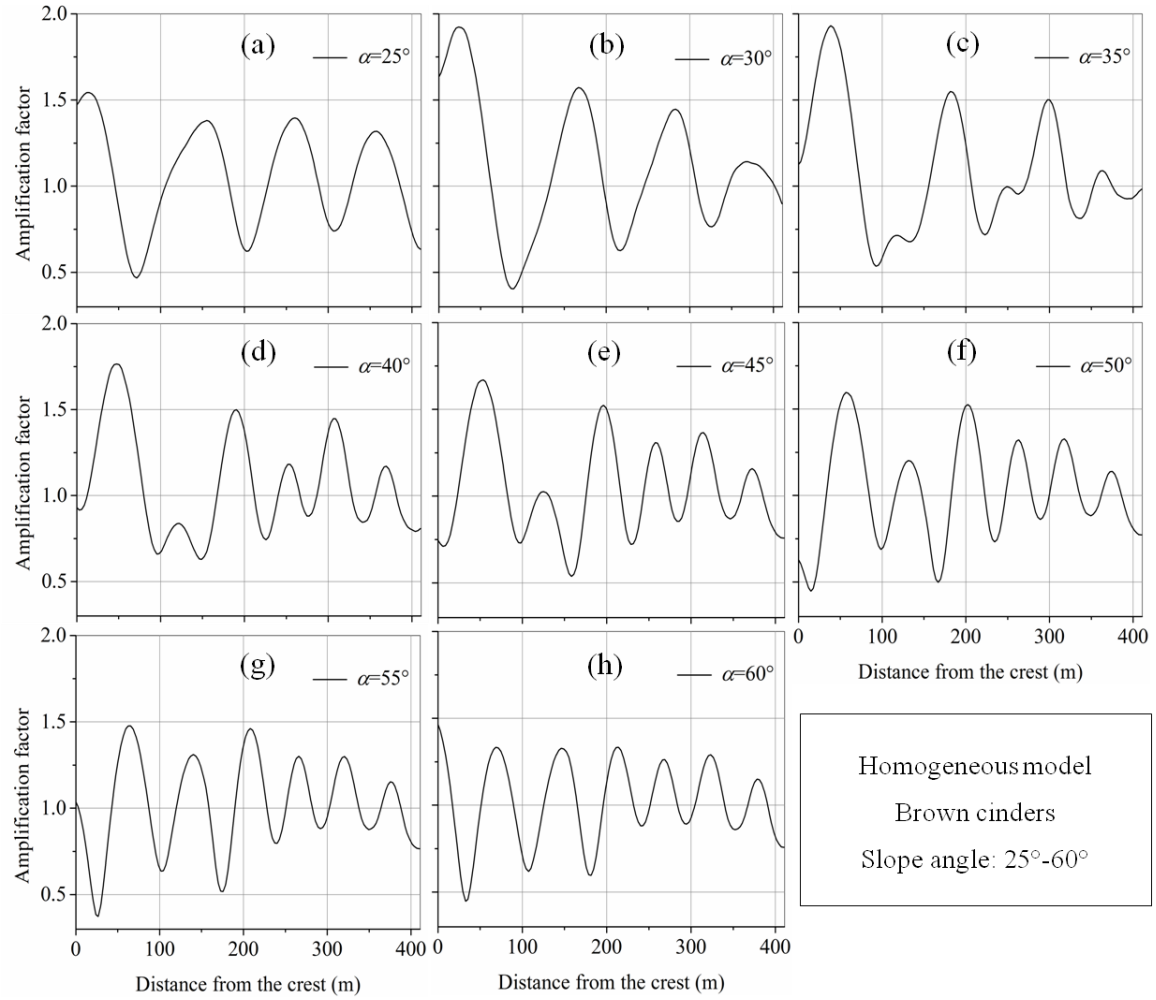


Figure 4.5: Horizontal peak ground motion maximum amplification as a function of distance from the crest (x=0 corresponds the crest). (a)-(h) Results from numerical analyses for the slope model with varying slope angles from 25 ° to 60 °.

It can be seen that a maximum ground motion amplification of 1.93 is obtained for a slope angle of 35 °. Actually, the critical angle at which the reflected P waves which hit the oblique surface achieve maximum amplitude, is 32.3 °. This critical angle can be derived from the following equations (Achenbach, 2012):

$$\theta_0=\theta_1, \text{ and} \tag{7}$$

$$\sin\ \theta_0=k^{-1}\sin\ \theta_2, \tag{8}$$

where k is the material constant defined by the ratio between the P wave velocity and SV wave velocity, here k=1.985, θ_0 is the incident angle of the SV wave (see Figure 4.6), and θ_1 is the reflected angle of the P wave. The amplitude of reflected P waves can be given by the following equation (Achenbach, 2012):

$$A_1 = -A_0 \frac{ksin4\theta_0}{sin2\theta_0 sin2\theta_2 + k^2 cos^2 2\theta_0} \tag{9}$$

where A_0 is the amplitude of incident SV waves, A_1 is the amplitude of reflected P waves. It can be derived from equation 9, as long as the slope angle remains above 32.3 °, the amplitudes of reflected

P waves approach zero. This is because when the slope angle is greater than 32.3 °, the reflected P waves transform into surface waves propagating along the free surface (Achenbach, 2012).

When the slope angle increases, the location of the largest ground motion amplification (the value of the highest peak in the curve of the ground motion amplification factor) shifts away from the crest. For a slope angle of 30 °, the largest ground motion amplification is observed approximately 20 m from the crest. This coincides with the location where the landslide initiated. The real slope has a slope angle between 30 ° and 35 ° near the crest, which contributed to the extremely high value of ground motion acceleration. In particular, the landslide movement initiated at the location where the maximum ground motion amplification occurred, showing that slope angle is an important factor of landslide triggering.

The ground motion amplification is caused by superposition of the diffracted Rayleigh waves, reflected P waves and incoming SV waves (Figure 4.6). This allows amplification and deamplificaion to alternate on the ground surface. From Figure 4.5, it can also be seen that the ground motion amplifications vary approximately equally in amplification and deamplification.

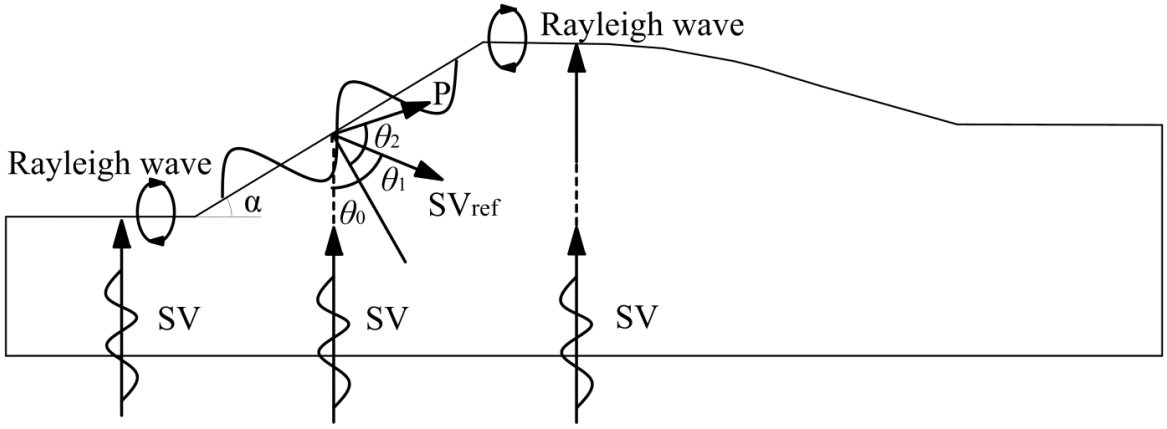


Figure 4.6: Illustration of wave propagation, reflection, diffraction and superposition.

Secondary amplification peaks can also be observed for slope angles steeper than 35 °, and they increase with the slope angle. This is because the reflected P waves transform into surface waves and propagate along the ground surface when the slope angle is greater than 32.3 °. This allows the occurrence of complex interference of Rayleigh waves, SV waves and the surface waves, which are transformed from P waves.

4.4.2 Effects of slope height

Figure 4.7 shows the peak amplification factors of horizontal accelerations on the ground surface behind the crest, normalized by the corresponding free-field acceleration (computed from the 1D model). Generally, the values of maximum amplification vary between 1.4 and 1.8 and depending on the slope height. Figure 4.7 also shows alternation between the amplification and deamplification and several successive peaks of amplification. The amplification increases with increasing slope height; in particular, the primary peak clearly increases.

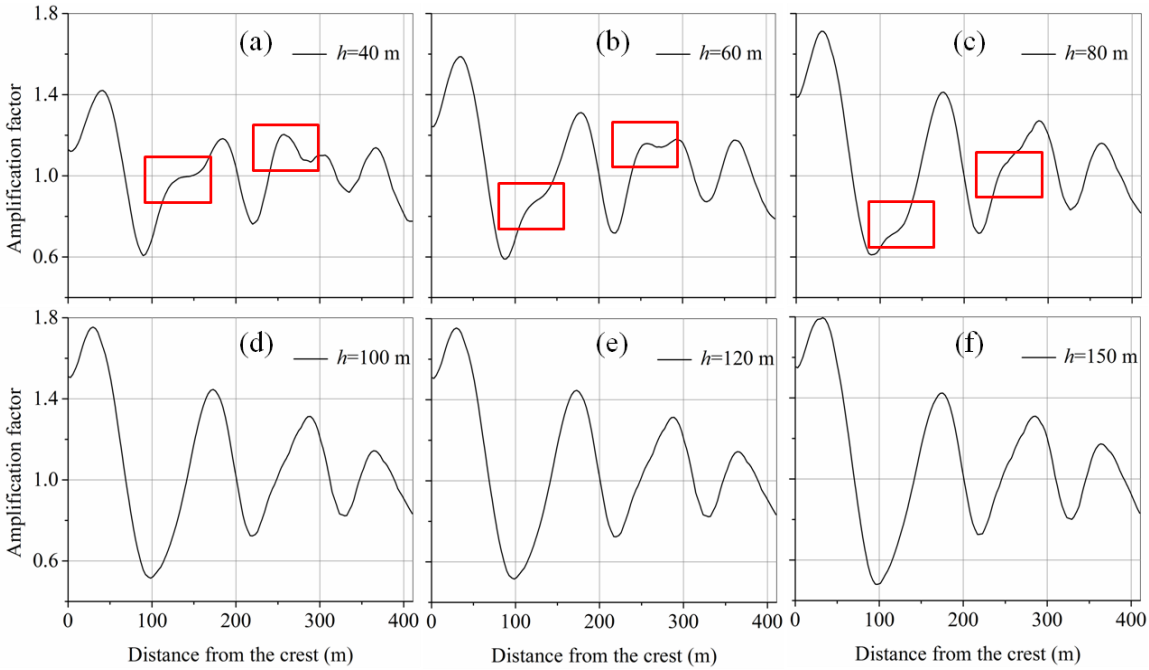


Figure 4.7: Peak ground motion amplification as a function of the distance from the crest. (a)-(f) Results from numerical analyses of the slope model with varying slope heights ranging from 40 m to 150 m. The red frame encloses the secondary peak.

The slope height could have an influence on the location where amplification or deamplification occurs depending on the ratio between the slope height and the wavelength. For the wavelength lower than the slope height (e.g. h=40 m, 60 m or 80 m), the wave scattering at the slope occurs, resulting in a modified wave field at the slope surface, which possibly causes that the location where the largest amplification is observed to move slightly closer to the crest with increasing slope height. This is also the cause why the secondary peaks are produced for models with a slope height of 40 m, 60 m or 80 m.

4.4.3 Effects of surface geology

Figure 4.8 gives the results of the numerical simulations of the 4 models for different geological compositions. It can be seen that much larger amplifications are observed in Figure 4.8(c) and (d), showing that the additional ground motion amplification due to the pyroclastic fall deposit is relatively large compared to the amplification caused by only topography (Figure 4.8a) and a layer of brown cinder (Figure 4.8b). In contrast to Figure 4.8(c), in Figure4.8(d) no obvious difference is found. This indicates that the palaeosol layer with a thickness of approximately 1.5 m has nearly no influence on the ground motion amplification, as it has the same shear wave velocity as the brown cinder layer. Compared to Figure 4.8(a), Figure 4.8(b) shows the same trend in amplification factor with a slight increase in magnitude.

The high amplification factors in Figure 4.8c and 4.8d result from the presence of a pyroclastic fall deposit with very low shear velocity at the surface. The geological effect is thus likely to be responsible for triggering the landslide, considering that extreme ground motion is the primary factor of landslide triggering.

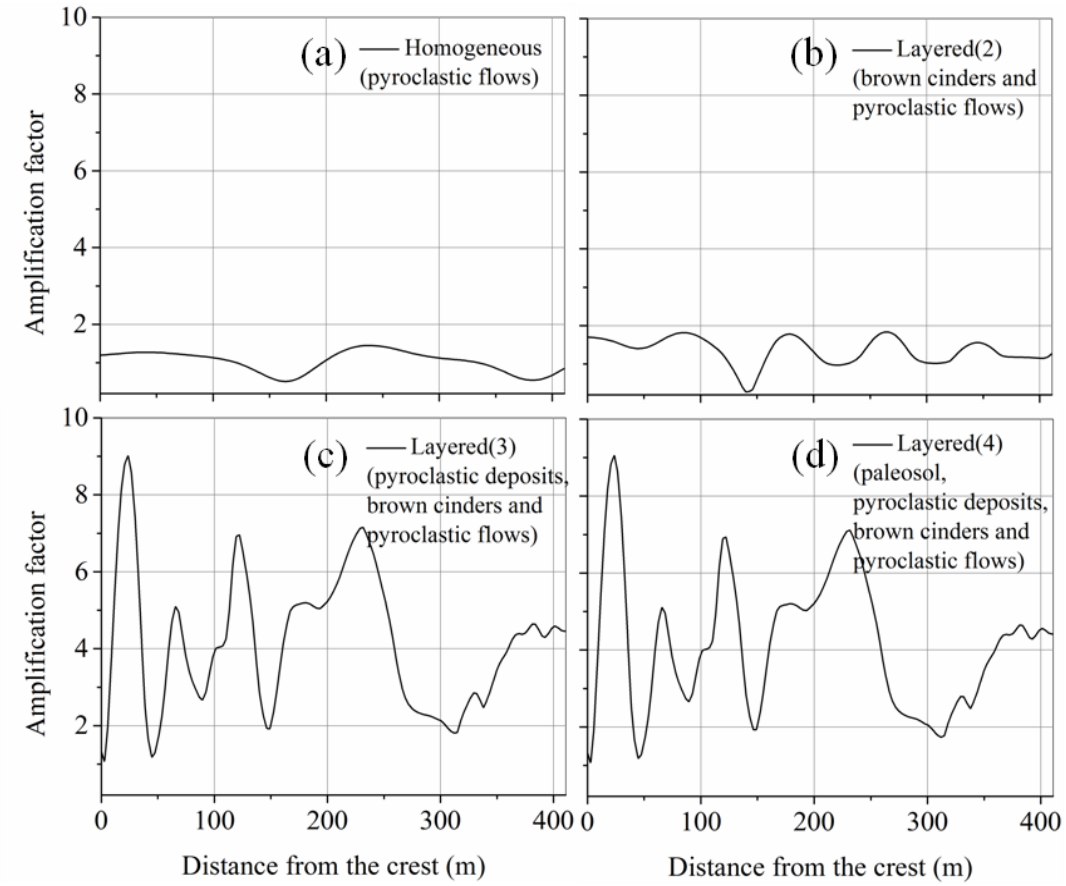


Figure 4.8: Amplification factor as a function of the distance from the crest of four slope models with different geological compositions. (a) Homogenous model; (b) the model in Figure 4.3(a) with brown cinders in place of palaeosol and pyroclastic fall deposits; (c) the model in Figure 4.3(a) with brown cinders in place of palaeosol; and (d) the model in Figure 4.3(a).

4.4.4 Effects of input motion frequency

Figure 4.9 displays the maximum ground motion amplification along the ground surface behind the crest of the model that corresponds to the actual geological and geomorphological slope conditions, subjected to Gabor wavelets with different central frequencies.

It can be observed that the ground motion amplifications due to wave interference are strongly frequency-dependent. First, Rayleigh waves that contribute to ground motion amplification are produced by wave diffraction at the geological or structural surface. The amplitude of the generated Rayleigh waves is affected by the relationship between the model size and the wavelength (frequency) of incoming waves. Second, trapped SV waves and reflected P waves in the soil layers repeatedly interfere and therefore contribute to higher wave amplitudes due to constructive or destructive interference. Without considering the thickness of the soil layer, the interference of trapped waves is also affected by the frequency (wavelength) content of the seismic input motion.

In general, when a model is subjected to input motion of a low central frequency, the ground motion amplification is relatively small compared to those obtained when applying high-frequency input motion. When subjected to input motion with a central frequency of 3 Hz, the maximum amplification factor is less than 3, while the ground motion amplification reaches 9 when the input motion as a central frequency of 7 Hz. From Figure 4.9, it can also be observed that the maximum ground motion amplifications are located far from the crest when the central frequency of the input

motion is 1 Hz, 2 Hz, 4 Hz, 8 Hz and 10 Hz; however, the maximum ground motion amplifications of the other central frequency values are located close to the crest or at the crest. In particular, the maximum value of amplification obtained with an input motion central frequency of 7 Hz is located approximately 20 m from the crest where the landslide occurred. These results demonstrate that the frequency content of input motion can also significantly affect the amplitude of ground motion amplification and determine the location of occurrence of the maximum values of amplification.

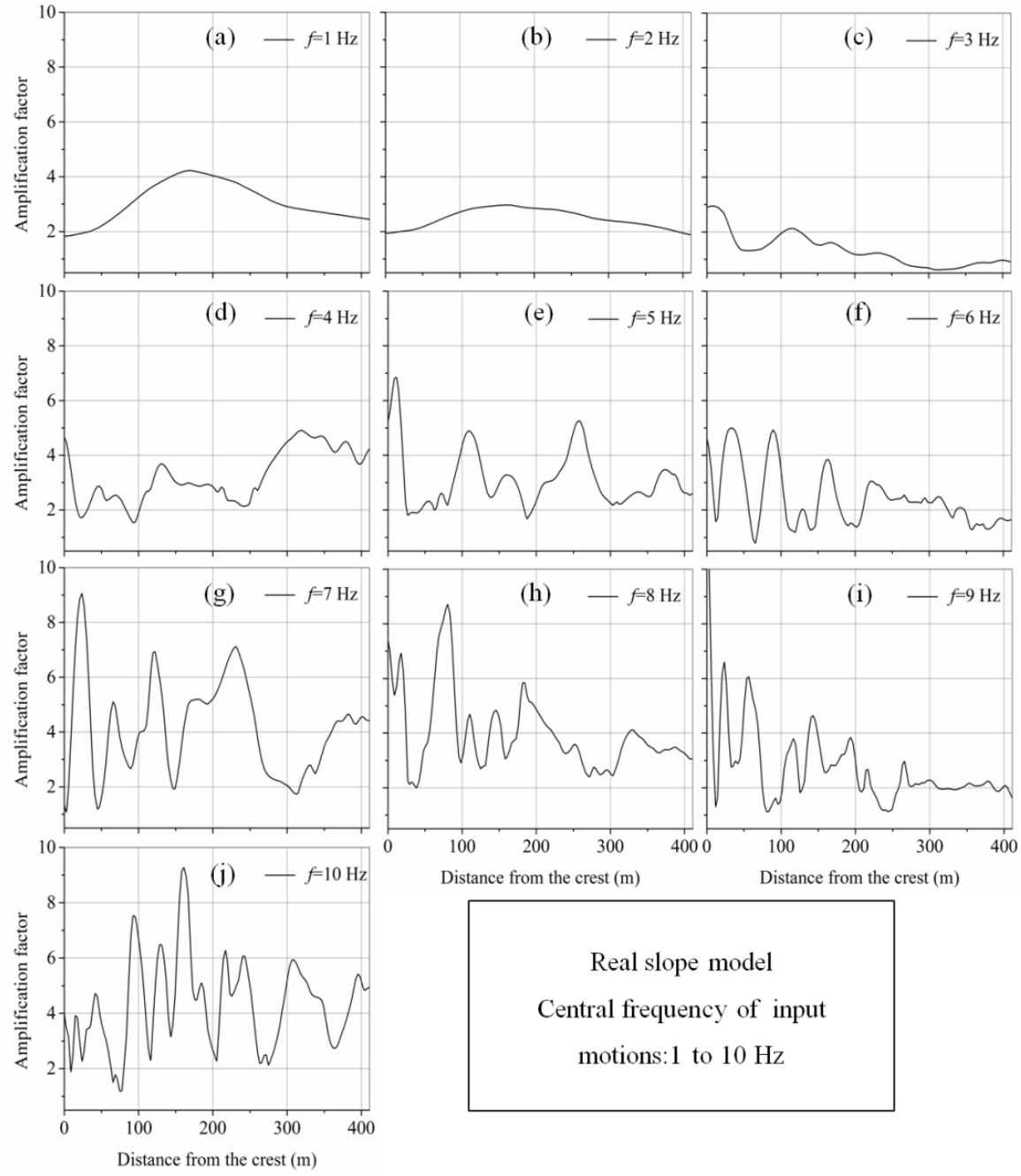


Figure 4.9: Distribution of peak ground motion amplification along the ground surface behind the crest of the model in Figure 4.3(a), subjected to a Gabor wavelet with a varying central frequency from 1 Hz to 10 Hz.

4.4.5 Effects of the number of cycles of the input motion

Earthquake magnitude has been reported to strongly increase with earthquake duration, which is one of the most important features of earthquake waves (Castello et al., 2007; Kempton and Stewart, 2006). The number of cycles determines the duration of input motion of univocal frequency. Therefore,

Gabor wavelets with different cycles were applied to the real slope model to assess the effect on the ground motion amplifications. The recorded ground motions are normalized by the reference ground motion obtained from the corresponding 1D model and are presented in Figure 4.10.

Figure 4.10 allows a comparison of amplification factors from simulations with different cycles of input motion. Figure 4.10 shows that the maximum amplification increases with the number of cycles of the input motion. For one cycle, the maximum amplification is less than 1.5, while the maximum amplification is approximately 2.3 when the number of cycles is 6. The secondary peaks of the curves of ground motion amplification significantly increase with the number of cycles. Therefore, longer duration of motion (more cycles) is much more prone to induce a greater amplification.

The acceleration time history (Figure 4.2) recorded by the nearest accelerograph lasted longer than 62 s. Therefore, the number of cycles in this recorded acceleration is enough large to produce high ground motion amplification, and this long duration aggravates landslide triggering.

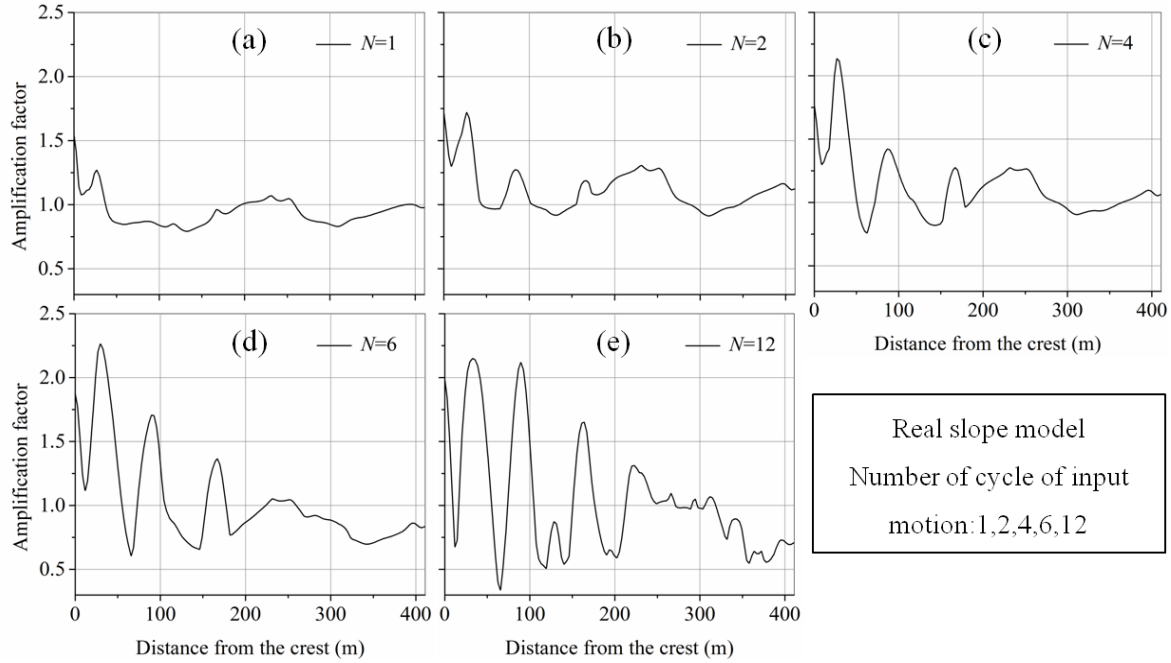


Figure 4.10: Distribution of peak ground motion amplification along the ground surface behind the crest in the model of Figure 4.3(a), subjected to a Gabor wavelet with varying cycles of 1, 2, 4, 6 and 12.

4.4.6 Effects of ground motion magnitude on slope stability

The above analyses show that slope geometry and surficial layer considerably amplify the ground motions near the crest. To provide evidence that increased magnitude due to site effects have possibly induced the landslide, a stability analysis of the Las Colinas slope was performed based on the detailed description of the geography, geological layers, soil properties and available earthquake recordings. The Mohr-Coulomb constitutive model was used for all zones of the slope.

However, a static analysis was first carried out using the strength reduction method for calculating the factor of safety (FOS) of the actual slope model and thus to assess pre-earthquake slope stability. A FOS of 1.46 was obtained for static analysis, which shows that the slope would have been stable, if not because of the ground shaking. It is, therefore, necessary to perform dynamic analysis for the slope model in order to evaluate effects of ground motion magnitude on slope stability, in particular with regard to the high amplification at the Las Colinas slope.

The Las Colinas slope should fail when subjected to the actual ground motion for dynamic analysis. Therefore, for comparison purpose, the earthquake recordings with reduced amplitudes (e.g. PGA=0.1 g, 0.2 g and 0.3 g) and the original amplitude were applied as input motions at the base of slope model for the dynamic analysis. Horizontal displacement distribution (Figure 4.11) was obtained for the real slope model. To analyse the results, a simple slope failure criterion related to horizontal displacement is made. As slip surface is also plotted in Figure 4.11(d), it can be seen that the slope failure behind the crest occurred where horizontal displacement is between 1 and 1.5 m. Horizontal displacement larger than 1 m is therefore used as an indication of slope failure in the present study.

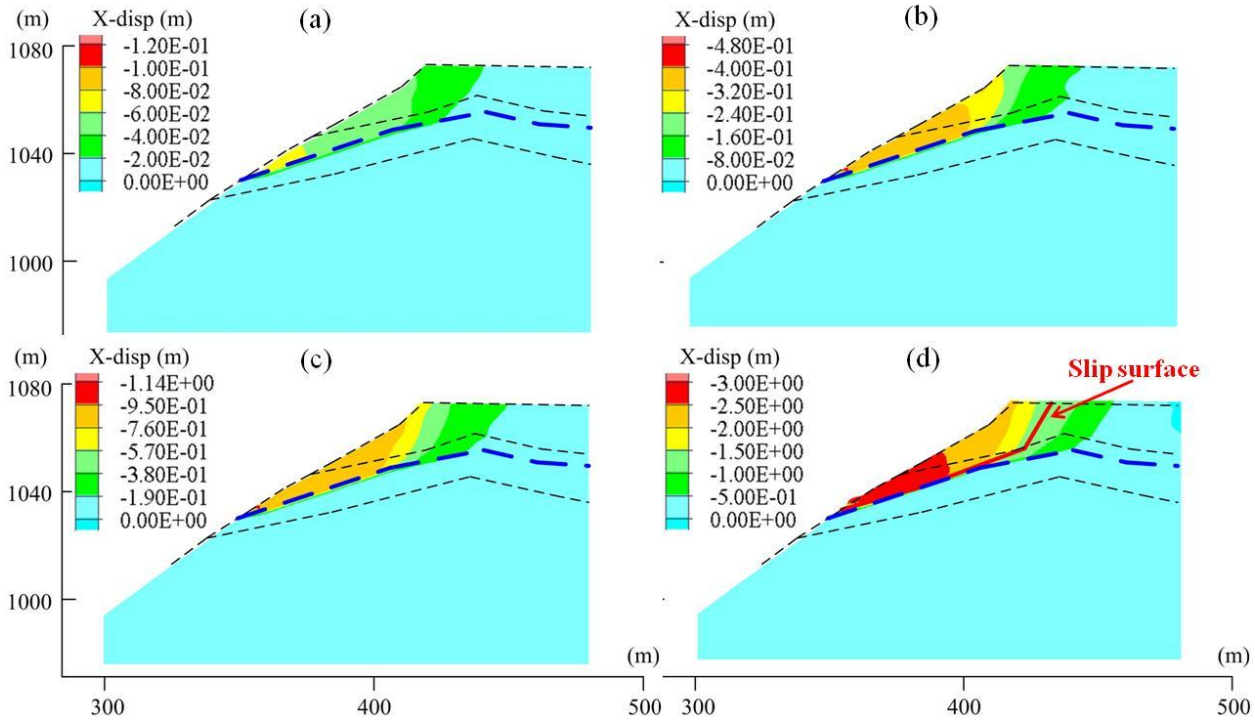


Figure 4.11: Horizontal displacement distribution in the real slope model subjected input motion with different peak ground accelerations. (a) PGA=0.1 g; (b) PGA=0.2 g; (c) PGA=0.3 g; (d) PGA equals to the original amplitude.

Figure 4.11 shows a comparison of the horizontal displacement distribution in the real slope model subjected to input motions with different PGAs. It can be observed that with the increase of PGA the horizontal displacement near the slope crest significantly increases. When exerting the original ground motion acceleration, the maximum horizontal displacement reaches 3 m. However, when reducing the PGA of input motion to 0.1g, the horizontal displacement near the crest turns very small (<0.04 m), which indicates that the slope is still stable when subjected to a relatively low shaking (e.g. PGA=0.1 and 0.2 g). According to the previous analyses, the ground motion amplification factor can reach 9. Therefore, although subjected to the input motion with a low magnitude, the observed acceleration near the crest should be much stronger (due to site effect) than the ground motion recorded at the Santa Tecla Station. Consequently, it is proved that site amplification contributed to the triggering of the Las Colinas landslide.

The maximum horizontal displacement larger than 1 m occurs in the layer of weak paleosoil when subjected to the input motion with PGA=0.3 g, showing the slope movement starts to develop in the weak soil layer. In addition, the maximum horizontal displacement always occurs in the layer of weak paleosoil and increases with the increase of ground motion magnitude. It shows that the weak palaeosol layer plays a significant role in enhancing the slope sliding.

4.5 Conclusions

Numerical modelling was conducted to evaluate factors that may have made possible to trigger the Las Colinas landslide induced by the 2001 M_w 7.7 earthquake in El Salvador. Parametric studies were performed with elastic models to characterize the ground motion amplifications due to site effects such as the slope angle, slope height, geological layers, frequency content and number of cycles of input motion. The results are expressed in terms of amplification factors along the ground surface and are clear evidence that site effects induce significant ground motion amplifications that are likely to trigger landslides.

The intensity of amplifications and the distribution of the amplifications along the ground surface (especially the location where the maximum amplification value occurs) significantly change with slope angle. The location of the calculated maximum amplification value for the model with a slope angle of 30 ° occurs at the same point where the real landslide initiated. The Las Colinas slope has a height of approximately 160 m, and height is another reason for triggering sliding movement because amplifications increase with slope height. The results clearly reveal that the geological amplifications are substantially larger than the amplifications due to topographic effects. In particular, the soft pyroclastic fall deposit located at the surface is responsible for the very high maximum amplification, which can reach a value of 9. The presence of a relatively thin palaeosol layer, without any significant effect on ground motion amplifications, enhances the ground movement because of its weak cohesion.

The frequency content of the input motion affects both the value of the amplification and location of the maximum ground motion amplification, depending on the comparative size between the wavelength of the input motion and the slope height or geological layer thickness. With an increasing number of cycles of input motion, the amplification values increase, and thus a longer earthquake is likely to enhance site effects.

Finally, results from dynamic analyses subjected to ground motions with different PGAs show that the higher PGA the larger horizontal displacement is produced near the slope crest. When exerting the input motion with a relatively low magnitude (e.g. PGA=0.1 and 0.2 g), the slope keeps stable although the observed acceleration on the ground surface is much stronger than the acceleration recorded at the Santa Tecla Station. Therefore, it is proved that site amplification contributed to the occurrence of the Las Colinas landslide.

Overall, numerical simulations provide results that reveal how site effects affect ground motion amplifications and thus promote the triggering of the landslide. However, the topographic effect associated with geological features shows a complex influence on the ground motion amplifications, resulting from complex wave propagation, reflection, diffraction and interference. In addition, the model simplicity neglects 3D effect, small-scale factors (if exist), material heterogeneity et al, which may lead to underestimate or overestimate ground motion amplification, in particular at high frequencies. To provide a better understanding of this landslide, it is necessary to perform more studies, which would take various conditions into consideration.

Chapter 5: Conclusions and Recommendations

5.1 Conclusions

This thesis describes topographic effect and soil amplification, focusing on investigating the interactions between topography and signal frequency that significantly affect ground motion response. Parametric studies were performed with elastic models in order to characterize the ground motion amplifications due to site effects such as the slope angle, slope height, surface geology, frequency content and number of cycles of the input signal. Furthermore, we analyzed the interaction between topography and ground movement amplification in the specific case of a ridge in Zigong city in China. Finally, we assessed site effects on the triggering of landslides in the case of Las Colinas in Salvador. The results of this research can be summarized as follows:

The parametric study suggests that the acceleration amplification factor is significantly affected by the slope angle, slope height, signal frequency and duration. The magnitude of the amplifications and the distribution of the maximum amplification along the ground surface behind the slope crest change with the slope angle. Slope height has also a significant effect on the magnitude of the acceleration amplification; however, it does not affect the distribution of the maximum amplification factor when the wavelength of the input signal is lower than the slope height.

The acceleration amplification factors along the ground surface behind the crest vary intensely around a value of 1 (in the range of 0.4-1.6) which means that acceleration along the surface of the slope alternates between amplification and de-amplification. The topographic effect on ground motion amplification significantly decreases with an increase of the distance to the crest and the amplification ratio is under 1.1 for all the studied cases when the distance from the crest is larger than 300 m.

The scattering, diffraction and mode conversion of seismic waves near the topographic feature gave rise to vertical accelerations; the acceleration amplification observed on the upper ground surface is primarily attributed to Rayleigh waves diffracted in the vicinity of the slope crest. The results also suggest that the maximum amplification does not necessarily occur at the crest and depends on the slope angle. The maximum amplification could be obtained at a short distance behind the crest and this distance increases with slope angle, when the slope angle is greater than 20 °. For instance, for slope angles equal to 25 ° and 45 °, the maximum acceleration amplifications were obtained at 5.7 m and 33 m behind the crest respectively.

The ratio between the slope height and the wavelength of the input signal can significantly affect not only the intensity of the amplification, but also the location where the largest amplification is observed.

The amplification values increase with the number of cycles of the input signal (duration), and secondary peaks appear in the curve of acceleration amplifications. The peak intensity also increases with the number of cycles of input motion.

The case study investigating site effects of the instrumented Xishan Park ridge in Zizhong (China), underlines that the amplification values change depending on the location of the monitoring station. The results reveal that site amplification is mainly observed at frequency ranges between 3 and 8 Hz and between 10 and 20 Hz, while the FFT spectra show that the signal energy is mainly distributed in a

frequency range between 1 and 6 Hz. The ground motion amplifications for the NS component are slightly higher than the corresponding ones for the EW component, which suggests a possible azimuthally dependence of site effects.

The simulated results are generally in good agreement with the recorded data, although the simulations reflect a slight overestimation at low frequencies and an underestimation at higher frequencies. Moreover, the "simulated" peaks of the spectral amplifications are almost lower than those derived from the field records in the time domain. Significant underestimation of the predicted amplification is observed at higher frequencies (f>3 Hz). The strong attenuation effect on the input motion at high frequency highlights the shortcoming that Rayleigh damping does not adequately represent the energy dissipation in the numerical simulations.

The observed discrepancies between the predicted amplifications and the field observations at high frequency can be attributed to small-scale or of near-surface geological conditions (e.g. presence of material with low seismic velocity).

Another numerical modelling related to the Las Colinas landslide in Salvador characterizes topographic geological site effects on ground motion amplifications. The results clearly reveal that the geological amplifications are substantially larger than the amplifications due to topographic effects. In particular, the soft pyroclastic deposit located at the surface is responsible for the very high level of amplification, which can reach a value of 9.

The results from dynamic analyses subjected to ground motions with different PGAs show that the higher the PGA, the larger horizontal displacements are produced near the slope crest. When exerting the input motion with a relatively low magnitude (e.g. PGA=0.1 g and 0.2 g), the slope remains stable although the observed acceleration on the ground surface is much stronger than the acceleration recorded at a nearby station. Therefore, it can be concluded that site amplifications contributed to the occurrence of the Las Colinas landslide.

5.2 Recommendations for further research

The research effort presented herein was mainly established by using simplified 2D numerical simulations, and the following fundamental recommendations should be made for the further research works:

To perform additional numerical simulations in order to complete the understanding of the fundamental mechanisms of topographic amplifications: the numerical models should include small-scale factors (e.g. the possible presence of soft material at the surface, intercalations and rock cracks in specific sites) which can cause unexpected ground motion amplifications at high frequency. It also should investigate sites with various topographic and geological conditions to better understand the ground motion response due to site effects.

To carry out 3D simulations in order to validate the model simplification and analyze the azimuthal dependence of site effects, in particular with consideration of 3D neighboring effects (e.g. the possible presence of neighboring fault, hill).

To conduct additional further field tests, shaking table tests or centrifuge tests to do comparisons with numerical results.

To continue investigating the site effect on the slope stability, in particular when considering the water and possible generation of additional pore water pressures induced by earthquakes.

Finally, besides site effect, the seismic wave motion generated in a site also depends on source mechanism, earthquake magnitude and wave transmission path. Therefore, it would be better to obtain the possible seismic effects by a statistical approach accounting for the related uncertainties.

References

Abbott, P.L., 2008. Natural disasters. McGraw-Hill New York.

Achenbach, J., 2012. Wave propagation in elastic solids. Elsevier, Amsterdam.

Aki, K., Larner, K.L., 1970. Surface motion of a layered medium having an irregular interface due to incident plane SH waves. *Journal of Geophysical Research* 75, 933-954.

Ambraseys, N., 1960. On the shear response of a two-dimensional truncated wedge subjected to an arbitrary disturbance. *Bulletin of the Seismological Society of America* 50, 45-56.

Ambraseys, N.N., Adams, R.D., 2001. Seismicity of Central America: A Descriptive Catalogue, 1898-1995. World Scientific.

Arias, A., 1970. Measure of earthquake intensity. Massachusetts Institute of Technology, Cambridge. University of Chile, Santiago de Chile.

Ashford, S.A., Sitar, N., 1997. Analysis of topographic amplification of inclined shear waves in a steep coastal bluff. *Bulletin of the Seismological Society of America* 87, 692-700.

Ashford, S.A., Sitar, N., Lysmer, J., Deng, N., 1997. Topographic effects on the seismic response of steep slopes. *Bulletin of the Seismological Society of America* 87, 701-709.

Assimaki, D., Gazetas, G., Kausel, E., 2005. Effects of local soil conditions on the topographic aggravation of seismic motion: parametric investigation and recorded field evidence from the 1999 Athens earthquake. *Bulletin of the Seismological Society of America* 95, 1059-1089.

Assimaki, D., Jeong, S., 2013. Ground‐motion observations at Hotel Montana during the M 7.0 2010 Haiti earthquake: Topography or soil amplification? *Bulletin of the Seismological Society of America* 103, 2577-2590.

Assimaki, D., Kausel, E., 2007. Modified topographic amplification factors for a single-faced slope due to kinematic soil-structure interaction. *Journal of Geotechnical and Geoenvironmental Engineering* 133, 1414-1431.

Asten, M.W., 2004. Comment on "Microtremor observations of deep sediment resonance in metropolitan Memphis, Tennessee" by Paul Bodin, Kevin Smith, Steve Horton and Howard Hwang. *Engineering Geology* 72, 343-349.

Atkinson, G.M., Cassidy, J.F., 2000. Integrated use of seismograph and strong-motion data to determine soil amplification: response of the Fraser River Delta to the Duvall and Georgia Strait earthquakes. *Bulletin of the Seismological Society of America* 90, 1028-1040.

Bard, P.-Y., 1982. Diffracted waves and displacement field over two-dimensional elevated topographies. *Geophysical Journal International* 71, 731-760.

Bard, P.-Y., 1995. Effects of surface geology on ground motion: recent results and remaining issues, 10th European conference on earthquake engineering, pp. 305-323.

Bard, P.-Y., Bouchon, M., 1980. The seismic response of sediment-filled valleys. Part 1. The case of incident SH waves. *Bulletin of the Seismological Society of America* 70, 1263-1286.

Barlow, N., 1933. Charles Darwin's Diary of the Voyage of HMS" Beagle". GB.

Bauer, R.A., Kiefer, J., Hester, N., 2001. Soil amplification maps for estimating earthquake ground motions in the Central US. *Engineering Geology* 62, 7-17.

Bertrand, E., Duval, A.-M., Régnier, J., Azzara, R., Bergamashi, F., Bordoni, P., Cara, F., Cultrera, G., Di Giulio, G., Milana, G., 2011. Site effects of the Roio basin, L'Aquila. *Bulletin of Earthquake Engineering* 9, 809-823.

Bo, J., Qi, W., Liu, H., Liu, B., Liu, D., Sun, Y., 2009. Abnormality of seismic intensity in Hanyuan during Wenchuan earthquake. *Journal of Earthquake Engineering and Engineering Vibration* 29, 53-63.

Bommer, J.J., Rodríguez, C.E., 2002. Earthquake-induced landslides in Central America. *Engineering Geology* 63, 189-220.

Bonamassa, O., Vidale, J.E., 1991. Directional site resonances observed from aftershocks of the 18 October 1989 Loma Prieta earthquake. *Bulletin of the Seismological Society of America* 81, 1945-1957.

Boore, D.M., 1972. A note on the effect of simple topography on seismic SH waves. *Bulletin of the Seismological Society of America* 62, 275-284.

Boore, D.M., 1973. The effect of simple topography on seismic waves: implications for the accelerations recorded at Pacoima Dam, San Fernando Valley, California. *Bulletin of the Seismological Society of America* 63, 1603-1609.

Boore, D.M., Harmsen, S.C., Harding, S.T., 1981. Wave scattering from a step change in surface topography. *Bulletin of the Seismological Society of America* 71, 117-125.

Borcherdt, R.D., 1970. Effects of local geology on ground motion near San Francisco Bay. *Bulletin of the Seismological Society of America* 60, 29-61.

Bouchon, M., 1973. Effect of topography on surface motion. *Bulletin of the Seismological Society of America* 63, 615-632.

Bouchon, M., Barker, J.S., 1996. Seismic response of a hill: the example of Tarzana, California. *Bulletin of the Seismological Society of America* 86, 66-72.

Bouchon, M., Schultz, C.A., Toksöz, M.N., 1996. Effect of three - dimensional topography on seismic motion. *Journal of Geophysical Research: Solid Earth* 101, 5835-5846.

Bouckovalas, G., Kouretzis, G., 2001. Stiff soil amplification effects in the 7 September 1999 Athens (Greece) earthquake. *Soil Dynamics and Earthquake Engineering* 21, 671-687.

Bouckovalas, G.D., Papadimitriou, A.G., 2005. Numerical evaluation of slope topography effects on seismic ground motion. *Soil Dynamics and Earthquake Engineering* 25, 547-558.

Bourdeau, C., 2005. Effets de site et mouvements de versant en zones sismiques: apport de la modélisation numérique. École Nationale Supérieure des Mines de Paris.

Buech, F., Davies, T., Pettinga, J., 2010. The Little Red Hill Seismic Experimental Study: Topographic Effects on Ground Motion at a Bedrock-Dominated Mountain Edifice. *Bulletin of the Seismological Society of America* 100, 2219-2229.

Caserta, A., Bellucci, F., Cultrera, G., Donati, S., Marra, F., Mele, G., Palombo, B., Rovelli, A., 2000. Study of site effects in the area of Nocera Umbra (Central Italy) during the 1997 Umbria-Marche seismic sequence. *Journal of Seismology* 4, 555-565.

Castello, B., Olivieri, M., Selvaggi, G., 2007. Local and duration magnitude determination for the Italian earthquake catalog, 1981–2002. *Bulletin of the Seismological Society of America* 97, 128-139.

Çelebi, M., 1987. Topographical and geological amplifications determined from strong-motion and aftershock records of the 3 March 1985 Chile earthquake. *Bulletin of the Seismological Society of America* 77, 1147-1167.

Chaljub, E., Moczo, P., Tsuno, S., Bard, P.-Y., Kristek, J., Käser, M., Stupazzini, M., Kristekova, M., 2010. Quantitative comparison of four numerical predictions of 3D ground motion in the Grenoble Valley, France. *Bulletin of the Seismological Society of America* 100, 1427-1455.

Chiarabba, C., Amato, A., Anselmi, M., Baccheschi, P., Bianchi, I., Cattaneo, M., Cecere, G., Chiaraluce, L., Ciaccio, M., De Gori, P., 2009. The 2009 L'Aquila (central Italy) MW6. 3 earthquake: Main shock and aftershocks. *Geophysical Research Letters* 36.

Cormier, V., Spudich, P., 1984. Amplification of ground motion and waveform complexity in fault zones: examples from the San Andreas and Calaveras faults. *Geophysical Journal of the Royal Astronomical Society* 79, 135-152.

Crosta, G., Imposimato, S., Roddeman, D., Chiesa, S., Moia, F., 2005. Small fast-moving flow-like landslides in volcanic deposits: the 2001 Las Colinas Landslide (El Salvador). *Engineering Geology* 79, 185-214.

Dai, F., Xu, C., Yao, X., Xu, L., Tu, X., Gong, Q., 2011. Spatial distribution of landslides triggered by the 2008 Ms 8.0 Wenchuan earthquake, China. *Journal of Asian Earth Sciences* 40, 883-895.

De Raedt, H., Michielsen, K., Hess, K., 2012. Analysis of multipath interference in three-slit experiments. *Physical Review A* 85, 012101.

Del Gaudio, V., Wasowski, J., 2007. Directivity of slope dynamic response to seismic shaking. *Geophysical Research Letters* 34.

Del Gaudio, V., Wasowski, J., 2011. Advances and problems in understanding the seismic response of potentially unstable slopes. *Engineering Geology* 122, 73-83.

Dewey, J.W., Suárez, G., 1991. Seismotectonics of middle America, Neotectonics of North America. Geological Society of America, pp. 309-321.

Donati, S., Marra, F., Rovelli, A., 2001. Damage and ground shaking in the town of Nocera Umbra during Umbria-Marche, central Italy, earthquakes: the special effect of a fault zone. *Bulletin of the Seismological Society of America* 91, 511-519.

Dravinski, M., Ding, G., Wen, K.-L., 1996. Analysis of spectral ratios for estimating ground motion in deep basins. *Bulletin of the Seismological Society of America* 86, 646-654.

Durand, S., Gaffet, S., Virieux, J., 1999. Seismic diffracted waves from topography using 3-D discrete wavenumber-boundary integral equation simulation. *Geophysics* 64, 572-578.

Faccioli, E., 1991. Seismic amplification in the presence of geological and topographic irregularities.

Fan, X., van Westen, C.J., Xu, Q., Gorum, T., Dai, F., 2012. Analysis of landslide dams induced by the 2008 Wenchuan earthquake. *Journal of Asian Earth Sciences* 57, 25-37.

Fleurisson, J.-A., Bourdeau, C., 2006. Numerical simulations of ground motion amplifications due to elevated topography and surface geology, Third International Symposium on the Effects of Surface Geology on Seismic Motion, pp. paper 151, 110 p.

Frankel, A., 1993. Three-dimensional simulations of ground motions in the San Bernardino Valley, California, for hypothetical earthquakes on the San Andreas fault. *Bulletin of the Seismological Society of America* 83, 1020-1041.

Frankel, A., Stephenson, W., 2000. Three-dimensional simulations of ground motions in the Seattle region for earthquakes in the Seattle fault zone. *Bulletin of the Seismological Society of America* 90, 1251-1267.

Frankel, A., Vidale, J., 1992. A three-dimensional simulation of seismic waves in the Santa Clara Valley, California, from a Loma Prieta aftershock. *Bulletin of the Seismological Society of America* 82, 2045-2074.

Fukushima, Y., Irikura, K., Uetake, T., Matsumoto, H., 2000. Characteristics of observed peak amplitude for strong ground motion from the 1995 Hyogoken Nanbu (Kobe) earthquake. *Bulletin of the Seismological Society of America* 90, 545-565.

Gazetas, G., Kallou, P., Psarropoulos, P., 2002. Topography and soil effects in the M s 5.9 Parnitha (Athens) earthquake: the case of Adames. *Natural Hazards* 27, 133-169.

Geli, L., Bard, P.-Y., Jullien, B., 1988. The effect of topography on earthquake ground motion: a review and new results. *Bulletin of the Seismological Society of America* 78, 42-63.

Gil-Zepeda, S., Montalvo-Arrieta, J., Vai, R., Sanchez-Sesma, F., 2003. A hybrid indirect boundary element—discrete wave number method applied to simulate the seismic response of stratified alluvial valleys. *Soil Dynamics and Earthquake Engineering* 23, 77-86.

Gilbert, F., Knopoff, L., 1960. Seismic scattering from topographic irregularities. *Journal of Geophysical Research* 65, 3437-3444.

Griffiths, D.W., Bollinger, G., 1979. The effect of Appalachian Mountain topography on seismic waves. *Bulletin of the Seismological Society of America* 69, 1081-1105.

Guo, X., Keller, G.R., Gao, R., Xu, X., Wang, H., Li, W., 2014. Irregular western margin of the Yangtze block as a cause of variation in tectonic activity along the Longmen Shan fault zone, eastern Tibet. *International Geology Review* 56, 473-480.

Hébert, H., Reymond, D., Krien, Y., Vergoz, J., Schindelé, F., Roger, J., Loevenbruck, A., 2009. The 15 August 2007 Peru earthquake and tsunami: Influence of the source characteristics on the tsunami heights, Tsunami Science Four Years after the 2004 Indian Ocean Tsunami. Springer, pp. 211-232.

Hanks, T.C., McGuire, R.K., 1981. The character of high-frequency strong ground motion. *Bulletin of the Seismological Society of America* 71, 2071-2095.

Harris, R.A., 1998. Forecasts of the 1989 Loma Prieta, California, earthquake. *Bulletin of the Seismological Society of America* 88, 898-916.

Hartzell, S.H., Carver, D.L., King, K.W., 1994. Initial investigation of site and topographic effects at Robinwood Ridge, California. *Bulletin of the Seismological Society of America* 84, 1336-1349.

Havenith, H.-B., Vanini, M., Jongmans, D., Faccioli, E., 2003. Initiation of earthquake-induced slope failure: influence of topographical and other site specific amplification effects. *Journal of Seismology* 7, 397-412.

Hayes, G.P., 2011. Rapid source characterization of the 2011 M w 9.0 off the Pacific coast of Tohoku earthquake. *Earth, planets and space* 63, 4.

Hough, S.E., Altidor, J.R., Anglade, D., Given, D., Janvier, M.G., Maharrey, J.Z., Meremonte, M., Mildor, B.S.-L., Prepetit, C., Yong, A., 2010a. Localized damage caused by topographic amplification during the 2010 M 7.0 Haiti earthquake. *Nature Geoscience* 3, 778.

Hough, S.E., Altidor, J.R., Anglade, D., Given, D., Janvier, M.G., Maharrey, J.Z., Meremonte, M., Mildor, B.S.-L., Prepetit, C., Yong, A., 2010b. Localized damage caused by topographic amplification during the 2010 M [thinsp] 7.0 Haiti earthquake. *Nature Geoscience* 3, 778-782.

Housner, G.W., Thiel, C.C., 1990. Competing against time: report of the Governor's Board of Inquiry on the 1989 Loma Prieta earthquake. *Earthquake Spectra* 6, 681-711.

Hudson, J., Boore, D., 1980. Comments on 'Scattered surface waves from a surface obstacle'by JA Hudson. *Geophysical Journal of the Royal Astronomical Society* 60, 123-127.

Itasca, 2016. FLAC Version 8.0: Fast Lagrangian Analysis of Continua-User's Guide. Itasca Consulting Group Inc., Minneapolis Minnesota.

Jafarzadeh, F., Shahrabi, M.M., Farahi Jahromi, H., 2015. On the role of topographic amplification in seismic slope instabilities. *Journal of Rock Mechanics and Geotechnical Engineering* 7, 163-170.

Jibson, R.W., Crone, A.J., 2001. Observations and recommendations regarding landslide hazards related to the January 13, 2001 M-7.6 El Salvador earthquake. US Department of the Interior, US Geological Survey.

Jibson, R.W., Crone, A.J., Harp, E.L., Baum, R.L., Major, J.J., Pullinger, C.R., Escobar, C.D., Martínez, M., Smith, M.E., 2004. Landslides triggered by the 13 January and 13 February 2001 earthquakes in El Salvador. *Geological Society of America Special Papers* 375, 69-88.

Kaiser, A., Holden, C., Massey, C., 2013. Determination of site amplification, polarization and topographic effects in the seismic response of the port hills following the 2011 christchurch earthquake, NZSEE Conference, Wellington, New Zealand, pp. 1-8.

Kempton, J.J., Stewart, J.P., 2006. Prediction equations for significant duration of earthquake ground motions considering site and near-source effects. *Earthquake Spectra* 22, 985-1013.

Khazai, B., Sitar, N., 2004. Evaluation of factors controlling earthquake-induced landslides caused by Chi-Chi earthquake and comparison with the Northridge and Loma Prieta events. *Engineering Geology* 71, 79-95.

Kobayashi, Y., 1981. Causes of fatalities in recent earthquakes in Japan. *Natural disaster science* 3, 15-22.

Konagai, K., JOHANSSON, J., MAYORCA, P., YAMAMOTO, T., MIYAJIMA, M., UZUOKA, R., PULIDO, N.E., DURAN, F.C., SASSA, K., FUKUOKA, H., 2002. Las Colinas landslide caused by the January 13, 2001 off the coast of El Salvador earthquake. *Journal of Japan Association for Earthquake Engineering* 2, 1-15.

Korup, O., Clague, J.J., 2009. Natural hazards, extreme events, and mountain topography. *Quaternary Science Reviews* 28, 977-990.

Kuhlemeyer, R.L., Lysmer, J., 1973. Finite element method accuracy for wave propagation problems. *Journal of Soil Mechanics & Foundations Div* 99.

LeBrun, B., Hatzfeld, D., Bard, P., Bouchon, M., 1999. Experimental study of the ground motion on a large scale topographic hill at Kitherion (Greece). *Journal of Seismology* 3, 1-15.

Lee, S.-J., Komatitsch, D., Huang, B.-S., Tromp, J., 2009. Effects of topography on seismic-wave propagation: An example from northern Taiwan. *Bulletin of the Seismological Society of America* 99, 314-325.

Lei, X., Ma, S., Chen, W., Pang, C., Zeng, J., Jiang, B., 2013. A detailed view of the injection - induced seismicity in a natural gas reservoir in Zigong, southwestern Sichuan Basin, China. *Journal of Geophysical Research: Solid Earth* 118, 4296-4311.

Lenti, L., Martino, S., 2012. The interaction of seismic waves with step-like slopes and its influence on landslide movements. *Engineering Geology* 126, 19-36.

Lenti, L., Martino, S., 2013. A Parametric Numerical Study of the Interaction between Seismic Waves and Landslides for the Evaluation of the Susceptibility to Seismically Induced Displacements. *Bulletin of the Seismological Society of America* 103, 33-56.

Lenti, L., Martino, S., Paciello, A., Scarascia Mugnozza, G., 2009. Evidence of two-dimensional amplification effects in an alluvial valley (Valnerina, Italy) from velocimetric records and numerical models. *Bulletin of the Seismological Society of America* 99, 1612-1635.

Lotti, C., Associati, 2001. Informe final. Investigacion geotecnica integral en la cordillera El Balasmo, al sur de Santa Tecla, entre Las Colinias, Las Delicias y Las Colinas, pp. 1-30.

Lu, L., Yamazaki, F., Katayama, T., 1992. Soil amplification based on seismometer array and microtremor observations in Chiba, Japan. *Earthquake Engineering & Structural Dynamics* 21, 95-108.

Luo, Y., Del Gaudio, V., Huang, R., Wang, Y., Wasowski, J., 2014. Evidence of hillslope directional amplification from accelerometer recordings at Qiaozhuang (Sichuan—China). *Engineering Geology* 183, 193-207.

Luzon, F., Ramırez, L., Sanchez-Sesma, F., Posadas, A., 2003. Propagation of SH elastic waves in deep sedimentary basins with an oblique velocity gradient. *Wave motion* 38, 11-23.

Lysmer, J., 1969. Finite dynamic model for infinite media, Proc. of ASCE, pp. 859-877.

Marano, K.D., Wald, D.J., Allen, T.I., 2010. Global earthquake casualties due to secondary effects: a quantitative analysis for improving rapid loss analyses. *Natural Hazards* 52, 319-328.

Matsuoka, M., Yamazaki, F., 2006. Use of SAR imagery for monitoring areas damaged due to the 2006 Mid Java, Indonesia earthquake, Proceedings of 4th international workshop on remote sensing for post-disaster response.

Maufroy, E., Cruz-Atienza, V.M., Gaffet, S., 2012. A robust method for assessing 3-D topographic site effects: A case study at the LSBB Underground Laboratory, France. *Earthquake Spectra* 28, 1097-1115.

Meunier, P., Hovius, N., Haines, J.A., 2008. Topographic site effects and the location of earthquake induced landslides. *Earth and Planetary Science Letters* 275, 221-232.

Nakamura, Y., 1989. A method for dynamic characteristics estimation of subsurface using microtremor on the ground surface. *Railway Technical Research Institute, Quarterly Reports* 30.

Nguyen, K.-V., Gatmiri, B., 2007. Evaluation of seismic ground motion induced by topographic irregularity. *Soil Dynamics and Earthquake Engineering* 27, 183-188.

Ohtsuki, A., Harumi, K., 1983. Effect of topography and subsurface inhomogeneities on seismic SV waves. *Earthquake Engineering & Structural Dynamics* 11, 441-462.

Paolucci, R., 2002. Amplification of earthquake ground motion by steep topographic irregularities. *Earthquake Engineering & Structural Dynamics* 31, 1831-1853.

Pedersen, H., Le Brun, B., Hatzfeld, D., Campillo, M., Bard, P.-Y., 1994. Ground-motion amplitude across ridges. *Bulletin of the Seismological Society of America* 84, 1786-1800.

Pellet, F., Hosseini, K.A., Jafari, M.K., Zerfa, F.Z., Mahdavifar, M.R., Bakhshayesh, M.K., 2005. Geotechnical performance of Qanats during the 2003 Bam, Iran, earthquake. *Earthquake Spectra* 21, 137-164.

Pischiutta, M., Salvini, F., Fletcher, J., Rovelli, A., Ben-Zion, Y., 2012. Horizontal polarization of ground motion in the Hayward fault zone at Fremont, California: dominant fault-high-angle polarization and fault-induced cracks. *Geophysical Journal International* 188, 1255-1272.

Pitarka, A., Irikura, K., Iwata, T., Sekiguchi, H., 1998. Three-dimensional simulation of the near-fault ground motion for the 1995 Hyogo-ken Nanbu (Kobe), Japan, earthquake. *Bulletin of the Seismological Society of America* 88, 428-440.

Plafker, G., Ericksen, G.E., Fernandez Concha, J., 1971. Geological aspects of the May 31, 1970, Peru earthquake. *Bulletin of the Seismological Society of America* 61, 543-578.

Ponti, D.J., Wells, R.E., 1991. Off-fault ground ruptures in the Santa Cruz Mountains, California: Ridge-top spreading versus tectonic extension during the 1989 Loma Prieta earthquake. *Bulletin of the Seismological Society of America* 81, 1480-1510.

Poppeliers, C., Pavlis, G.L., 2002. The seismic response of a steep slope: High-resolution observations with a dense, three-component seismic array. *Bulletin of the Seismological Society of America* 92, 3102-3115.

Reyners, M., 2011. Lessons from the destructive Mw 6.3 Christchurch, New Zealand, earthquake. *Seismological Research Letters* 82, 371-372.

Rodríguez-Castellanos, A., Sanchez-Sesma, F., Ortiz-Alemán, C., Orozco-del-Castillo, M., 2011. Least square approach to simulate wave propagation in irregular profiles using the indirect boundary element method. *Soil Dynamics and Earthquake Engineering* 31, 385-390.

Sánchez-Sesma, F.J., 1985. Diffraction of elastic SH waves by wedges. *Bulletin of the Seismological Society of America* 75, 1435-1446.

Sánchez-Sesma, F.J., Arellano-Guzmán, M., Pérez-Gavilán, J.J., Suarez, M., Marengo-Mogollón, H., Chaillat, S., Jaramillo, J.D., Gómez, J., Iturrarán-Viveros, U., Rodríguez-Castellanos, A., 2010. Seismic response of three-dimensional rockfill dams using the Indirect Boundary Element Method, IOP Conference Series: Materials Science and Engineering. IOP Publishing, p. 012167.

Sánchez-Sesma, F.J., Campillo, M., 1991. Diffraction of P, SV, and Rayleigh waves by topographic features: A boundary integral formulation. *Bulletin of the Seismological Society of America* 81, 2234-2253.

Sánchez-Sesma, F.J., Herrera, I., Avilés, J., 1982. A boundary method for elastic wave diffraction: application to scattering of SH waves by surface irregularities. *Bulletin of the Seismological Society of America* 72, 473-490.

Sánchez-Sesma, F.J., Vai, R., DRETTA, E., 2001. The variational indirect boundary element method: A strategy toward the solution of very large problems of site response. *Journal of Computational Acoustics* 9, 531-541.

Semblat, J.-F., Duval, A.-M., Dangla, P., 2002. Seismic site effects in a deep alluvial basin: numerical analysis by the boundary element method. *Computers and geotechnics* 29, 573-585.

Semblat, J.F., Pecker, A., 2009. Waves and vibrations in soils: earthquakes, traffic, shocks, construction works. *Waves and vibrations in soils: Earthquakes, Traffic, Shocks, Construction works*, 500 p.

Sepúlveda, S.A., Murphy, W., Jibson, R.W., Petley, D.N., 2005. Seismically induced rock slope failures resulting from topographic amplification of strong ground motions: The case of Pacoima Canyon, California. *Engineering Geology* 80, 336-348.

Smerzini, C., Aviles, J., Paolucci, R., Sánchez‐Sesma, F., 2009. Effect of underground cavities on surface earthquake ground motion under SH wave propagation. *Earthquake Engineering & Structural Dynamics* 38, 1441-1460.

Spudich, P., Hellweg, M., Lee, W., 1996. Directional topographic site response at Tarzana observed in aftershocks of the 1994 Northridge, California, earthquake: implications for mainshock motions. *Bulletin of the Seismological Society of America* 86, S193-S208.

Stolte, A.C., Cox, B.R., Lee, R.C., 2017. An experimental topographic amplification study at Los Alamos National Laboratory using ambient vibrations. *Bulletin of the Seismological Society of America* 107, 1386-1401.

Telford, J., Cosgrave, J., 2006. Joint evaluation of the international response to the Indian Ocean tsunami: Synthesis report. Tsunami Evaluation Coalition (TEC).

Trifunac, M., 1971. Surface motion of a semi-cylindrical alluvial valley for incident plane SH waves. *Bulletin of the Seismological Society of America* 61, 1755-1770.

Tripe, R., Kontoe, S., Wong, T., 2013. Slope topography effects on ground motion in the presence of deep soil layers. *Soil Dynamics and Earthquake Engineering* 50, 72-84.

Tsai, Y.-B., Huang, M.-W., 2000. Strong ground motion characteristics of the chichi, Taiwan, earthquake of September 21, 1999. Institute of Geophysics, National Central University.

Wald, D.J., Helmberger, D.V., Heaton, T.H., 1991. Rupture model of the 1989 Loma Prieta earthquake from the inversion of strong-motion and broadband teleseismic data. *Bulletin of the Seismological Society of America* 81, 1540-1572.

Wang, H., Xie, L., 2010. Effects of topography on ground motion in the Xishan park, Zigong city. *Chinese Journal of Geophysics* 53, 1631-1638.

White, R.A., Harlow, D.H., 1993. Destructive upper-crustal earthquakes of Central America since 1900. *Bulletin of the Seismological Society of America* 83, 1115-1142.

Wilson, D.C., Pavlis, G.L., 2000. Near-surface site effects in crystalline bedrock: A comprehensive analysis of spectral amplitudes determined from a dense, three-component seismic array. *Earth Interactions* 4, 1-31.

Wilson, R.C., Keefer, D.K., 1985. Predicting areal limits of earthquake-induced landsliding.

Wong, H., Jennings, P., 1975. Effects of canyon topography on strong ground motion. *Bulletin of the Seismological Society of America* 65, 1239-1257.

Wong, H., Trifunac, M., 1974. Scattering of plane SH waves by a semi‐elliptical canyon. *Earthquake Engineering & Structural Dynamics* 3, 157-169.

Wood, C.M., 2013. Field investigation of topographic effects using mine seismicity.

Xu, X., Zhang, P., Wen, X., Qin, Z., Chen, C., Zhu, A., 2005. Features of active tectonics and recurrence behaviors of strong earthquakes in the western Sichuan Province and its adjacent regions. *Dizhen Dizhi(Seismology and Geology)* 27, 446-461.

Yang, Q., 2008. The divisional evaluation of urban environmental geology in Zigong city. Chengdu University of Technology.

Yang, Y., Li, X., He, Q., 2011. Numerical simulation for site effect of ridge terrain and overlaying soil in Zigong Xishan Park. *Technology for Earthquake Disaster Prevention* 4, 011.

Yin, Y., 2008. Researches on the geo-hazards triggered by Wenchuan earthquake, Sichuan. *Journal of Engineering Geology* 4, 7-12.

Yin, Y., Wang, F., Sun, P., 2009. Landslide hazards triggered by the 2008 Wenchuan earthquake, Sichuan, China. *Landslides* 6, 139-152.

Zahradn ík, J., Urban, L., 1984. Effect of a simple mountain range on underground seismic motion. *Geophysical Journal International* 79, 167-183.

Publications of the author

[1] Zezhong Zhang, Jean-Alain Fleurisson, Frederic Pellet, 2018. Numerical evidence of site effects contributing to triggering the Las Colinas landslide during the 2001 M_w=7.7 El Salvador earthquake. Landslides. DOI:10.1007/s10346-018-1040-y.

[2] Zezhong Zhang, Jean-Alain Fleurisson, Frederic Pellet, 2018. A case study of site effects on seismic ground motions at Xishan Park ridge in Zigong, Sichuan, China. Engineering Geology. DOI: 10.1016/j.enggeo.2018.07.004.

[3] Zezhong Zhang, Jean-Alain Fleurisson, Frederic Pellet, 2018. The effects of slope topography on acceleration amplification and interaction between slope topography and seismic input motion, Soil Dynamics and Earthquake Engineering, 113 420-431. DOI: 10.1016/j.soildyn.2018.06.019.

RÉSUMÉ

Dans cette thèse, des simulations numériques ont d'abord été effectuées avec le logiciel en différences finies FLAC (Itasca) sur un modèle de pente élastique linéaire homogène pour caractériser l'amplification de l'accélération le long de la surface située le long et à l'arrière de la crête d'une pente, et évaluer ainsi l'effet de la topographie sur l'amplification de l'accélération. L'interaction entre la fréquence du signal sismique appliqué à la base du modèle et l'angle et la hauteur de la pente a été particulièrement étudiée. Il a été constaté que le facteur d'amplification de l'accélération varie de manière significative avec l'angle et la hauteur de la pente ainsi que la fréquence et la durée (nombre de cycle) du signal. De plus, l'amplification du mouvement du sol due à la topographie de la pente est influencée de manière significative par l'effet de couplage complexe entre les ondes incidentes et les ondes réfléchies sur la topographie, et qu'elle est fortement contrôlée par le rapport entre la longueur d'onde du signal incident et la hauteur de la pente.

Les simulations numériques sont basées sur une étude géotechnique et une modélisation géomécanique nécessitant de valider les résultats par des comparaisons entre les résultats de modélisations et les données provenant des observations sur le terrain. L'analyse des domaines de fréquence, telle que la densité spectrale et la réponse en fréquence, est un moyen performant pour comprendre les caractéristiques des processus et les divers phénomènes qui ne peuvent pas être expliqués dans le domaine temporel. À cette fin, une étude de la crête du parc Xishan à Zigong au Sichuan en Chine a été réalisée. Les amplifications du site associées au mouvement du sol produit par le séisme de Wenchuan en 2008 ont été évaluées à l'aide de la technique du rapport spectral standard (SSR) et de la méthode d'accélération quadratique moyenne (arms) dans le domaine temporel. Une analyse numérique à 2D au moyen du logiciel FLAC (Itasca) a été ensuite mise en œuvre et les résultats ont été comparés aux mesures de terrain. Les pics "simulés" des amplifications spectrales sont toujours inférieurs à ceux dérivés des enregistrements de terrain. L'effet d'atténuation important sur le mouvement d'entrée pour les hautes fréquences met en évidence le fait qu'un rapport d'amortissement du signal ne représente pas correctement la dissipation d'énergie dans les simulations numériques. Des amplifications significatives se sont produites à des fréquences élevées (> 10 Hz) et sont considérées comme résultant de conditions locales spécifiques telles que la fracturation des roches et les irrégularités géométriques locales. Ces amplifications ne sont pas nécessairement localisées au sommet de la colline.

Enfin, des études paramétriques ont été réalisées avec des modèles élastiques en termes de diverses géométries de pente 2D et de couches géologiques de subsurface pour caractériser les amplifications du mouvement du sol. L'analyse paramétrique a pour but de comprendre le rôle joué par ces couches de surface, l'angle de la pente et la hauteur de la pente sur l'amplification du mouvement du sol, et donc d'évaluer si l'amplification du site peut être responsable du déclenchement du glissement de terrain. Ensuite, l'analyse dynamique sur des modèles de pente pour différentes magnitudes a été effectuée la stabilité de la pente du site de Las Colinas au Salvador a été évaluée sur la base du déplacement induit. Les résultats numériques ont clairement montré que les effets de site peuvent avoir induit d'importantes amplifications du mouvement du sol qui ont contribué à déclencher des glissements de terrain.

MOTS CLÉS

Effets de site topographiques, Simulations numériques, Stabilité des pentes, Tremblements de terre, Glissements de terrain

ABSTRACT

In this research work, numerical simulations using the finite difference FLAC software (Itasca)were first conducted with a homogeneous linear elastic slope model in order to characterize the acceleration amplification along the slope surface and behind the slope crest, and then to evaluate the topographic effect on the acceleration amplification. The interaction between the frequency of the seismic input motion applied at the base of the model with the slope angle and height has been deeply investigated. It was found that significant changes in the acceleration amplification factor result from variations in the slope angle and height as well as the signal frequency and duration. In addition, it has been shown that the ground motion amplification due to slope topography result from complex coupling effects between the input waves and the reflected waves on the topographic features and is highly controlled by the ratio between the wavelength of the input signal and the slope height.

Numerical simulations are based on geotechnical investigations and geotechnical modeling, and it is necessary to validate the results through comparisons between modeling results and field observations. Frequency domain analysis such as spectral density and frequency response are an effective way to understand process characteristics and the various phenomena that cannot be explained in the time domain. For this purpose, a case study at Xishan Park ridge in Zigong in China has been studied. Site amplifications associated with the ground motion produced by the 2008 Wenchuan earthquake have been evaluated using the Standard Spectral Ratio (SSR) technique and root-mean-square acceleration (arms) method in time domain. 2D numerical analysis using the FLAC software (Itasca) has been then performed and results have been compared with monitoring data. The "simulated" peaks of the spectral amplifications are always lower than those derived from the field records. The strong attenuation of input motion at high frequencies highlights the shortcoming that a signal damping ratio does not adequately represent the energy dissipation in numerical simulations. Significant amplifications occurred at high frequencies (>10 Hz) and are considered to result from local specific conditions such as rock fracturing and ridge steps; thus they do not necessarily occur at the top of the hill.

Finally, parametric studies were performed with elastic models in terms of various 2D slope geometries and geological layers to characterize the ground motion amplifications. The purpose of the parametric analysis is to understand the role of the geological layer, slope angle and slope height on the ground motion amplification, and thus to estimate if site amplifications could be responsible for the triggering of landslide. Then, the dynamic analysis on the slope model for different seismic magnitudes was performed and the Las Colinas slope stability in Salvador was evaluated through the analysis of the induced displacement. The numerical results clearly showed that site effects can have induced significant ground motion amplifications that contributed to trigger landslides.

KEYWORDS

Site effect, Numerical simulation, Slope, Earthquake, Landslides